Mid-Infrared Applications of Quasicylindrical Waves at Dielectric Interfaces

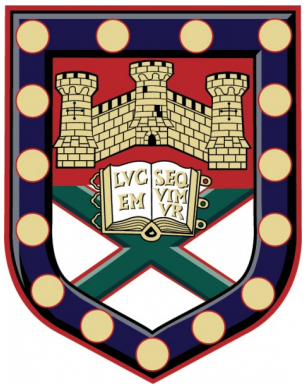

Oliver Higbee

Department of Engineering

University of Exeter

This dissertation is submitted for the degree of

Doctor of Philosophy in Engineering

CEMPS October 2019

Declaration

Oliver Higbee
October 2019

I certify that all material in this thesis which is not my own work has been identified and that no material has previously been submitted and approved for the award of a degree by this or any other University.

Signature: ……..

Contents

List of Figures

Chapter 1

Introduction

1.1 Motivation

Nanophotonics is facilitating the replacement of bulky optical components. Thin films can be patterned to produce almost flat optics and has allowed for optical structures to be integrated directly onto active devices, such as semiconductor lasers and diodes. These devices typically suffer from large intrinsic beam divergence, caused by their small aperture size. This lessens their effectiveness in some applications while ruling them out of being included in others. A smaller divergence would be invaluable for many applications such as: facilitating coupling of the laser output into optical fibers, waveguides, free space communications, ranging and remote sensing. Using semiconductor lasers as a case study, a brief summary of research efforts to reduce beam divergence is given below. These efforts metalise the dielectric facets of the active devices. The motivation of this work is to present a way of achieving integrated beam shaping structures while preserving the fully dielectric nature of the laser facet. This will make devices more simple to fabricate and aid commercial viability.

1.1.1 Semiconductor lasers

Semiconductor lasers are key in the development of emerging fields such as quantum information, medical imaging and 3D displays. They are also found at the heart of many common commercial technologies such as the interface for optical fiber communications and in compact disks (CDs). They are chosen above alternative light sources due to their simple construction, low power consumption and high efficiency. However they have two main drawbacks which prevent their use in other technologies. Firstly they suffer from large beam divergence, typically on the order of tens of degrees, this is caused by the small emission aperture [1]. Secondly, optical selection rules of the gain medium results in linearly polarized light along a

single plane [77]. Many technologies require a range of polarisations, such as circular polarisation and linear polarisation along different directions. Divergent output beams are conventionally collimated using external components such as lenses or curved mirrors. Polarisation is also conventionally controlled externally with waveplates and polarising beam splitters. External optics are bulky, can be expensive and not always readily available depending on the wavelength of the optical source. They also usually require meticulous optical alignment. The most effective way of minimizing the size and reduce the costs of optical components is to integrate them with the optical device they were designed for, to achieve the desired beam characteristics. There are many ways to approach this, for example tapered waveguides have been used to reduce beam divergence in ridge-waveguides semiconductor lasers [52]. Another solution would be increasing the effective emission area to reduce beam divergence, for example vertical-cavity surface-emitting lasers (VCSELs) have a larger emission area compared to edge-emitting semiconductor lasers, as such they typically have a smaller beam divergence, around 10º [56]. While this is an improvement over edge emitting lasers, 10º is still too large for many applications, which can require a beam divergence of less than 1º.

To achieve this further reduction in beam divergence, surface emitting structures have been integrated onto various laser types. Initially 1D grating outcouplers were integrated onto laser diodes to produce high directional beams [38]. These gratings were later applied to quantum cascade lasers (QCLs) for both mid-infrared QCLs and terahertz QCLs [16, 32]. These successfully reduced the beam divergence greatly along a single plane. Later work expanded this concept to two dimensions [51]. These were in the form of a 2D second order grating integrated onto a ring QCL. Fabrication of this design is complex, however it did show successfully collimation in two dimensions.

An alternative solution to surface emitting lasers are phase locked diode laser arrays, these not only reduce beam divergence but also enhance output power. These have been demonstrated for both 1D and 2D arrays with promising results [4, 68]. However they are more complicated to design and fabricate than 2D surface emitting lasers and it is difficult to see how these could be implemented onto viable commercial devices.

In recent years a favored method of integrated beam collimation has emerged, based on a aperture-groove structure. This forms the basis on the work demonstrated in this thesis and will be discussed below.

1.2 A brief history of beaming light from a subwavelength aperture

Light passing through an aperture has been studied for centuries. From classical diffraction theory, if the aperture is much smaller than the wavelength of the light passing through it, then the light emerging from the subwavelength aperture will diffract uniformly in all directions. The result is very poor transmission [8]. This phenomenon effectively puts a lower limit on the size of structures that can be used in photonics. However it has been shown by patterning the exit side of a metallic subwavelength aperture, with a periodic groove structure, this limitation can be overcome.

Lezec et al. [44] were the first to demonstrate that such a aperture-groove structure could be employed to drastically reduce the divergence of the light exiting a subwavelength aperture. They found that diffracted light was reduced from a classical half sphere diffraction pattern (without grooves) to a beam with an angular divergence of just 3º (with grooves), representing a ten fold boost in transmission. This result was found when the incident light was 580nm and the total patterned area was less than one cubic micrometer. To produce a beam divergence of 3º without the periodic groove structure, the aperture would be required to be ~5 microns. This is a significant lowering of the size limit of photonic structures. The effectiveness of the periodic groove structure is due to the excitation of surface waves called surface plasmons (SPs). SPs are collective electron excitations (charge density waves) on metallic surfaces. The underlining theory for SPs is discussed in detail in Chapter 2.

Following on from the concept demonstrated by Lezec et al, many experimental and theoretical studies on the plasmonic aperture-groove structure have been presented [5, 6, 25, 47, 78]. All showing that it is possible to create light sources with a high output power and small divergent angles on the nanoscale. And highlighting potential applications ranging from near-field scanning optical microscopy (NSOM) to free space communications. The next step in this research was to show the plasmonic structure integrated on active devices. The active devices chosen all suffered from a large intrinsic beam divergence due to transmission through a subwavelength aperture. Guo et al. were one of the first to attempt such an integration, patterning the front facet of a commercial edge emitting laser diode [29].

They first prepared the front facet by depositing a 300nm layer of SiO_2/SiN_x directly onto it, before depositing the 100nm metallic (gold) layer. The metallic film could not be directly deposited onto the front facet as the metal would connect the upper and bottom electrodes, causing a short circuit. Despite the prevention of a direct short circuit by deposition of a SiO_2/SiN_x layer, many diodes still fail because of cutting out resulting from the promixty of

the upper electrode to the gold film. To overcome this, an insulating channel to separate the upper electrode and gold film was etched. This increases the yield of the laser diode with a gold film. A 300nm by 500nm rectangular aperture and four rings (width 200nm, depth 40nm and period 380nm) were patterned into the gold layer with a focused ion beam (FIB). This resulted in a 140% increase in output power (0.7mW to 1.7mW) over a normal small aperture edge emitting laser diode.

This method of enhancement of light transmission through a subwavelength aperture was replicated for a near infrared (850nm) light source by Gao et al. [24]. A nano-aperture vertical-cavity surface-emitting laser array (NA-VCSL) was patterned with concentric periodic grooves, demonstrating a far-field output enhancement from 0.18mW to 0.3mW (67%), with a 9º beam divergence at 850nm. The facet was again prepared with the deposition of a half-wavelength thick layer of dielectric (400nm layer of SiO_2) to protect the P side of the VCSEL but no insulating channel was required. The lower enhancement when compared with the work done by Guo is largely caused by the diminishing effectiveness of SPs at longer wavelengths.

This concept was extended into the infrared the following year by the Capasso group at Harvard. They demonstrated plasmonic collimation in the mid-infrared by patterning a 9.9μm, TE polarised, quantum cascade laser (QCL) [80]. The facet of the semiconductor laser source was patterned with a metallic structure consisting of a sub-wavelength slit of 2μm width and an adjacent one dimensional grating. The grooves had to be adjacent to the aperture rather than surrounding due to the nature of the edge-emitting geometry. An edge emitting semiconductor was chosen over a conventional surface emitting laser because many applications require an edge rather than a surface emitting geometry. The measured beam divergence was reduced to 2.4º in the vertical direction and a high output power, comparable to unpatterned lasers was demonstrated. All devices with this slit-grating structure show a 10-20% larger divergence when measured, compared with simulations. This is thought to be caused by the sensitivity of the slit-grating structure to wavelength change. For example a change of 0.1μm in wavelength in the mid-infrared lead to a ~1º shift in position of the central lobe. Given that the light sources used are multi-mode and in the case of the 9.9μm QCL has a bandwidth of 0.05-0.1μm, such a change of divergence should be expected. Combining edge emitting in the mid-infrared with no significant reduction in output power was a major step forward in the concept to application path.

The group then extended this method by patterning a two dimensional plasmonic structure onto the facet of a 8.06μm QCL to achieve a 2D collimation for a linearly polarised edge-emitting semiconductor laser [79]. The 2D structure consisted of a subwavelength aperture on the laser active region and an array of half rings centered on the aperture. The struc-

ture returned a beam divergence of 2.7º in the perpendicular direction and 3.7º in the parallel direction, this compared with beam divergences of the unpatterned devices of 74º and 42º respectively. An output power of 53% compared to an unpatterned device was preserved.

In 2009 the group started to look at other integrated beam manipulating structures. Yu et al. demonstrated plasmonic control of a semiconductor laser's polarisation with a subwavelength-aperture grooves structure [82]. Again a mid-infrared edge-emitting QCL was used as the model device. QCLs are intrinsically transverse magnetically (TM) polarised, due to the optical selection rules of the gain medium [77]. By patterning the facet with a 1D slit-groove structure at an offset angle to the active region's waveguide, output light can be linearly polarised at a different angle to an unpatterned QCL. The objective of producing linearly polarised light along other directions to an unpatterned QCL was achieved. The next objective was to transform a linearly polarised laser into a circularly polarised device. This was attempted by patterning the facet with two orthogonal 1D aperture-grating structures adjacent to each other. The result was a superposition of linearly and right-circularly polarised light. This could be first step towards a circularly polarised laser, if a way to suppress the linearly polarized component can be found.

In summary the plasmonic approach to beaming has successfully demonstrated beam collimation of light exiting a subwavelength aperture, for visible and infrared light sources. The potential to obtain other desirable beam properties with this approach such as different polarisations has also been shown. However for integration on active devices, depositing the metallic surfaces to support SPs makes fabrication of such devices more difficult, more costly and can be detrimental to the device's functionality. An all-dielectric approach would simplify fabrication and be more cost effective. Also given that SPs perform less optimally at longer wavelengths where losses are high, the surface waves described in this thesis may provide a viable alternative to the plasmonic approach at infrared wavelengths.

1.3 Contributions of this work

The results presented in thesis are among the first to demonstrate collimation of light exiting a subwavelength aperture using a purely dielectric grating. Results have been published in a conference paper (Frontiers in Optics 2016) and presented at frontiers in optics (FiO) in Rochdale, USA [31]. Work is ongoing to publish the modelling results presented in Chapters 4 and 7. The original project for this thesis was to employ phase change materials to achieve tunable beaming of infrared light. The phase change material chosen was GeTe, unfortunately upon performing optical measurements on the device, it was clear the phase changing mechan-

ics were poorly understood within our research group and it was decided to switch to studying beaming of mid-IR light using quasicylindrical waves (QCWs) on dielectric interfaces.

1.4 Outline of Thesis

In this introduction motivation for this study has been identified. The applications and limitations of semiconductor lasers have been stated and work done to tackle these limitations have been summarised. The field of beam shaping has been introduced and key results in the area of integrated beam collimation have been presented. Applications from this field of study have been outlined and contributions of this work given.

Background theory behind the electromagnetic surface waves presented in this thesis is outlined in Chapter 2. The surface plasmon polariton (SPP) is introduced alongside a brief history of how the field of research developed. The SPP dispersion relation at a flat metallic-dielectric interface is derived and key properties of the surface mode discussed. SPP coupling geometries are presented and analysed. The latter half of the chapter focuses on the quasi-cylindrical wave (QCW), starting with its discovery and the hybrid wave theory. A closed form expression of the QCW is derived from a dipole line source radiating at a flat metallic-dielectric interface. The QCW is compared to the SPP with key properties contrasted. Finally isolated QCWs on fully dielectric interfaces are discussed.

The computation methods employed to model the photonic structures designed in this thesis are identified in Chapter 3. The transfer matrix method (TMM) and finite difference time domain method (FDTD) are described in detail. Explanations of how each method works are given by deriving key electromagnetic relationships. Important components that are used in the FDTD method are described, these are; boundary conditions, meshing, sources and far field projections. How each component can be used to improve efficiency and accuracy of the model are described. Lastly sources of error and the method, convergence, of how to identify and reduce errors has are discussed.

Chapter 4 describes the design of a fully dielectric mid-infrared band pass filter using the transfer matrix method (TMM). The design is then recreated in a 2D finite difference time domain method (FDTD) model. A subwavelength aperture is then created in the filter and near and far field results are illustrated. By applying a resonant nanograting to the exit side of the filter the effect of quasicylindrical waves (QCWs) on the near and far fields are presented. The nanograting design is then optimized and improvements to the full width half maximum (FWHM) of the far field are shown. Finally the model is expanded into three dimensions and the 2D results are successfully verified.

Chapter 5 presents the fabrication processes used to pattern the photonic structures onto a mid IR dielectric band pass filter. An overview on how a focused ion beam (FIB) works is given alongside how it was utilized in the fabrication process. A fabrication method for creation of a fully dielectric 1D QCW grating is outlined and fabrication results presented. The measurement system is introduced and initial measurements of the device are presented.

In Chapter 6, optical measurements are presented on the patterned fully dielectric mid-infrared band pass filter, which was designed and modelled in Chapter 4 and fabricated as described in Chapter 5. Analysis is outlined on the far field radiation pattern produced by the geometries designed in this thesis and flaws in the filter are highlighted. Solutions to these problems are then presented and implemented on a second mid-infrared band pass filter described at the end of the chapter.

Modelling of 2D and asymmetrical dielectric structures in FDTD are presented in Chapter 7. Analysis of the simulations including near and far field results are given. Fabrication of the 2D and asymmetrical gratings are shown on a second dielectric band pass filter. Measurement results and analysis are carried out on the second filter and key properties of QCWs are discussed.

Finally, in Chapter 8, a brief summary of the results presented in this thesis is given and conclusions from this work are drawn along with suggestions on future work to be carried out.

Chapter 2

Background Theory

2.1 Overview

This chapter will introduce the theory behind the electromagnetic surface waves discussed in this thesis. The surface plasmon polariton (SPP) will be introduced with a brief history of how the field developed. The SPP dispersion relation at a flat metallic-dielectric interface will be derived and key properties of the surface mode will be discussed. SPP coupling geometries will be presented and analysed. The latter half of this chapter will focus on the quasicylindrical wave (QCW), starting with its discovery and the hybrid wave theory. A closed form expression of the QCW will be derived from a dipole line source radiating at a flat metallic-dielectric interface. The QCW will be compared to the SPP with key properties contrasted. Finally isolated QCWs on fully dielectric interfaces will be discussed.

2.2 Surface Plasmon Polariton

For over a century there have been investigations into the interactions between metals and electromagnetic radiation. The first observation of a surface plasmon polariton (SPP) was made by Wood in 1902 [76]. When he shone polarized light onto a mirror with a diffraction grating on its surface, Wood observed a pattern of anomalous dark and light bands in the reflected light. Lord Rayleigh explained the observed dark bands as the wavelength of incident light at which a diffracted light ray will, or cease, to propagate, in his theory of diffraction gratings in 1907 [62]. This is referred to as the Rayleigh anomaly. The bright bands were not explained until 1941 by Fano [17–19], who concluded that this reflectivity anomaly was the result of interactions of light with a trapped surface wave, comprised in part by the metal's conduction electrons at the surface. By solving Maxwell's equations, Fano found that such a

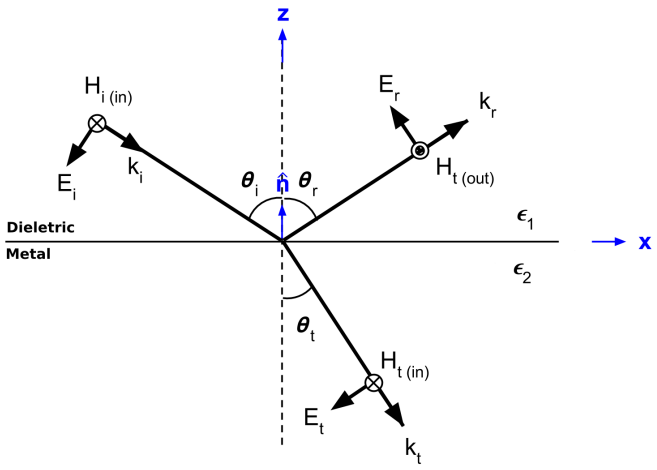

Figure 2.1: Incident TM polarized light on a metal-dielectric interface

wave could exist at an interface between a metal and a dielectric. It is worth noting that similar work had been done by Zenneck [83] and Sommerfeld [70] on the transmission of radio waves across large distances using trapped surface waves between seawater and air.

These waves have been extensively studied and are well understood. It is known that a surface plasmon (SP) is a quantised longitudinal oscillation in the free electron gas of a metal, confined at a metal dielectric interface [46, 61]. These oscillations can be coupled to incident electromagnetic radiation, with transverse magnetic polarization, the resulting surface wave is known as a surface plasmon polariton (SPP) and is a combination of the charge carrier oscillation and the coupled electromagnetic radiation.

2.2.1 Dispersion Relation

By solving Maxwell's equations for a transverse magnetic (TM) polarized electromagnetic wave at a single interface between two materials of different permittivities, the dispersion relation (relationship between energy and momentum) for an SPP can be obtained [61]. Figure 2.1 shows the most simple geometry capable of sustaining SPPs, the flat interface is between a metallic layer and a dielectric layer, both have complex dielectric functions that are positive and the materials are assumed to be non-magnetic and semi-infinite. We will look for propagating wave solutions confined to the interface. First consider the incident TM electromagnetic wave, with wavevector $\vec{k} = (k_x, 0, k_z)$ and frequency ω, shown in Figure 2.1. The electric and magnetic fields can be written as:

$$\vec{E} = [E_x, 0, E_z] \, exp\,(i\,(k_x x + k_z z - \omega t)) \tag{2.1}$$

$$\vec{H} = [0, H_y, 0]\, exp\,(i\,(k_x x + k_z z - \omega t)) \tag{2.2}$$

Applying Maxwell's equation in the absence of free charge (Ampere's Law),

$$\vec{\bigtriangledown} \times \vec{H} = \varepsilon \frac{\delta \vec{E}}{\delta t} \tag{2.3}$$

gives,

$$H_Y = \frac{\varepsilon \omega E_x}{k_z} = -\frac{\varepsilon \omega E_z}{k_x} \tag{2.4}$$

By combining this with the electric (2.1) and magnetic fields (2.2), expressions for the incident (2.5, 2.6), reflected (2.7, 2.8) and transmitted (2.9, 2.10) fields can be found:

$$\vec{E_1^+} = \vec{E_{x1}^+} \left[1, 0, -\frac{k_x}{k_z}\right] exp\,(i\,(k_x x + k_z z - \omega t)) \tag{2.5}$$

$$\vec{H_1^+} = \vec{E_{x1}^+} \left[0, +\frac{\omega \varepsilon_m}{k_{z1}}, 0\right] exp\,(i\,(k_x x + k_z z - \omega t)) \tag{2.6}$$

$$\vec{E_1^-} = \vec{E_{x1}^-} \left[1, 0, +\frac{k_x}{k_z}\right] exp\,(i\,(k_x x - k_z z - \omega t)) \tag{2.7}$$

$$\vec{H_1^-} = \vec{E_{x1}^-} \left[0, -\frac{\omega \varepsilon_m}{k_{z1}}, 0\right] exp\,(i\,(k_x x + k_z z - \omega t)) \tag{2.8}$$

$$\vec{E_2^+} = \vec{E_{x2}^+} \left[1, 0, -\frac{k_x}{k_z}\right] exp\,(i\,(k_x x + k_z z - \omega t)) \tag{2.9}$$

$$\vec{H_2^+} = \vec{E_{x2}^+} \left[0, +\frac{\omega \varepsilon_d}{k_{z2}}, 0\right] exp\,(i\,(k_x x + k_z z - \omega t)) \tag{2.10}$$

The next step is the apply boundary conditions to the fields. The tangential components of the electric and magnetic fields have to be continuous across the interface, i.e.

$$E_{x1} = E_{x2} \tag{2.11}$$

and

$$H_{y1} = H_{y2} \tag{2.12}$$

As the SPP is non-radiative the incident field (or reflected field) can be set to zero, applying

this to (2.4) gives,

$$\vec{H}_y = -E_{x1}^{-}\frac{\omega\varepsilon_m}{k_{z1}} = -E_{x2}^{+}\frac{\omega\varepsilon_d}{k_{z2}} \tag{2.13}$$

where ε_m and ε_d are the dielectric functions of the metal and dielectric layers respectively. This can then be applied to the expressions for the fields and simplified to,

$$\frac{\varepsilon_m}{k_{z1}} = -\frac{\varepsilon_d}{k_{z2}} \tag{2.14}$$

Equation (2.14) is known as the existence condition for SPPs and shows that SPPs can only exist at the interface between a positive permittivity material (dielectric) and a negative permittivity material (metal). The surface is considered to be translationally invariant this means that momentum is conserved in the plane of the surface i.e. $k_{x1} = k_{x2} = k_x$. By applying this to the condition that the electric and magnetic fields are continuous across the interface (2.11 and 2.12), it can be shown that $\varepsilon k_0^2 = k_x^2 + k_{zj}^2$, rearranging this gives:

$$k_{zj} = \sqrt{\varepsilon_j k_0^2 - k_x^2} \tag{2.15}$$

where j is the medium that the field is propagating through. By substituting this into (2.14), an expression for the SPP dispersion relation can be obtained,

$$k_x = \frac{\omega}{c}\sqrt{\frac{\varepsilon_m\varepsilon_d}{\varepsilon_m + \varepsilon_d}} = k_{spp} \tag{2.16}$$

The SPP dispersion relation relates the angular frequency of the field (ω), to the wavevector along the surface (k_x). The energy and momentum of the SPP is related to these quantities by the reduced Planck's constant ($\hbar$). An example dispersion relation is shown in Figure 2.2. In this figure the dispersion of a surface plasmon polariton on a flat interface between silver and air is plotted along with a line representing a free space electromagnetic wave, called the 'light-line'. The light line and the surface plasmon polariton dispersion line do not cross, showing that there is no solution at which the energy and momentum of a free space electromagnetic wave and surface plasmon polariton are equal. From this we can conclude that for a given frequency, light does not have sufficient momentum to match that of a surface plasmon polariton therefore free space electromagnetic waves incident on a flat metal-air interface cannot couple to a surface plasmon polariton. Methods of coupling to surface plasmon polaritons will be discussed in 2.2.2.

As well as the momentum mismatch at a given frequency the dispersion relation can also be used to show other properties of SPPs [5]. By substituting the complex forms of ε_m and $\varepsilon_d$into (2.16) the real and imaginary parts of the SPP dispersion relation can be found. The

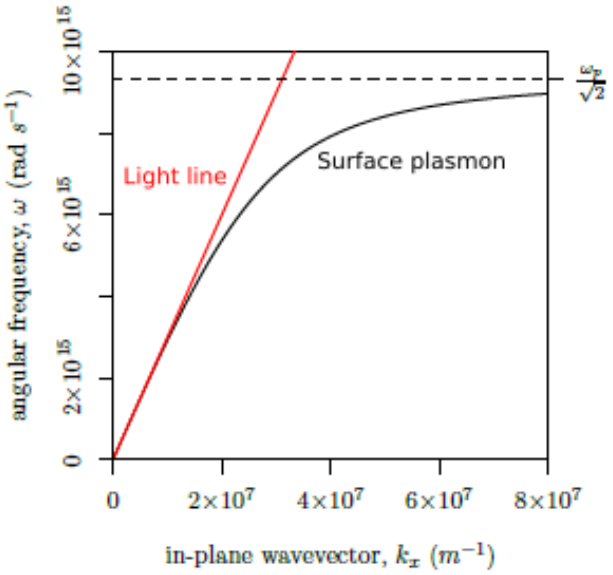

Figure 2.2: SPP Dispersion relation on a flat silver-air interface

imaginary part of the dispersion relation provides the exponential decay of the SPP as it travels along the interface, given by;

$$Im(k_x) = \frac{\omega}{c}\frac{Im(\varepsilon_d)}{2Re(\varepsilon_d)^2}\left(\frac{\varepsilon_m Re(\varepsilon_d)}{\varepsilon_m + Re(\varepsilon_d)}\right)^{\frac{3}{2}} \tag{2.17}$$

The propagation length of the SPP along the surface is defined as the length at which the field intensity drops to e^{-1} of it's maximum value. Therefore the propagation length, L_x, is given as,

$$L_x = \lambda_0 \frac{Re(\varepsilon_d)^2}{2\pi Im(\varepsilon_d)}\left(\frac{\varepsilon_m + Re(\varepsilon_d)}{\varepsilon_m Re(\varepsilon_d)}\right)^{\frac{3}{2}} \tag{2.18}$$

To give some context, for the flat interface between silver and air using a HeNe laser source (632nm), the propagation length is 42.6μm, which is sufficiently large enough to interact strongly on diffraction gratings with submicron periodicity.

Investigating the fields normal to the surface, due to (2.15), wave vectors k_{zj} must be purely imaginary. Substituting an imaginary k_{zj} into an expression for the electric field at the surface gives;

$$\vec{E}_j = \left[E_{xj}, 0, E_{zl}\right] e^{i(k_x x - \omega t)} e^{-k_{zj} z} \tag{2.19}$$

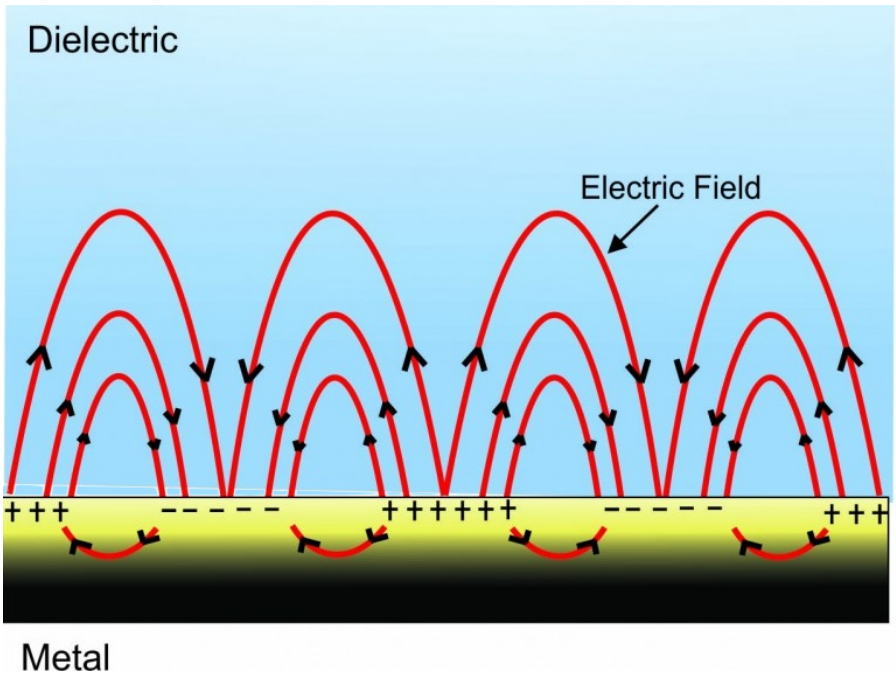

Figure 2.3: Electric field vectors of an SPP at the interface between a metal and a dielectric [3]

This describes an electric field that decays exponentially into the two surrounding media as it travels along the surface, a schematic of this electric field is shown in Figure 2.3. A measure of this decay is the penetration depth, L_z, which is the distance at which the field amplitude has decreased to e^{-1} of it's maximum value. The penetration depth is given by;

$$L_z = \lambda_0 \frac{1}{2\pi} \sqrt{\frac{Re(\varepsilon_d)}{Re(\varepsilon_j)^2}} \tag{2.20}$$

Again using the example of the flat interface between silver and air and a HeNe laser source, the penetration depth of the SPP into media is calculated to be 415nm into the air and 24nm into the metal.

2.2.2 Coupling to Surface Plasmons

As discussed above SPPs on a flat metal-dielectric interface cannot be directly excited by incident light due to the momentum mismatch at a given energy. To overcome this mismatch and allow coupling of light to SPPs different techniques have been employed, the three main methods will discussed here.

Photons incident upon a flat metal-dielectric interface at an angle θ will have a wave vector $k_x = ksin\theta$, which is always smaller than the SPP propagation constant, k_{SPP} , preventing cou-

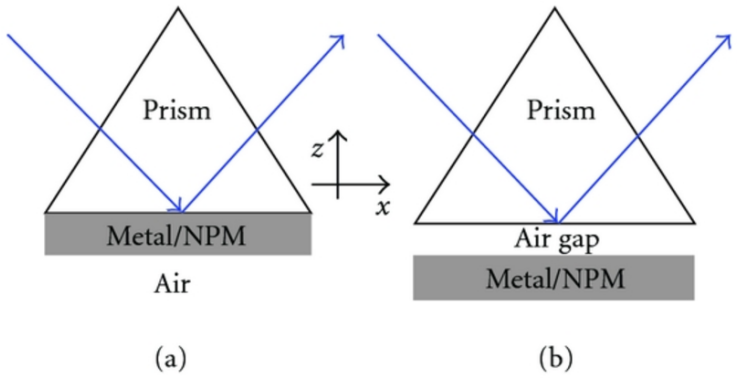

Figure 2.4: Kretschmann configuration (a) and Otto configuration (b) [15]

pling. By using a three layer system, consisting of a metal film placed between two dielectric layers with different refractive indices, the wave vector can be enhanced and coupling can be achieved. The higher index dielectric is in the form of a prism, with air usually fulfilling the role of a lower index dielectric. When the angle is sufficient, total internal reflection occurs at the interface between the prism and metallic layer, this results in a evanescently decaying field at the interface, decaying into the metallic layer. As there is no wavevector normal to the surface, all the momentum must be in the in-plane direction, $k_x = k\sqrt{\varepsilon}sin\theta$, where ε is the prism's dielectric constant. This is sufficient to excite SPPs at the interface, this coupling method is known as attenuated total internal reflection. Two geometries for this coupling are possible, by placing the metal film directly onto the prism's surface, known as the Kretschmann configuration [40, 41] (shown in figure 2.4) and with a small air gap between the prism and metal film, know as the Otto configuration [58], (shown in figure 2.4). The Otto configuration is often used in surface quality studies where direct contact with the metal surface is avoided [33].

Diffraction gratings with periodicity on the order of the wavelength of the incident light can also be used to couple incident light to SPPs. By patterning a metallic surface with a shallow grating of grooves, the incident light's in-plane momentum can be modified, a one-dimensional grating of grooves is shown in Figure 2.5. If the grating has a period of λ_g, its corresponding wavevector is k_g, when scattered, momentum can be added to the incident light such that $k_{scattered} = k\sin\theta + nk_g$, where n is the integer number of grating vectors. If the condition is met whereby $k_{scattered} = k_{SPP}$, light will couple to an SPP. This was the method employed when Wood first observed an SPP in 1902 and variations of this have been widely used. It is possible to replicate this method of coupling using a rough surface, the efficiency is greatly reduced, as is the propagation length of the SPP, however this method is used in surface enhanced Raman spectroscopy. A grating can also be used to reverse the process, SPPs propagating along a surface with a grating can couple to light and radiate. By altering

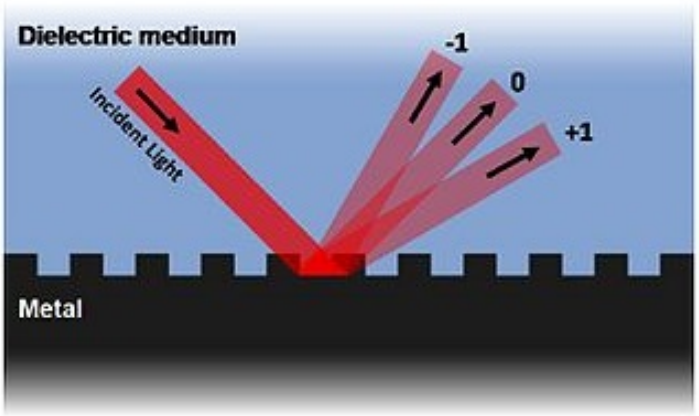

Figure 2.5: Schematic of light incident on a 1D diffraction grating

the geometry of the grating, the direction of radiation can be influenced, this method will be addressed later in this chapter.

The final method of coupling to SPPs is to scatter the incoming light at a single point, known as scattering centres. This point can be an aperture or edge. When light is incident on the aperture or edge, it will scatter in many different directions, some of the scattered light will have a wave vector such that $k_{scattered} = k_{SPP}$ allowing coupling to the surface mode. This method is inefficient when compared to grating or prism coupling, where nearly 100% coupling can be achieved. However this is a highly flexible method and it is possible to achieve broadband SPP coupling. A single subwavelength aperture, which is studied in Chapter 4, can exhibit high levels of transmission at optical frequencies. Transmission through the aperture is enabled by surface modes propagating along the sidewalls, as shown in Figure 2.6. Incident light scattering at the entrance to the aperture with wavevectors $k_{scattered} = k_{SPP}$ couple to the surface modes, which then propagate along the sidewalls of the aperture. Upon reaching the exit of the aperture, the surface modes will scatter, couple to light and reradiate [26].

2.2.3 Extraordinary Optical Transmission

In 1998, enhanced transmission of light through an array of cylindrical subwavelength holes in a silver thin film was observed by Ebbesen et al [13]. This study preceded the work done on the simpler isolated subwavelength slit structures and concluded that the Extraordinary Optical Transmission (EOT) at particular wavelengths was the result of the excitation of SPPs on the periodically patterned metal film. However the SPP model did not fully support the experimental results and as such the underlying mechanisms that cause EOT have been the subject of considerable debate.

In 2006, there were two papers published in Nature Physics that attempted to explain the

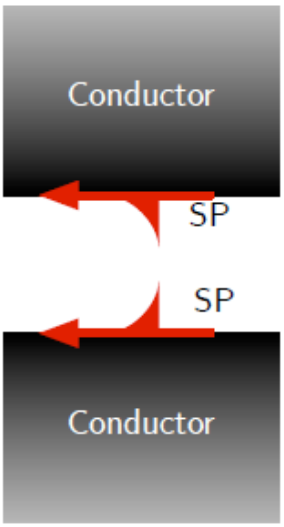

Figure 2.6: SPP propagation on the sidewalls of a subwavelength aperture

same EOT observations with two differing theories. They studied the transmission through a subwavelength aperture assisted by a single groove, this simple geometry was chosen to address the fundamentals of the near-field interaction, through far-field measurements and is shown in the insert of Figure 2.7. Gay et al [27] proposed a new type of surface wave, known as composite diffraction of surface evanescent waves (CDEW) to displace the existing SPP based interaction model. This was done because when d, the distance between the aperture and groove, is small, the existing SPP based model did not match the experimental data. The surface wave excited by the groove is called the CDEW and has the form $H_z(y) \propto (\kappa/y + \mu)\cos(k_{surf}U + \phi)$. In response to this paper Lalanne et al [42] showed that the SPP interaction was indeed responsible for the EOT but while it was the dominant surface wave, it was supplemented by an additional near-field wave. This residual near-field wave is known as the quasicylindrical wave (QCW) and provided good agreement between model and experiment for small values of d, as shown in Figure 2.7. It was also shown that the CDEW model fails at predicting the oscillation or phase of the scattered field for small groove widths.

2.3 Quasicylindrical waves (QCWs)

QCWs are a superposition of evanescent and radiative components. A closed form expression for the QCW fields can be derived and from this important properties of QCWs such as decay rates and field characteristics can be presented. The following is adapted from P. Lalanne's work [43]. We start by considering a flat metallic-dielectric interface along the x axis (y=0), as

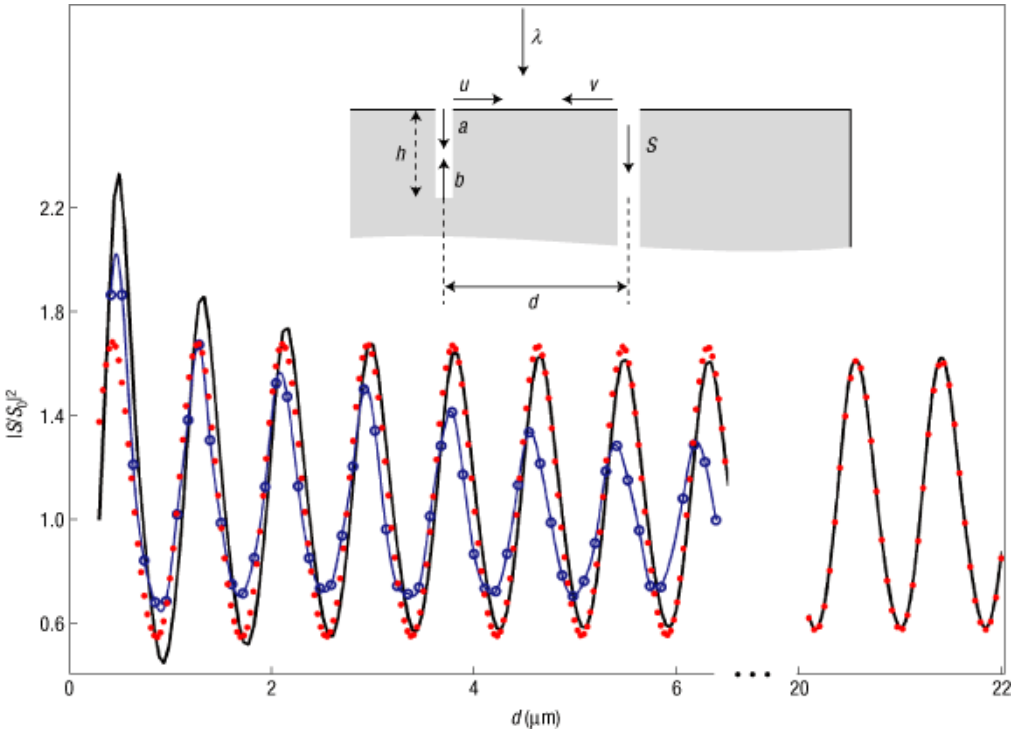

Figure 2.7: The transmission through the subwavelength metallic slit accompanied by a groove. Experimental data (blue circles), CDEW model (solid blue line), fully vectorial method model (solid black line) and surface plasmon mode model (red dots). The Insert is the geometry of the structure. [42]

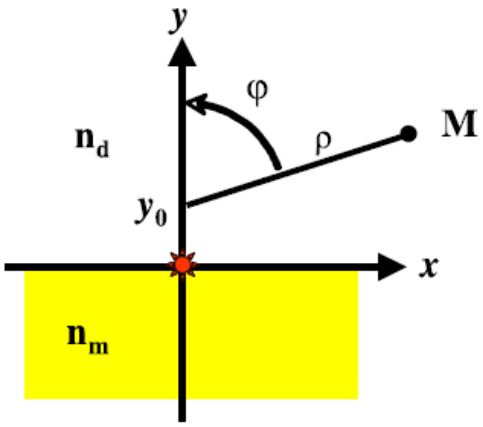

Figure 2.8: Schematic of a line source situated at x=y=0 on a metal-dielectric interface [43]

shown in Figure 2.8. The materials are considered to be nonmagnetic and semi infinite, with permittivities ε_m (metal) and ε_d (dielectric). A transverse magnetic (TM) polarized dipole line source is situated at x=y=0. The electromagnetic field of the infinitely small dipole can be described by the following equations;

$$\nabla \times \vec{E} = ik\vec{H} + H_z^S \vec{z}\,\delta(x,y) \tag{2.21}$$

$$\nabla \times \vec{H} = ik\varepsilon(\vec{r})\vec{E} + (E_x^S \vec{x} + E_y^S \vec{y})\delta(x,y) \tag{2.22}$$

Where $\delta(x,y)$ is the 2D Dirac distribution and S represents the source currents. Note $\varepsilon(\vec{r}) = \varepsilon_m$ below the x axis and $\varepsilon(\vec{r}) = \varepsilon_d$ above the x axis. (2.21) and (2.22) can be rewritten in the form;

$$\frac{\delta H_z}{\delta y} = ik\varepsilon E_x + E_x^S \delta(x,y) \tag{2.23}$$

$$-\frac{\delta H_z}{\delta x} = -ik\varepsilon E_y + E_y^S \delta(x,y) \tag{2.24}$$

$$\frac{\delta E_y}{\delta x} - \frac{\delta E_x}{\delta y} = ikH_z + H_z^S \delta(x,y) \tag{2.25}$$

This allows us to take advantage of the translational invariance in the x direction and use the inverse Fourier transform, $H_z = \int \hat{H}_z(u,y)\,exp\,(ikux)\,du$. With the 2D Dirac distribution

$\delta(x,y) = \frac{k}{2\pi}\int \delta(y)\, exp(ikux)\, du$. The electromagnetic field can then be written as;

$$\hat{E}_y = \frac{u}{\varepsilon}\hat{H}_z + \frac{i}{2\pi\varepsilon^S}E_y^S\delta(y) \tag{2.26}$$

$$\frac{\delta\hat{H}_z}{\delta y} = -ik\varepsilon\hat{E}_x + \frac{k}{2\pi}E_x^S\delta(y) \tag{2.27}$$

$$\frac{\delta\hat{E}_x}{\delta y} = ik\left(\varepsilon - u^2\right)\hat{H}_z - \frac{k}{2\pi}(H_z^S - \frac{u}{\varepsilon_S}E_y^S)\delta(y) \tag{2.28}$$

We can then perform the inverse Fourier transform to obtain a contour integral, known as a Sommerfeld integral;

$$[H_z, E_x, E_y] = \int_{-\infty}^{\infty} f(y,u)\, exp(\rho h)\, du \tag{2.29}$$

Where the function when $y > 0$ (in the dielectric) is;

$$f(y,u) = \frac{ik}{2\pi}\frac{exp(+ik\chi_d y_0)}{\frac{\chi_d}{\varepsilon_d} + \frac{\chi_m}{\varepsilon_m}}\left(H_z^S + \frac{\chi_m}{\varepsilon_m}E_x^S - \frac{u}{\varepsilon_S}E_y^S\right)\left[1, \frac{-\chi_d}{\varepsilon_d}, \frac{u}{\varepsilon_d}\right] \tag{2.30}$$

With;

$$h = ik\left(u\sin(\varphi) + \chi_d\cos(\varphi)\right) \tag{2.31}$$

And for $y < 0$ (in the metal) is;

$$f(y,u) = \frac{ik}{2\pi}\frac{exp(+ik\chi_d y_0)}{\frac{\chi_d}{\varepsilon_d} + \frac{\chi_m}{\varepsilon_m}}\left(H_z^S - \frac{\chi_d}{\varepsilon_d}E_x^S - \frac{u}{\varepsilon_S}E_y^S\right)\left[1, \frac{\chi_m}{\varepsilon_m}, \frac{u}{\varepsilon_m}\right] \tag{2.32}$$

With;

$$h = ik\left(u\sin(\varphi) - \chi_m\cos(\varphi)\right) \tag{2.33}$$

Where $\varepsilon_S = \varepsilon_m$ if the source is in the metal and $\varepsilon_S = \varepsilon_d$ if the source is in the dielectric. We define $\chi_d = \sqrt{\varepsilon_d - u^2}$ and $\chi_m = \sqrt{\varepsilon_m - u^2}$. The complete calculation of (2.29) is difficult as at large values of ρ the function becomes rapidly oscillating. To reduce the impact of these oscillations, the contour of integration can be deformed to take the steepest descent path. The steepest path occurs when the imaginary part of h (2.31 and 2.33) is constant, i.e. $\frac{dh}{du} = 0$. The integration path along the complex space of u is shown in Figure 2.9, branch cuts, shown with green and red vertical lines, are chosen to give the root functions χ_m and χ_d single values and the black star is a pole and represents the SPP contribution to the radiated field. Using

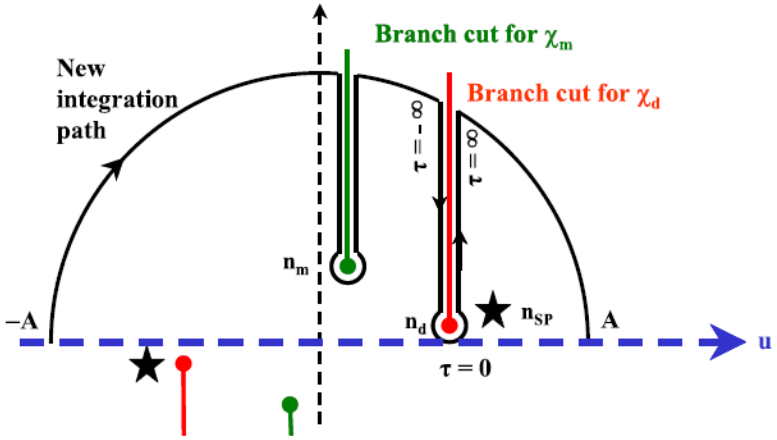

Figure 2.9: The contour in the complex plane for calculating the integral of equation (2.34). The black star indicates the pole, the green and red lines indicate branches of the integrand. [43]

Cauchy's integral formula we can obtain expressions for the SPP (pole) and QCW (branch cuts) contributions;

$$[H_z, E_x, E_y] = \Phi^{+}_{SPP} + \Phi^{+}_{QCW} \tag{2.34}$$

The contribution of SPPs are well understood and have already been covered in this chapter. The contribution of the QCW will be studied further, the approximate expression developed is accurate for $x \succ \lambda$ and near the metallic surface ($y \prec \lambda$). By approximating the field radiated by the line source ($\Psi(x,y) = [H_z, E_x, E_y]$) into a sum of SPP and QCW waves, which are launched in opposite directions, the field can be written as;

$$\Psi(x,y) = \left[\alpha^{+}\Psi^{+}_{SPP}(x,y) + \alpha^{-}\Psi^{-}_{QCW}(x,y)\right] + \left[\beta^{+}\Psi^{+}_{QCW}(x,y) + \beta^{-}\Psi^{-}_{SPP}(x,y)\right] \tag{2.35}$$

Where $\Psi^{\pm}_{SPP}(x,y) = \left[H^{\pm}_{z,SPP}, E^{\pm}_{x,SPP}, E^{\pm}_{y,SPP}\right]$ are the normalized SPP modes and $\alpha^{\pm}$ are the SPP excitation coefficients. Similarly $\Psi^{\pm}_{QCW}(x,y) = \left[H^{\pm}_{zQCW}, E^{\pm}_{x,QCW}, E^{\pm}_{y,QCW}\right]$ are the normalized QCWs with $\beta^{\pm}$ representing the QCW excitation coefficients. Focusing on the QCW contribution, the normalized QCW wave can be written as;

$$\Psi^{\pm}_{QCW}(x,y) \simeq \frac{W(2\pi\gamma|x|/\lambda)}{W(2\pi\gamma)} (\lambda/|x|)^{\frac{3}{2}} \Psi^{\pm}_{0}(x,y) \tag{2.36}$$

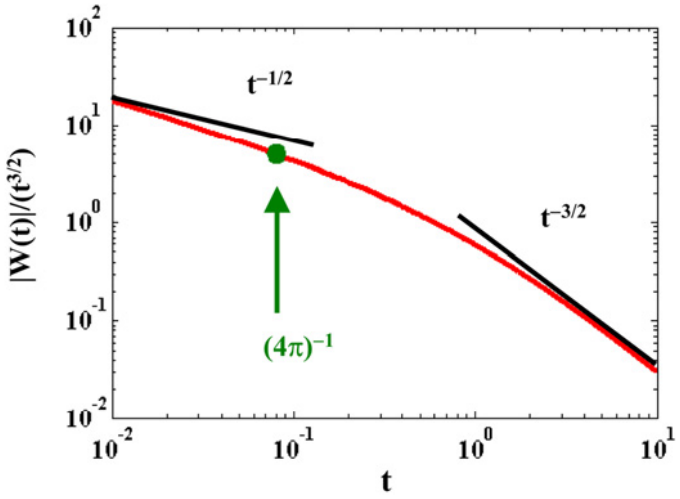

Figure 2.10: Plot of $\frac{|W(t)|}{t\sqrt{t}}$ as a function of t real. Shows two damping regimes, initial damping is $t^{-\frac{1}{2}}$ before transitioning to $t^{-\frac{3}{2}}$, where t is a complex variable. [43]

With;

$$\gamma = n_{SPP} - n_d = \frac{-n_d^3}{\left(\varepsilon_d + \varepsilon_m + \frac{n_m^3}{\chi_{SPP_m}}\right)} \tag{2.37}$$

W(t) is the complementary error function and describes the envelope of the QCW, importantly it governs the decaying rate, Figure 2.10 shows this decay rate, $\frac{|W(t)|}{t\sqrt{t}}$ is plotted as a function of t real, where t is complex variable. W(t) resembles the amplitude of the magnetic field and t, the distance from the line source.The figure shows two distinct damping regimes, the initial damping rate is $t^{-\frac{1}{2}}$, before transitioning to an asymptotic damping rate of $t^{-\frac{3}{2}}$, interestingly this second decaying regime is similar to Norton waves found in long distance radio transmissions studies [10]. The transition occurs at $4\pi t = 1$. The vectors $\Psi_0^{\pm}(x,y)$ provide the vector field pattern of the QCWs, for $y \succ 0$ the vector is;

$$\Psi_0^{\pm}(x,y) = exp(\pm ikn_d x)\left[1 - iky\left(\varepsilon_d\frac{\chi_m^0}{\varepsilon_m}\right), \frac{\chi_m^0}{\varepsilon_m}, \pm\frac{\left(1 - iky\left(\varepsilon_d\frac{\chi_m^0}{\varepsilon_m}\right)\right)}{n_d}\right] \tag{2.38}$$

And for $y \prec 0$;

$$\Psi_0^{\pm}(x,y) = exp(\pm ikn_d x)\, exp\left(-ik\chi_m^0 y\right)\left[1, \frac{\chi_m^0}{\varepsilon_m}, \frac{\pm in_d}{\varepsilon_m}\right] \tag{2.39}$$

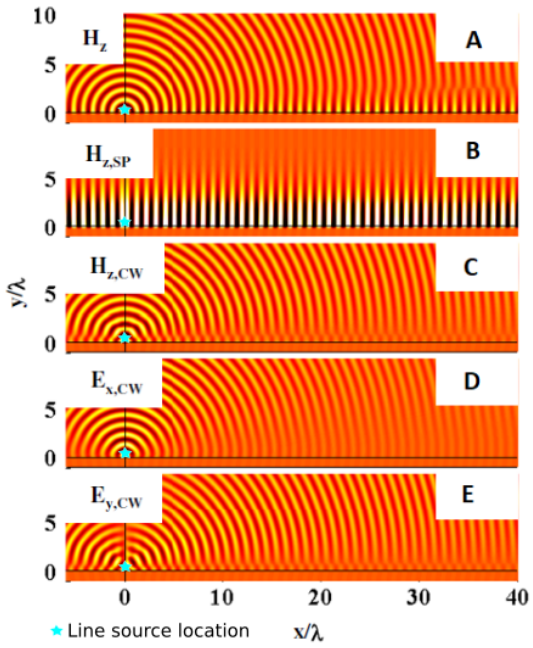

Figure 2.11: Electromagnetic fields generated by a TM polarized line source, polarized along the x-direction and located just above the metal surface at x=y=0. Total magnetic field (A), SPP contribution to magnetic field (B), QCW contribution to magnetic field (C) and the QCW electric field contribution polarized in x direction (D) and y direction (E). [43]

From this we can interpret that the QCW is a product of the asymptotic and small angle field by an envelope function. The final expression is the QCW excitation coefficient, giving the QCW generation at a distance of one wavelength from the indentation;

$$\beta^{\pm} = k\frac{\varepsilon_m^2\sqrt{in_d}}{\varepsilon_d\left(\varepsilon_e-\varepsilon_m\right)}\frac{W\left(2\pi\gamma\right)}{4\pi^2}\left[H^S+\frac{\chi_m^0}{\varepsilon_m}E_x^S \mp \frac{n_d}{\varepsilon^S}E_y^S\right] \tag{2.40}$$

By numerically solving (2.34), the exact solution can be obtained, this solution is shown in Figure 2.11. It vividly displays the cylindrical nature of the QCW, contrasted against the SPP mode and shows the significant contribution QCWs have to the shape of the total field, especially at distances of a few wavelengths. With the analysis complete we can conclude that QCWs are a superposition of evanescent and radiative components and that its field persists over a distance of a few wavelengths on the surface, at significant intensities. This is crucial because it means QCWs can be employed to play significant roles in compact optical devices. However the QCW attenuation rate is much faster than the characteristic damping of the SPP mode, meaning that SPPs dominate at metal-dielectric interfaces at distances of more than the incident wavelength. It is also understandable how EOT resulted in the discovery of QCWs as in EOT both decay regimes are present, due to the periodicity of the hole arrays.

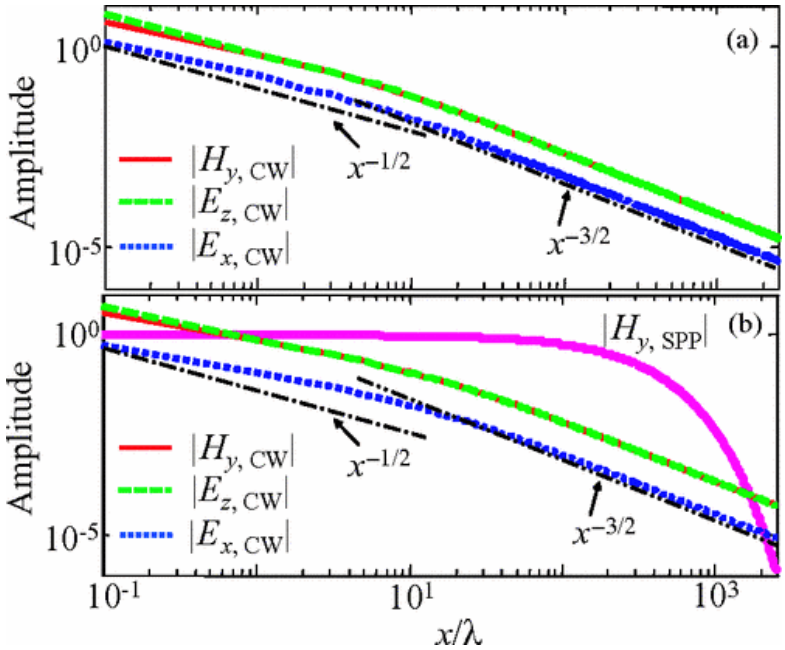

Figure 2.12: Decay characteristics of the field components of the waves launched at; a silicon-air interface (a) and gold-air interface (b). [23]

2.3.1 QCWs in Dielectric

In 2011, Choon How Gan et al [23] experimentally demonstrated that QCWs can be supported on dielectric interfaces. A silicon-air interface, with a subwavelength indentation, was illuminated by a laser diode at a TM polarized wavelength of 975nm and the near-field was probed with a fluorescent glass nano particle. The resultant surface wave resembled the QCW, with its characteristic electromagnetic field profile and two distinct decay regimes, initially decaying at $x^{-\frac{1}{2}}$ before transitioning to a decay rate of $x^{-\frac{3}{2}}$ at larger distances, as shown in Figure 2.12. This confirmed Lalanne's theory that QCWs can exist in the absence of SPPs, on dielectric interfaces or on perfectly electrically conducting (PEC) interfaces. This leads onto the question addressed in this thesis, can QCWs be employed on a fully dielectric interface to achieve beaming of infrared light in the absence of SPPs?

2.4 Summary

In this Chapter, the surface plasmon polariton (SPP) was introduced with a brief history of how this field of research has developed. The SPP dispersion relation at a flat metallic-dielectric interface was derived and key properties of the surface mode was discussed. The geometries capable of supporting SPPs were presented and explained. The quasicylindrical wave (QCW)

was introduced starting with how it was discovered and the hybrid wave model. A closed form expression of the QCW was derived from a dipole line source radiating at a flat metallic-dielectric interface. Key properties of the QCW was described and contrasted against the SPP. Finally isolated QCWs on fully dielectric interfaces were discussed.

Chapter 3

Photonic modelling methods

3.1 Overview

To optimize the design of photonic structures covered in this thesis, computational modelling is employed. Traditionally there are two main methods of optimization; iterative fabrication and theoretical modelling. Aided by recent advances in computing, computation modelling has become the main optimization method chosen, being both faster and more cost effect than the experimental equivalent. However regardless of which modelling method is chosen, models are approximations and should be verified with experiment. Every modelled structure described in this thesis is fabricated and experimentally measured. The modelling considered in this thesis is based on classical electrodynamics [48], with the smallest structures studied being tens of nanometers, this branch of theoretical physics is sufficiently accurate to describe interactions at these length scales where quantum mechanical effects, as described by quantum electrodynamics, are negligible. In this chapter the two main modelling methods used in this thesis are described in detail, these are the Transfer Matrix Method (TMM) and the Finite Difference Time Domain method (FDTD).

3.2 Transfer matrix method

The transfer-matrix method (TMM) is used in this thesis to optimize the reflection of dielectric stacks at specific wavelengths, more generally the TMM is used to analyse the propagation of electromagnetic waves through a multilayered one dimensional medium [53, 54]. Consider an arbitrary multilayered structure, consisting of layers of isotropic material, as shown in Figure 3.1. Light is partially reflected and partially transmitted at each interface, depending on the thickness of each layer and the wavelength of incident light, these reflections can construc-

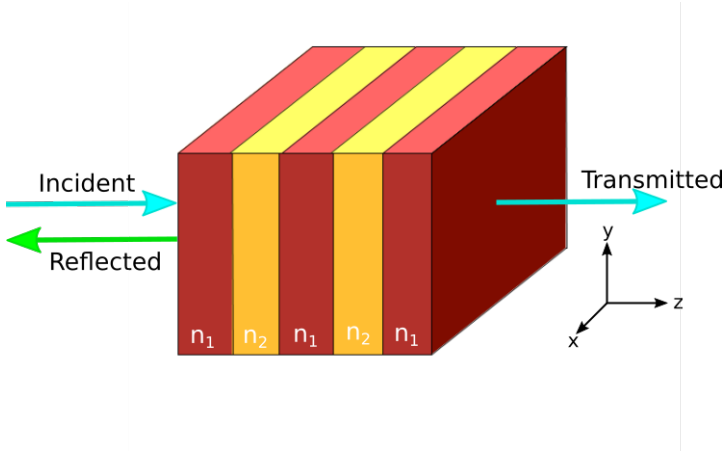

Figure 3.1: A 1D photonic crystal consisting of alternate layers of dielectric

tively or destructively interfere. The overall reflection of the structure can be seen as the sum of an infinite number of reflections. The continuity condition for the electric field across an interface from one layer to the next means that if the field is known at the start of a layer, then the field at the end of that layer can be derived. Using the continuity condition, the multilayered structure can be represented by a system matrix made up of individual layer matrices and this system matrix is called the transfer matrix.

Considering the multilayered structure, with layers of isotropic material stacked in the z-direction and light incident normal to the layers, as shown in Figure 3.1. The electromagnetic field can be broken down into the two polarizations; transverse electric polarization (TE) and transverse magnetic polarization (TM) . For TE polarization the electric field vector is $\vec{E} = (0, E_y, 0)$ and the magnetic field vector is $\vec{H} = (H_x, 0, H_z)$. The y component of the wavevector can be set to zero without loss of generality and the field can be taken to have harmonic time dependence $exp(-i\omega t)$. The field parallel to the structure is $exp(-ik_x x)$, where k_x is the same for all layers. Maxwell's equations can then be reduced to the Helmholtz equation for the spatial dependence of the electric field E_y in each layer and can be written as;

$$\frac{\partial^2 E_y}{\delta z^2} + k_z^2 E_y = 0 \tag{3.1}$$

where $k_z^2 = \varepsilon(\frac{w}{c})^2 - k_x^2$, with ε being the dielectric permittivity of the layer. A general solution of equation (3.1) is;

$$E_y = Aexp(ik_z z) + Bexp(-ik_z z) \tag{3.2}$$

where A and B are the amplitudes of the forward and backwards propagating waves respectively. The original TMM considered all waves to be forward propagating, this treatment leads

decaying fields associated with backward propagating waves (waves reflected at the interfaces between layers) to become exponentially growing fields, leading to numerical instability [75]. In homogeneous medium, the amplitudes at the start of a layer in the plane $z = z_0$ can be defined as (A_0, B_0) and at the end of that layer in the plane $z = z_1$ can be defined as (A_1, B_1). The relationship between the amplitudes at the two positions is $A_1 = A_0 exp[ik_z(z_1 - z_0)]$ and $B_1 = B_0 exp[-ik_z(z_1 - z_0)]$ and can be written in matrix form;

$$\begin{pmatrix} A_1 \\ B_1 \end{pmatrix} = \hat{P} \begin{pmatrix} A_0 \\ B_0 \end{pmatrix}; \ \hat{P} = \begin{pmatrix} e^{ik_z d} & 0 \\ 0 & e^{-ik_z d} \end{pmatrix} \tag{3.3}$$

where $d = z_1 - z_0$ and $\hat{P}$ is the transfer (propagation) matrix, expressed in terms of forward and backward propagating waves. It is also possible to express this in terms of tangential field components E_y and H_x. Following on from equation (3.1) the tangential components E_y and H_x can be written as;

$$E_y = Aexp(ik_z z) + Bexp(-ik_z z) \tag{3.4}$$

$$H_x = \frac{k_z}{k_0}[-Aexp(ik_z z) + Bexp(-ik_z z)] \tag{3.5}$$

where $k_0 = \omega/c$. Expressing in matrix form this becomes;

$$\begin{pmatrix} E_y \\ H_x \end{pmatrix} = \hat{W} \begin{pmatrix} A \\ B \end{pmatrix}; \ \hat{W} = \begin{pmatrix} 1 & 1 \\ -\frac{k_z}{k_0} & \frac{k_z}{k_0} \end{pmatrix} \tag{3.6}$$

The transfer matrix $\hat{T}$ expressed in terms of tangential field components is given by $\hat{T} = \hat{W}\hat{P}\hat{W^{-1}}$. The relationship between the tangential field components at different points, $z = z_0$ and $z = z_1$ in homogeneous medium is;

$$\begin{pmatrix} E_{y1} \\ H_{x1} \end{pmatrix} = \hat{T} \begin{pmatrix} E_{y0} \\ H_{x0} \end{pmatrix} \tag{3.7}$$

where the transfer matrix, $\hat{T}$, is given by;

$$\hat{T} = \begin{pmatrix} \cos(k_z d) & i\left(\frac{k_0}{k_z}\right)\sin(k_z d) \\ i\left(\frac{k_z}{k_0}\right)\sin(k_z d) & \cos(k_z d) \end{pmatrix} \tag{3.8}$$

Extending the problem across the interface between two layers with dielectric permittivi-

ties $\varepsilon_1$and ε_2, the transfer matrix $\hat{M}$ uses the continuity condition and can be written as;

$$\hat{M} = \hat{W}_1 \hat{W_2^{-1}} = \frac{k_{z2}}{2k_{z1}} \begin{pmatrix} 1+\frac{k_{z1}}{k_{z2}} & 1-\frac{k_{z1}}{k_{z2}} \\ 1-\frac{k_{z1}}{k_{z2}} & 1+\frac{k_{z1}}{k_{z2}} \end{pmatrix} \tag{3.9}$$

The corresponding layer and interface transfer matrices for TM polarization can be derived in a similar fashion and result in;

$$\hat{T} = \begin{pmatrix} \cos(k_z d) & \frac{ik_z}{\varepsilon k_0}\sin(k_z d) \\ \frac{i\varepsilon k_0}{k_z}\sin(k_z d) & \cos(k_z d) \end{pmatrix} \tag{3.10}$$

$$\hat{M} = \frac{\varepsilon_1 k_{z2}}{2\varepsilon_2 k_{z1}} \begin{pmatrix} 1+\frac{\varepsilon_2 k_{z1}}{\varepsilon_1 k_{z2}} & 1-\frac{\varepsilon_2 k_{z1}}{\varepsilon_1 k_{z2}} \\ 1-\frac{\varepsilon_2 k_{z1}}{\varepsilon_1 k_{z2}} & 1+\frac{\varepsilon_2 k_{z1}}{\varepsilon_1 k_{z2}} \end{pmatrix} \tag{3.11}$$

By forming the product of appropriate layer and interface transfer matrices, a transfer matrix for any arbitrary multilayered structure can be obtained. Once the transfer matrix of the arbitrary structure is obtained, the structure's transmission and reflection coefficients can be calculated. With the assumption that the amplitude of the incident light is unity, it can be written;

$$\begin{pmatrix} t \\ 0 \end{pmatrix} = \hat{F} \begin{pmatrix} 1 \\ r \end{pmatrix} \tag{3.12}$$

where $\hat{F}$ is the transfer matrix. t and r are the transmission and reflection coefficients respectively and can be expressed as;

$$t = \frac{1}{\hat{M}_{22}}; \quad r = -\frac{\hat{M}_{21}}{\hat{M}_{22}} \tag{3.13}$$

Using these transmission and reflection coefficients the reflectance and transmittance of a multilayered structure can be found. It is possible to describe a 3D device in 1D for initial simulations before verifying in 3D, to simplify the optimization process. In this work the TMM is used to optimize the reflectance of a dielectric stack. Code to perform the TMM was written in MATLAB. Once optimized the structure's reflectance is then verified in Lumerical FDTD, in both 2 and 3 dimensions.

3.3 Finite difference time domain method

Finite Difference Time Domain method (FDTD) is a modelling method developed by Kane S. Yee in 1966, that simulates the propagation of electric and magnetic fields [37]. Using

central finite difference approximations in the time and spatial domains, direct solutions of Maxwell's time-dependent curl equations are obtained. The biggest advantage of using FDTD is that a broadband source can be used and the response of the system to this source over a wide range of frequencies can be obtained in a single simulation[72]. The underlying theory of this method and identification of key features is given below.

To gain a better understanding of the Finite Difference Time Domain (FDTD) method the name can be broken down into two parts. 'Finite Difference' and 'Time Domain'. Finite difference is a numerical method, the finite difference method (FDM), whereby differential equations are solved by approximating them with difference equations, in which finite difference approximate the derivatives[66, 71]. FDM is the basic principle behind FDTD. To clarify this description, the increment of a function $f(x)$ at a point, x_0 is defined as;

$$\Delta f(x_0) = f(x_0 + \Delta x) - f(x_0) \tag{3.14}$$

The slope of the function $f(x)$ with respect to x is known as the difference quotient and can be written as;

$$\frac{\Delta f(x_0)}{\Delta x} = \frac{f(x_0 + \Delta x) - f(x_0)}{\Delta x} \tag{3.15}$$

As Δx approaches zero, the derivative of $f(x)$ with respect to x can be expressed as;

$$f\prime(x_0) = \lim_{\Delta x \to 0} \frac{\Delta f(x_0)}{\Delta x} = \lim_{\Delta x \to 0} \frac{f(x_0 + \Delta x) - f(x_0)}{\Delta x} \tag{3.16}$$

Therefore the derivative of a function can be approximated by its difference quotient when Δx is very small. There are three ways of approximating the first order derivative, the forward (3.17), backwards (3.18) and central difference (3.19) method, these can be expressed as;

$$f\prime(x_0) \approx \frac{f(x_0 + \Delta x) - f(x_0)}{\Delta x} \tag{3.17}$$

$$f\prime(x_0) \approx \frac{f(x_0) - f(x_0 - \Delta x)}{\Delta x} \tag{3.18}$$

$$f\prime(x_0) \approx \frac{f(x_0 + \frac{\Delta x}{2}) - f(x_0 - \frac{\Delta x}{2})}{\Delta x} \tag{3.19}$$

The FDTD method uses the second order central difference method applied to Maxwell's curl equations in the time and space domains. Maxwell's time dependent equations are a set of partial differential equations that form the foundation of classical electrodynamics. They describe electromagnetic wave propagation and are made up of Faraday's Law (3.20), Ampere's

Law (3.21), Gauss's Law (3.22) and Gauss's Magnetism Law (3.23). In an isotropic, linear medium, Maxwell's equations are as follows;

$$\nabla \times \vec{E} = -\frac{\delta \vec{B}}{\delta t} \tag{3.20}$$

$$\nabla \times \vec{H} = \vec{J} + \frac{\delta \vec{D}}{\delta t} \tag{3.21}$$

$$\nabla \cdot \vec{D} = \rho \tag{3.22}$$

$$\nabla \cdot \vec{B} = 0 \tag{3.23}$$

Where;
$\vec{E}$: electric field
$\vec{B}$: magnetic flux density
$\vec{H}$: magnetic field
$\vec{J}$: electric current density
$\vec{D}$: electric flux density
ρ: electric charge density

(3.20) and (3.21) are commonly referred to as the 'curl equations'. Faraday's Law describes how the electric field circulates around time varying magnetic fields and Ampere's law describes how the magnetic field circulates around time varying electric fields and electric currents. For isotropic, non-dispersive materials, the electric flux density is related to the electric field by;

$$\vec{D} = \varepsilon \vec{E} = \varepsilon_r \varepsilon_0 \vec{E} \tag{3.24}$$

And the magnetic flux density relation to the magnetic field is given by;

$$\vec{B} = \mu \vec{H} = \mu_r \mu_0 \vec{H} \tag{3.25}$$

Where;
ε: electrical permittivity
ε_r: relative electrical permittivity
ε_0: permittivity of free space
μ: magnetic permeability
μ_r: relative magnetic permeability

μ_0: permeability of free space

$\vec{J}$, the electric current density can act as an independent electric field energy source, $\vec{J}_{source}$, allowing for attenuation of the electric field by the isotopic non dispersive materials. This attenuation is the conversion of electric field energy to heat energy and can be written as;

$$\vec{J} = \vec{J}_{source} + \sigma\vec{E} \tag{3.26}$$

Where σ is the electrical conductivity. By introducing an equivalent magnetic current density term, $\vec{M}$, to Faraday's Law, an independent source for the magnetic field energy can be introduced and magnetic losses can be described. Faraday's Law becomes;

$$\nabla \times \vec{E} + \vec{M} = -\frac{\delta \vec{B}}{\delta t} \tag{3.27}$$

And conversion of magnetic field energy to heat energy can be written as;

$$\vec{M} = \vec{M}_{source} + \sigma_M \vec{H} \tag{3.28}$$

Where σ_M is the equivalent magnetic loss. (3.25) and (3.28) can then be substituted into Faraday's Law (3.27). Similarly (3.24) and (3.26) can be substituted into Ampere's Law (3.21) to give the 'curl equations' in isotropic, non-dispersive and lossy materials;

$$\frac{\delta \vec{H}}{\delta t} = -\frac{1}{\mu}\nabla \times \vec{E} - \frac{1}{\mu}\left(\vec{M}_{source} + \sigma_M \vec{H}\right) \tag{3.29}$$

$$\frac{\delta \vec{E}}{\delta t} = -\frac{1}{\varepsilon}\nabla \times \vec{H} - \frac{1}{\varepsilon}\left(\vec{J}_{source} + \sigma\vec{E}\right) \tag{3.30}$$

In order to compute solutions of these 'curl equations' they need to be in vectorial form. Vector components of the 'curl equations' in Cartesian coordinates can be written as a system of six coupled partial differential equations in the form;

$$\frac{\delta H_x}{\delta t} = -\frac{1}{\mu}\left[\frac{\delta E_y}{\delta z} - \frac{\delta E_z}{\delta y}\left(\vec{M}_{source} + \sigma_M H_x\right)\right] \tag{3.31}$$

$$\frac{\delta H_y}{\delta t} = -\frac{1}{\mu}\left[\frac{\delta E_z}{\delta x} - \frac{\delta E_x}{\delta z}\left(\vec{M}_{source} + \sigma_M H_y\right)\right] \tag{3.32}$$

$$\frac{\delta H_z}{\delta t} = -\frac{1}{\mu}\left[\frac{\delta E_x}{\delta y} - \frac{\delta E_y}{\delta x}\left(\vec{M}_{source} + \sigma_M H_z\right)\right] \tag{3.33}$$

$$\frac{\delta E_x}{\delta t} = -\frac{1}{\varepsilon}\left[\frac{\delta H_z}{\delta y} - \frac{\delta H_y}{\delta z}\left(\vec{J}_{source} + \sigma E_x\right)\right] \tag{3.34}$$

$$\frac{\delta E_y}{\delta t} = -\frac{1}{\varepsilon}\left[\frac{\delta H_x}{\delta z} - \frac{\delta H_z}{\delta x}\left(\vec{J}_{source} + \sigma E_y\right)\right] \tag{3.35}$$

$$\frac{\delta E_z}{\delta t} = -\frac{1}{\varepsilon}\left[\frac{\delta H_x}{\delta x} - \frac{\delta H_x}{\delta y}\left(\vec{J}_{source} + \sigma E_z\right)\right] \tag{3.36}$$

The vectorial form of the 'curl equations' (3.31-3.36) are the basis of the FDTD numerical algorithm and describes the interactions of electromagnetic waves with three-dimensional arbitrary structures.

3.3.1 The Yee Cell

The FDTD method provides discrete 'curl equations' in both time and space. The computation space is divided into a lattice of small cells, known as 'Yee cells'. A Yee unit cell in 3D FDTD space is shown in Figure 3.2, it can be seen that the unit cell is configured to ensure every electric field component is surrounded by four circulating magnetic field components and every magnetic field component is surrounded by four circulating electric field components. The field at each grid point at each time step is calculated by using the relation between the neighbouring cells. Applying central finite difference approximations to time and space derivatives of equations (3.31-3.36) explicit Yee FDTD equations are obtained. These equations are numerically solved in a leapfrog method, only the electric field components will be solved for one time step, then only the magnetic field components in the next time step. The leapfrogging continues until the specified number of iterations is met.

3.3.2 Boundary Conditions

The Yee algorithm does not explicitly contain any boundary information. Computers cannot store unlimited amounts of information so boundaries are a necessity. With the electric and magnetic fields calculated using information from their surrounding neighbours, a problem will occur at the boundaries, where field values outside the simulation region will be required to calculate field values inside the region. Without boundary conditions the FDTD method cannot solve problems practically. Typically the simulation region should be large enough to enclose the specified structure and boundary conditions applied to the region perimeters to simulate extension to infinity. Boundary conditions must suppress false reflections of outgoing waves for the FDTD solution to be valid at all time steps. Boundary conditions used in this work are called perfectly match layers (PMLs), these absorb electromagnetic waves incident upon them and are essentially reflectionless when the appropriate layers are chosen. PML is an absorbing boundary condition (ABC) developed by Berenger in 1994 [7, 9, 73]. The PML

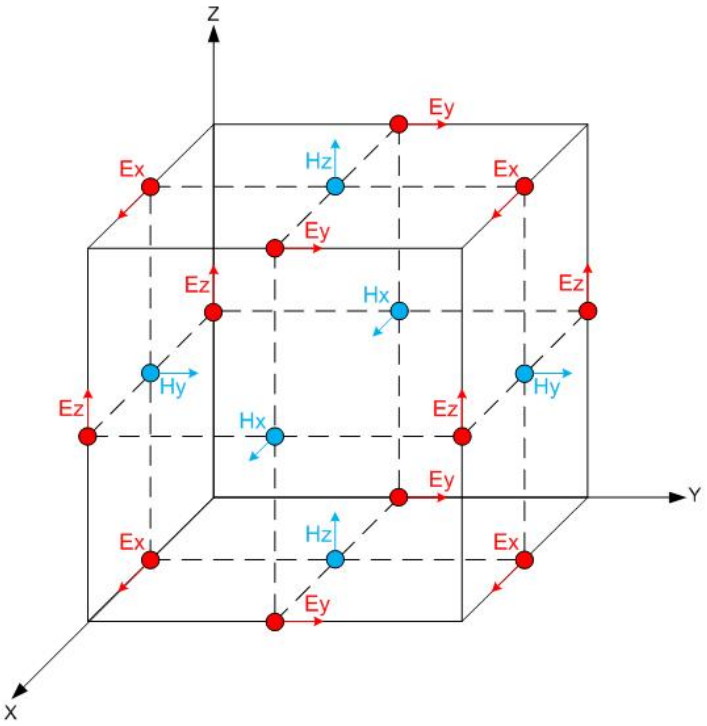

Figure 3.2: A schematic of the Yee unit cell, with the positions of the electric and magnetic field components

is an artificial anisotropic material that can be perfectly matched to free space for all incident angles and frequencies, one requirement of an PML is that the interface is an infinite plane.

3.3.3 Adaptive meshing

With a finite simulation region defined and appropriate boundary conditions applied, consideration is required on the distance between points at which the electric and magnetic fields are sampled, i.e. the size of the Yee cell. This is commonly referred to as the mesh. For numerical stability and accuracy at least 15 mesh cells per wavelength are needed. Using smaller mesh allows for more accurate representation of the structure that is being simulated however as the mesh becomes smaller the memory requirements and thus the simulations times increase. This leads to a trade off between accuracy (mesh coarseness) and simulation time. An added complication comes when non-rectangular structures are simulated, the Cartesian style mesh, as shown in Figure 3.3, means a round surface is approximated to a staircase grid. To optimize accuracy and simulation times, mesh is applied non-uniformly to a simulation region. Smaller mesh should be applied to regions of higher refractive index to maintain the number of mesh points per wavelength and in highly absorbing materials, to resolve penetration depths. Near

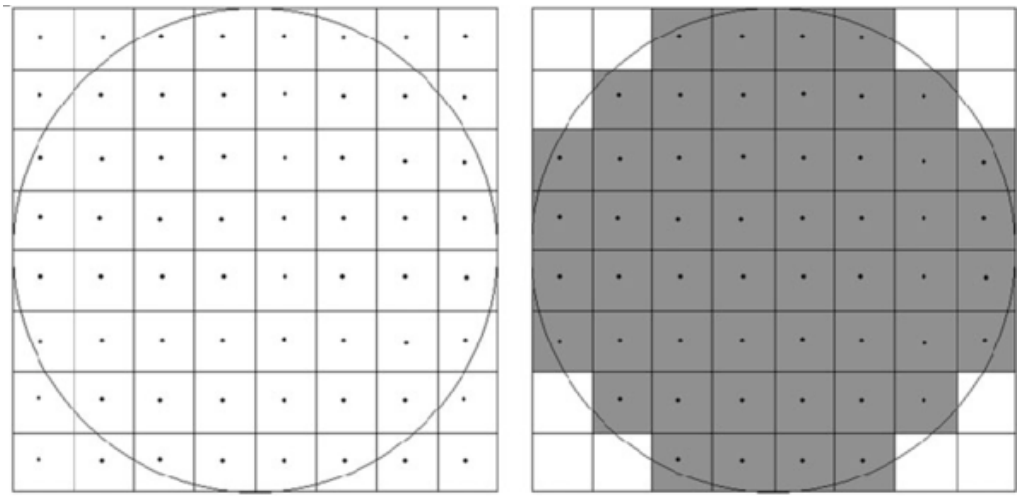

Figure 3.3: The grid (staircase) approximation of a circle in the FDTD simulation region. The 2D FDTD grid is made up of finite rectangular cells, a round surface (left) gets approximated to a staircase of rectangles (right), the smaller the mesh the better the approximation.

the surface of complex structures, where the fields are rapidly changing, smaller meshes are required for accurate results.

3.3.4 Sources

To observe the electromagnetic response in a simulation region, energy needs to be added to the system. From the vectorial form of the 'curl equations' (3.31-3.36), electric ($\vec{J}_{source}$) and magnetic ($\vec{M}_{source}$) sources are allowed. Many different types of sources can be chosen, with full control over spatial and temporal extents. The choice of point sources such as dipole sources are available, as well as regional sources such as total field, scattered field (TFSF). The source types used in this thesis are directional, such as plane waves and Gaussian beam sources. Plane waves are used to inject laterally uniform electromagnetic energy from one side of the region source, in 2D simulations the energy is injected along a line and in 3D simulations the energy is directed along a plane. Gaussian beam sources are better approximations to sources used in experiment. The Gaussian source defines a beam of electromagnetic radiation propagating in a specific direction. Its amplitude is a defined Gaussian cross section of a specified width, as shown in Figure 3.4. Highly focused Gaussian sources can also be modelled by using a thin lens source that injects a fully vectorial beam.

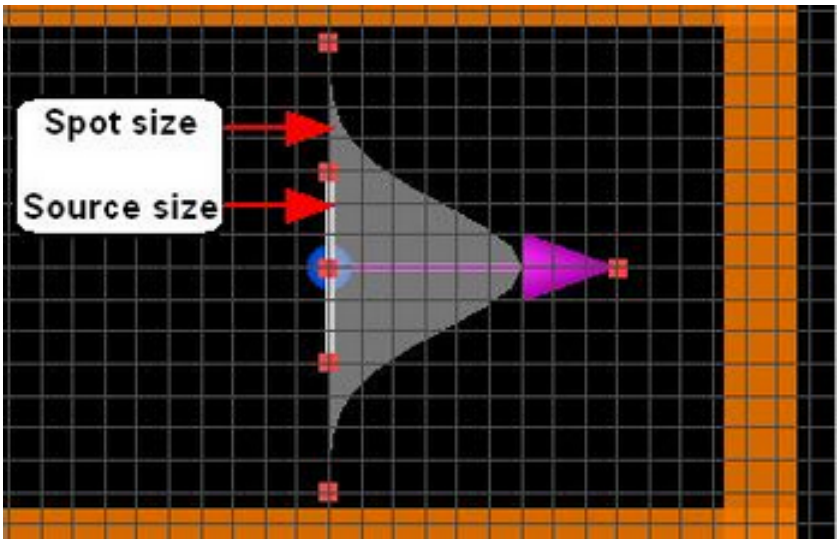

Figure 3.4: An unfocused Gaussian source propagating in the position x direction, a view from the Lumerical FDTD simulation region.

3.3.5 Far field Projections

Extending the simulation region to the far field is not practical due to the extremely large memory requirements, instead near field data is obtained from the simulation and used to calculate a far field projection as a post processing step. Far field projections can be seen as a decomposition of the near field data using a set of plane waves propagating at different angles and can be used to calculate the electromagnetic field anywhere in the intermediate and far field regions. For the far field projection to be valid electromagnetic fields must be known everywhere on a plane or closed surface made up of a single homogeneous medium, this medium must extend out to infinity with no additional structures beyond this plane. Far field projections are key to work done in this thesis as far field radiation patterns are studied for evidence of beaming. The near field data used is typically taken a wavelength's distance above the grating structure patterned on the exit of a subwavelength aperture.

3.3.6 Convergence

The accuracy of a simulation is determined by the model's convergence, the goal is to provide a self consistent model. Convergence can be used to determine the possible sources of error in a simulation, in FDTD simulations the main sources of error that have to be considered are from PML, mesh and dispersive material fit. The method of convergence is to vary a certain parameter until the results stop changing. If the PML is too close to a structure and the evanescent fields contact the PML, the resonance frequency will be altered, so the PML's proximity

should be altered and convergence of the simulation tested. Similarly any reflections from the PML will interfere with the source or scattered fields, PML is not completely reflectionless but the number of layers can be increased to minimize reflections. Convergence on the number of layers should be investigated. As discussed in section 3.3.3 the staircasing effect of the grid approximating structures is a source of error, while decreasing the mesh size reduces this error, there will always be a geometric error for a finite size mesh, testing convergence by decreasing the mesh size will help determine an acceptable level of error. The final source of error to be looked at is dispersive material fit, in FDTD it is not possible to use the dispersive refractive index as a function of wavelength directly. Instead the dispersive material properties are fitted to models that can be solved efficiently in the time domain, there is an error associated with this fit. By using different sources of dispersive refractive index of a material, such as Palik, CRC and Johnson and Christy, convergence can be investigated [14, 36, 59]. However fabrication precision should be taken into account, for example in FDTD you can define structures to 1nm precision but using the fabrication precision could be 10nm, it is unnecessary to achieve much higher precision in the simulation if it is being used to model experimental data.

3.4 Summary

In this chapter the computation methods employed to model the photonic structures designed in this thesis have been identified. The transfer matrix method (TMM) and finite difference time domain method (FDTD) have been described in detail. Explanations of how each method works are given by deriving key electromagnetic relationships. Important components that are used in the FDTD method are described, these are; boundary conditions, meshing, sources and far field projections. How each component can be used to improve efficiency and accuracy of the model have been described. Lastly sources of error and the method, convergence, of how to identify and reduce errors has been discussed.

Chapter 4

Device Design and Modelling Results

4.1 Overview

This chapter describes the design of a fully dielectric mid infrared band pass filter using the transfer matrix method (TMM). The design is then recreated in a 2D finite difference time domain method (FDTD) model. A subwavelength aperture is then created in the filter and near and far field results are illustrated. By applying a resonant nanograting to the exit side of the filter the effect of quasicylindrical waves (QCWs) on the near and far fields are presented. The nanograting design is then optimized and improvements to the full width half maximum (FWHM) of the far field are shown. Finally the model is expanded into three dimensions and the 2D results are successfully verified.

4.2 Design

Quasicylindrical waves (QCWs) can exist in the absence of surface plasmon polaritons (SPPs) on fully dielectric or perfectly electrically conducting (PEC) interfaces [43]. PECs do not exist in nature, this thesis will focus on the investigation of fully dielectric interfaces . In 2011 the existence of QCWs in the absence of SPPs was experimentally shown for the fully dielectric case, a silicon-air interface by Gan et al [23]. Focusing of light through a subwavelength aperture can be achieved by patterning the exit side of the aperture with a series of grooves, the theory behind this was covered in Chapter 2. In order to utilize such a structure there can be no transmission through the layer the aperture is situated in, this is straightforward for a metallic layer as it is highly reflective and as such a single thin film layer can be used. However dielectrics do not share this property; a single uniform layer of dielectric material will allow light to pass through it. One solution to achieve near zero transmission is to utilize

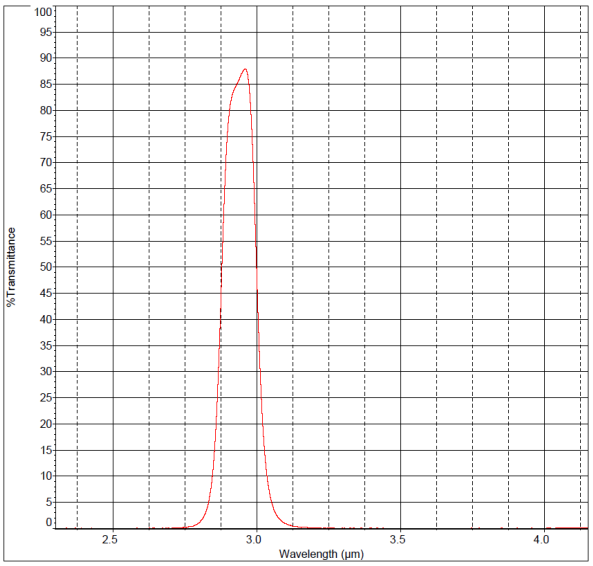

Figure 4.1: Mid-IR dielectric band pass filter transmission spectrum supplied by the manufacturer [55]

a stack of dielectric made up of layers of differing dielectric material, this takes advantage of interference effects described in Chapter 3. As an added complication the total thickness of the stack is limited by the fabrication of the subwavelength aperture, to achieve patterning on the nano-scale a focused ion beam (FIB) is used. The depth of focus of the focused ion beam (FIB) is typically around 20µm dependent on the beam current used, outside this zone the ion beam is unfocused and patterning is less precise. Therefore the total thickness of the dielectric stack should be no thicker than 20µm.

Thin dielectric stacks are commonly used in industry in the form of pass filters and one option would have been to purchase a commercially available infrared band pass filter and try to model it. The alternative would have been to design the dielectric filter ourselves, as from a modelling perspective this is straightforward and the transfer modelling method (TMM) can be used to obtain the ideal spectra. However, the designs of interference stacks are highly sensitive to layer thicknesses and the hardware to fabricate such a stack and achieve the precision needed would mean outsourcing to a optical coating company. The cost of a custom filter compared to an off-the-shelf product was too large to justify. It was decided to source an off-the-shelf mid-IR dielectric band pass filter from Northumbria Optical Coatings limited. The transmission spectra of the filter is shown in Figure 4.1, the band pass is centered at a wavelength of 2.91µm. Off-the-shelf filters are much more economically viable than the custom made alternative and successful demonstration of focusing from a subwavelength aperture using such a filter would make subsequent applications more appealing. To protect

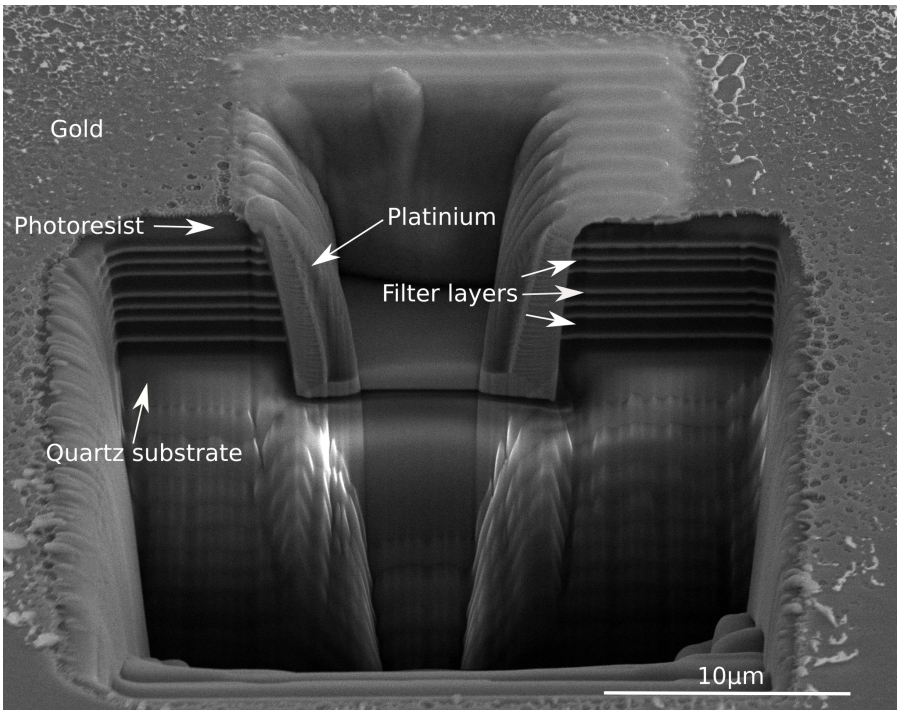

Figure 4.2: Scanning electron microscope(SEM) image of a cross section of dielectric band pass filter. Filter has a gold conducting layer to make it visible in SEM. Platinum was deposited during the cross section process, see Chapter 5 for details of this process.

their intellectual property (IP), Northumbria Optical Coatings Limited would not provide us with information on the dielectric materials used and the number and thickness of each layer in the filter. This presented challenges in modelling such a device.

More information about the filter would need to be obtained before modelling can begin. By taking a cross section of the filter using a focused ion beam (FIB), the thickness of the filter could be determined and the number of layers and thickness of each layer examined, Figure 4.2 shows a cross section through the mid-IR dielectric band pass filter from Northumbria Optical Coatings limited. The cross section shows 7 lighter bands and 3 extended dark regions which could be cavities. The filter was measured to be 9.1μm thick and is likely to be constructed from two dielectric materials, with one material having a substantially higher refractive index than the other. Using the transfer matrix method (TMM) described in Chapter 3, the estimated number of layers and their thicknesses were fitted to common dielectric materials known to be used in optical filters. Unfortunately a spectra close to the Northumbria Optical Coatings (NOC) filter was not obtained, it was concluded the dielectric materials present in the band pass filter were not commonly used in optical filters or that the filter was constructed from more than two dielectric materials. Instead, a more complex structure was used to model the filter response as described below.

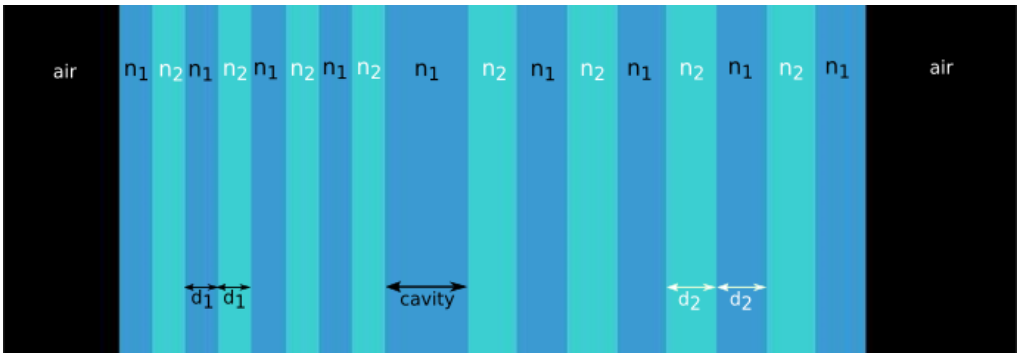

Figure 4.3: Schematic of the band pass filter designed using TMM method.

4.2.1 Dielectric Stack

A literature search was carried out into leading designs of infrared band pass filters and 1D photonic crystals and various configurations were modelled using the transfer matrix method (TMM). The design resulting in a spectrum and thickness that most closely matched the Northumbria Optical Coatings filter consisted of combining two quarter-wavelength stacks and a single cavity, each quarter-wavelength stack comprising of 9 alternating layers of high and low refractive index dielectric. A schematic of this filter is shown in Figure 4.3.

The filter was optimized to have a narrow band-pass at 2.91μm, this was achieved combining a high pass filter with a low pass filter and tuning the thickness to achieve an overlap of the pass regions of each filter. The first stack acted like a high pass filter by setting the thickness of each layer to 20% of the band-pass wavelength 2.91μm, resulting in each layer being 582nm across, with the first and last (9th) layers consisting of the dielectric with the higher refractive index. The second stack acted like a low pass filter by tuning the thickness of each layer to 30% of the band-pass wavelength, each layer is 873nm across, as before the first and last layers consisted of the dielectric with the higher refractive index. The higher index dielectric was stibnite, with a refractive index of 2.72 at the band pass wavelength and chiolite was chosen to be the lower index dielectric with a refractive index of 1.332 at the band pass wavelength. The filter has a total thickness of 13.1μm, similar to that of the NOC filter. The resulting spectrum is shown in Figure 4.4.

4.2.2 Subwavelength aperture

The geometry for the mid-IR dielectric narrow band pass filter modelled using the TMM was then recreated in two dimensional space using the Lumerical FDTD software. A broadband plane wave source was placed 3μm away from the incident side of the filter and its transmittance and reflectance measured using frequency monitors placed either side of the filter. This

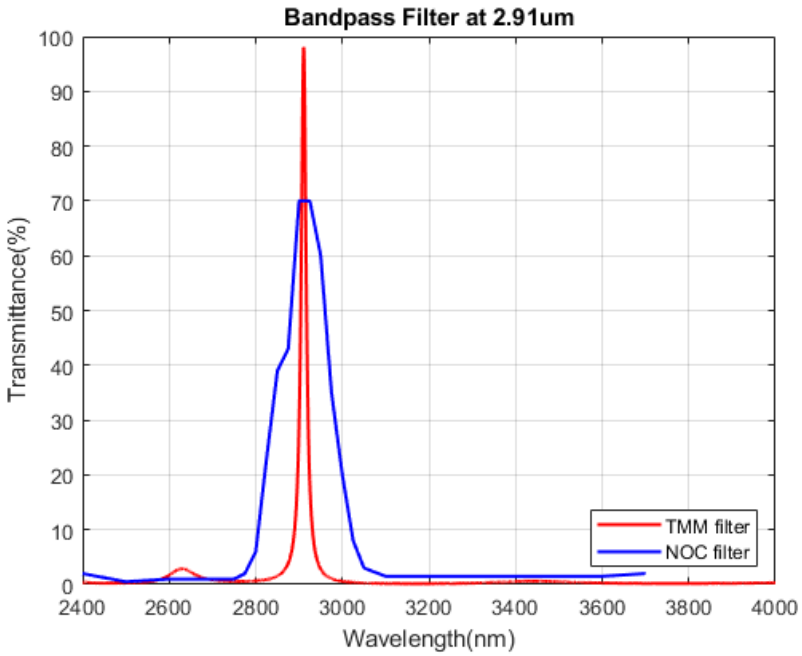

Figure 4.4: Transmission spectra of the dielectric stack designed with the TMM (red). Transmission spectra of the NOC bandpass filter (blue)

was repeated in three dimensional space to fully verify the TMM results.

For the following work a resonant wavelength of 3.4μm was chosen. 3.4μm has enough clearance above the filter's band pass for the Gaussian source's spectral width to not overlap and is in a part of the mid-IR spectrum used in many industrial applications. Starting with two dimensional space, a subwavelength aperture with a width of 850nm (quarter wavelength) was then created through the band pass filter. A plane wave source was placed on the incident side of the filter and a frequency domain power monitor was placed at a distance of 500nm from the aperture exit to record near field data. This data included the electric and magnetic field components, transmission, power and Poynting vectors along the Y plane. A conformal mesh was applied to the simulation region with an override mesh applied to the region inside the subwavelength aperture for increased accuracy, with a mesh cell size of $1nm^2$. The model setup is illustrated in Figure 4.5. Initially the geometry shown in Figure 4.6 was investigated.

Perfect electrically conducting aperture sidewall

The near field data was analysed and there was found to be a significant amount of radiation exiting the filter away from the subwavelength aperture. By placing frequency domain power monitors in the X plane through the filter either side of the subwavelength aperture, the source of this radiation was found to be light escaping through the sidewalls of the subwavelength

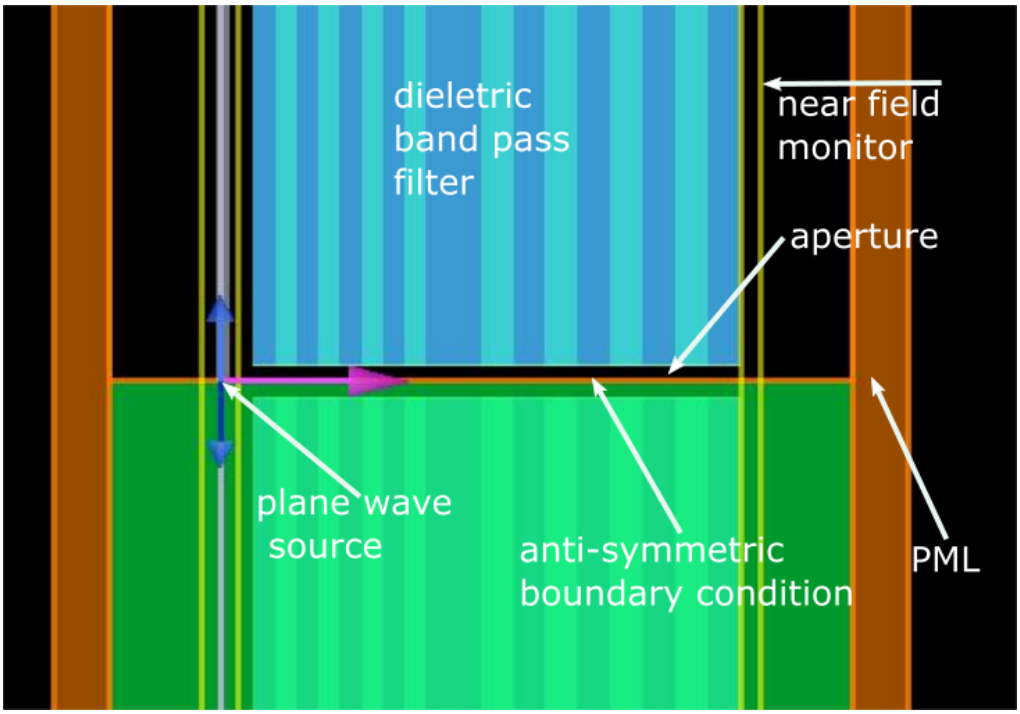

Figure 4.5: FDTD Model Setup, blue arrows on source denote the electric field component direction and purple arrow the source direction

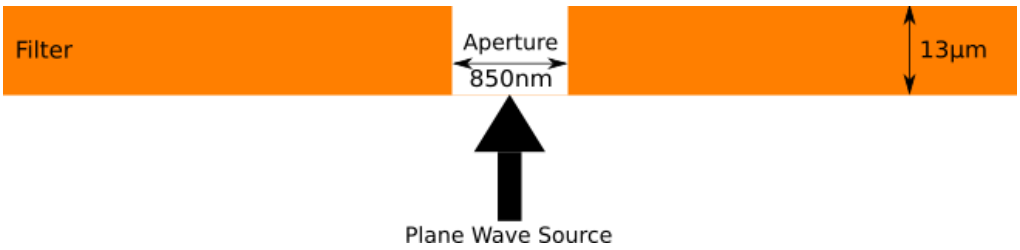

Figure 4.6: Geometry of the structure modelled in FDTD, with an aperture and no grooves.

aperture. To evaluate the impact this has on the far field, the near field data collected by the Y plane monitor situated at the exit side of the filter was projected to create a 2D far field XY map. Figure 4.7 shows the effect of lighting escaping through the sidewalls on the light emitted from the exit side of the filter. The impact on the far field is unacceptable and any beaming effects would be overpowered by radiation escaping from the sidewalls.

To prevent this from happening a layer of 50nm thick perfect electrical conductor (PEC) was placed on the sidewalls of the subwavelength aperture, this will reflect light incident on the sidewalls back into the subwavelength aperture. PEC was chosen because it does not support surface plasmon modes and nullifies the electric field inside the PEC, cutting down on simulation time. The effect of adding 50nm of PEC to the sidewalls of the subwavelength

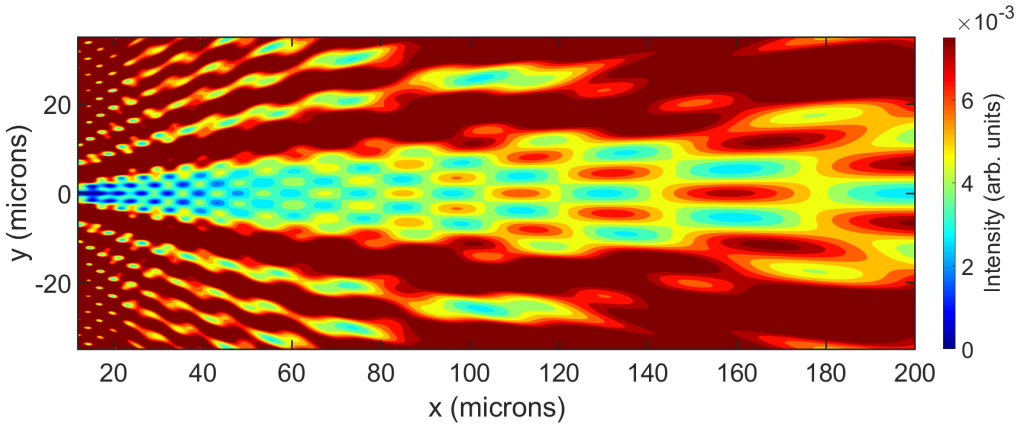

Figure 4.7: Electric field intensity on the exit side of the filter when no PEC was placed on the aperture. Incident light wavelength 3.4μm.

aperture can be seen in Figure 4.8. No radiation passes through the filter away from the subwavelength aperture, leaving a highly divergence beam caused by scattering at the exit of the subwavelength aperture. This will allow the role of QCWs in focusing the re-radiated light to be investigated.

If light escaping through the sidewalls of the subwavelength aperture is found in experiment, metal may have to be deposited on the sidewalls. However, in practise it would not only be technologically challenging to coat only the sides of the nanoaperture with metal, the presence of a metallic layer could also confuse the interpretation of the results. Initial experiments (as described in the following chapter) were therefore undertaken without coating the aperture sides, but with the expectation that ultimately a route may have to be found to define a mode within the aperture. This could perhaps be achieved, for example, by the use of a dielectric photonic crystal, thus retaining the fully dielectric nature of the device.

4.2.3 Nanograting

When light exits a subwavelength aperture, it is scattered in all directions resulting in a highly divergent beam, this is clearly shown in Figure 4.9 which was created by projecting the near field data onto the XY plane to obtain the far field. To reduce the divergence of this beam, a series of resonant nanogrooves can be added to the exiting side of the band pass filter resulting in a nanograting. The mechanics behind resonant nanogratings is described in Chapter 2. The initial geometry for such a grating is shown in Figure 4.10. The initial dimensions for; the first groove to aperture distance, groove depth, groove width and number of grooves were taken from Gan et al [22], where a nanograting resonant at 3μm was patterned onto gold and tungsten. The grating constant (distance between grooves) was then changed to 3.4μm to move

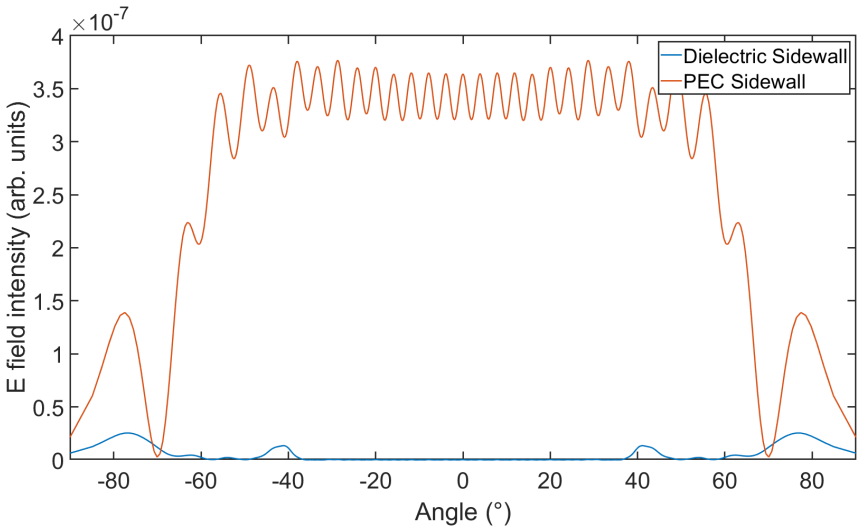

Figure 4.8: Electric field intensity one metre from exit side of filter for a subwavelength aperture with PEC sidewalls (red) vs dielectric sidewalls (blue). Incident light wavelength 3.4μm.

away from the band pass (transparent) region of the filter, this should serve as a good initial approximation to observe a reduction of the beam's divergence as a result of QCWs scattered by the nanograting. Another mesh override region was added to the nanograting region where fields will rapidly change due to scattering from the nanogrooves. The near field behavior and projected far field can be seen in Figure 4.11 for the resonant nanograting patterned onto the modelled band pass filter. The beam divergence has been greatly reduced as illustrated in Figure 4.12. In the far field at a distance of one meter from the filter, the full width half maximum (FWHM) of the radiated beam improves from 129.8° for the isolated subwavelength aperture with no nanogrooves to 4.1° for the subwavelength aperture surrounded by nanogrooves, this shows that QCWs can be successfully used as the sole mechanic for focusing the highly divergent light radiated from a subwavelength aperture.

4.3 Optimization

The reduction in divergence can be improved upon further by optimizing the geometry. The geometry for the resonant nanogratings was optimized by running a number of simulations iterating through ranges for each of the grating dimensions; aperture to first groove distance, groove depth and groove width. The ranges for each parameter were determined by running a series of coarse optimizations and observing where peak power of the far field at an angle of zero degrees dropped significantly. The ranges were as follows; 1 to 3μm for the aperture

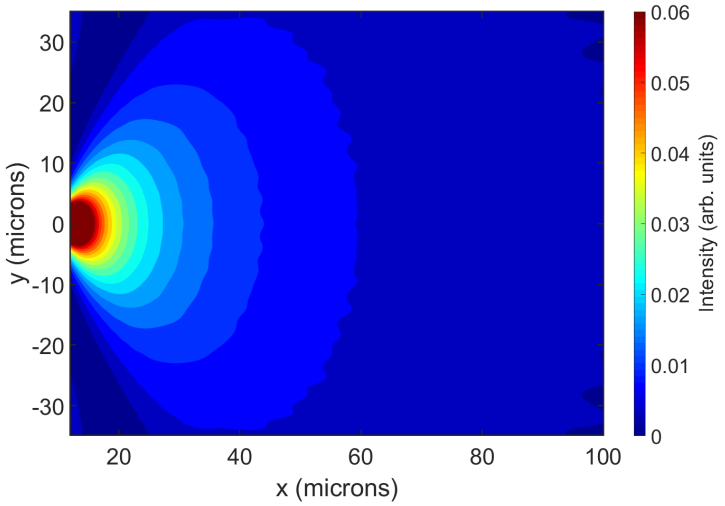

Figure 4.9: Far field intensity of an isolated subwavelength aperture. Incident light wavelength 3.4μm.

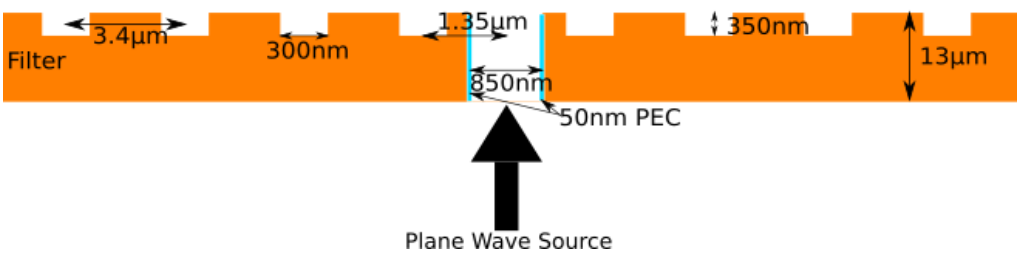

Figure 4.10: Initial aperture groove geometry used in FDTD simulations.

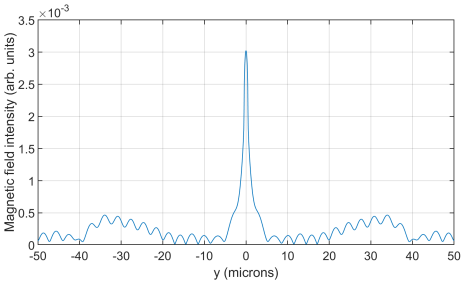

(a) Magnetic field strength along the surface of the filter. Incident light wavelength 3.4μm.

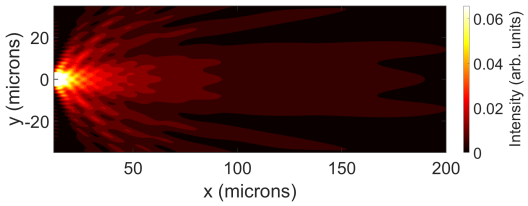

(b) Intensity of electric field on the exit side of the filter.

Figure 4.11: Near and far fields for the initial geometry. Incident light wavelength 3.4μm.

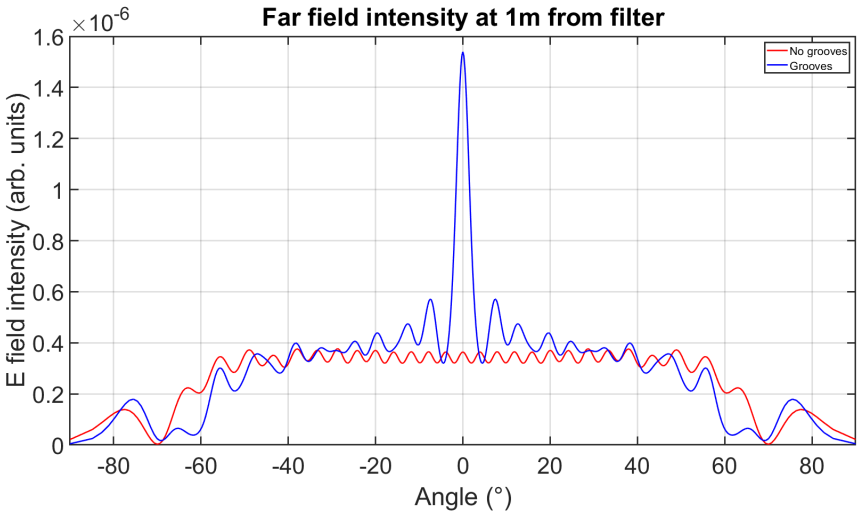

Figure 4.12: Electric field intensity one metre from exit side of filter, grooves (blue) vs aperture only (red)

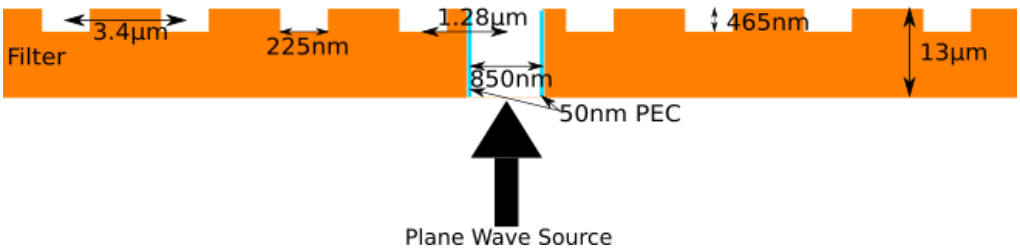

Figure 4.13: Optimized geometry used in FDTD simulations.

to first groove distance, 150 to 550nm for the groove depth and 100 to 500nm for the groove width. The parameters were optimized around maximizing the peak electric field intensity at a distance of one meter from the filter, this coincides with the zero degree electric field intensity.

A second optimization around minimizing the FWHM of the electric field at one meter from the filter was carried out and gave the same result, the scripts written for finding the zero degree electric field intensity. Lumerical uses an optimization algorithm which is a population based stochastic optimization technique called the 'Particle Swarm Optimization'. The optimization geometry is shown in Figure 4.13, the groove depth and width were optimized to the nearest nanometer and the first groove to aperture distance was optimized to the nearest 10nm.

The amplitude of the total magnetic field H along the Y plane of the nanogratings is shown in Figure 4.14, it can be seen that a standing wave with decaying amplitude is sustained along the Y plane. Due to the mixture of vectors associated with the quasicylindrical wave (QCW), the QCW is not as strongly trapped when compared with surface plasmon polaritons (SPPs) which have a well-defined wavevector. This contrast is seen as the magnetic field falls off after several wavelengths. In a metallic nanogroove system employing SPPs to re-radiate, the H field falls off much faster, typically after the first couple of grooves, indicating that part of the energy of the SPP that emerges from the subwavelength aperture is strongly trapped within

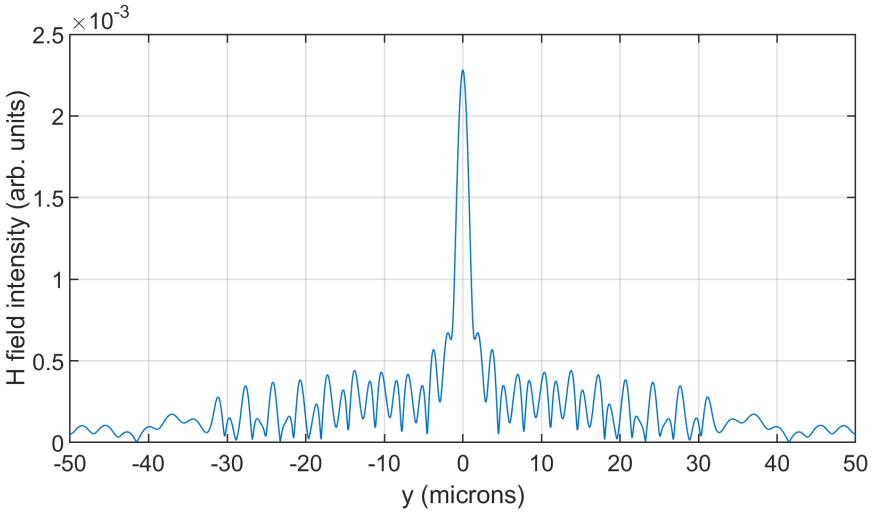

Figure 4.14: Magnetic field strength along the exit side surface of the filter for optimized geometry. Incident light wavelength 3.4μm.

the nanogrooves. Another feature characteristic of QCWs which is shown in Figure 4.14 is the rapid decay of the field between the subwavelength aperture and first nanogroove.

The projected far field, Figure 4.15, shows a directional radiation pattern with an increased peak intensity when compared with the initial geometry's projected far field (Figure 4.11).

The effect of an optimized geometry can be illustrated by contrasting the electric field amplitudes and FWHM, at one meter from the filter, before and after the optimization has taken place. Figure 4.16 shows that the FWHM of the beam has been improved from 4.1° to 3.4° with the peak electric field intensity greatly increased.

4.3.1 3D FDTD

The simulation was expanded to three dimensional space to match experimental work as closely as possible, as well as verifying the findings of the 2D simulations. The 3D geometry is shown in Figure 4.17, the grooves and aperture were made 50μm long to aid with finding and illuminating the nanograting with the OPO laser in experiment.

Full illumination of the entire length of the aperture from a plane wave source was first done to verify the 2D simulations. The total magnetic field intensity H produced along the XY plane is shown in Figure 4.18, it is possible to see distinct areas of higher intensity.

These areas are illustrated more clearly by observing the Poynting vectors of the near field, as shown in Figure 4.19, to show the magnetic field direction. The areas of higher intensity are likely caused by interference in the subwavelength aperture.

The near field was then projected along a hemisphere one meter from the filter to obtain a

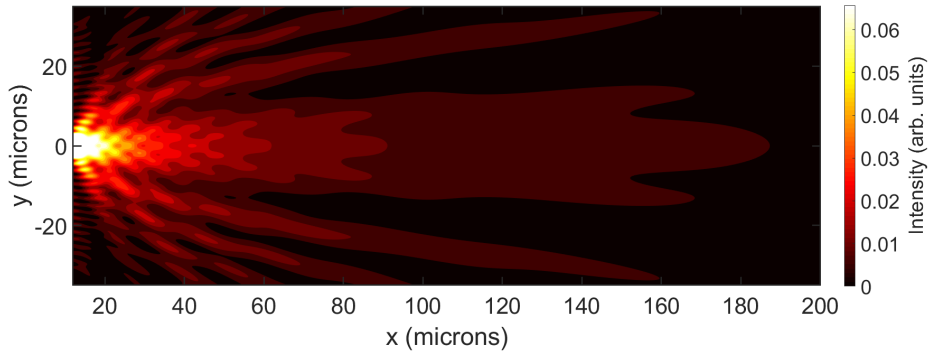

Figure 4.15: Optimized geometry electric field intensity. Incident light wavelength 3.4μm.

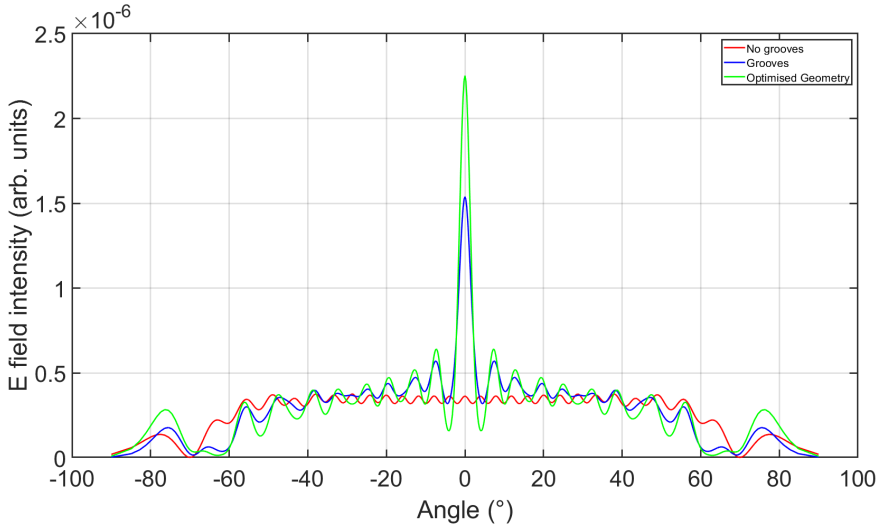

Figure 4.16: FWHM comparison between the aperture only (red), initial geometry (blue) and optimised geometry (green). Incident light wavelength 3.4μm.

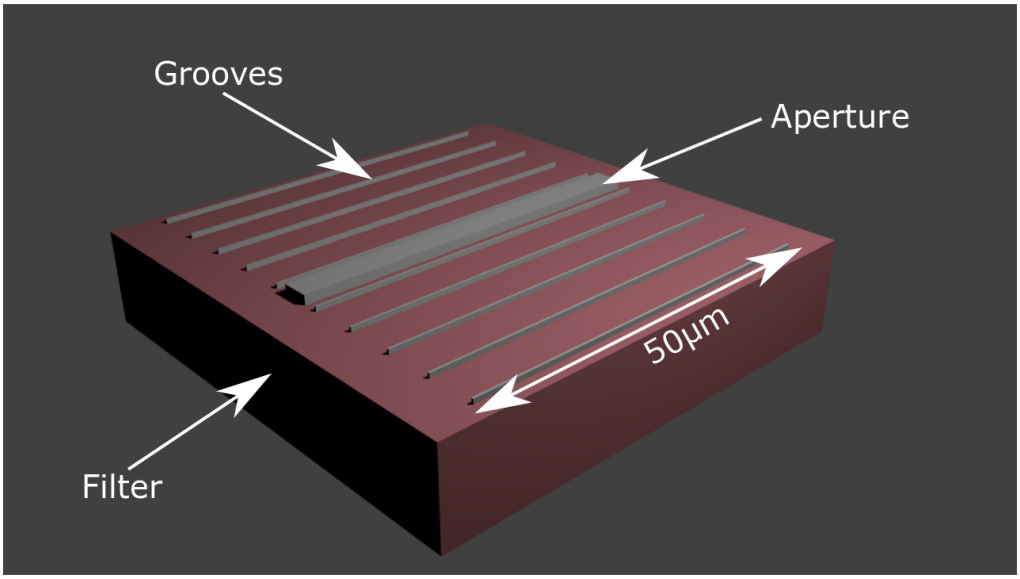

Figure 4.17: Geometry used for the 3D FDTD simulations.

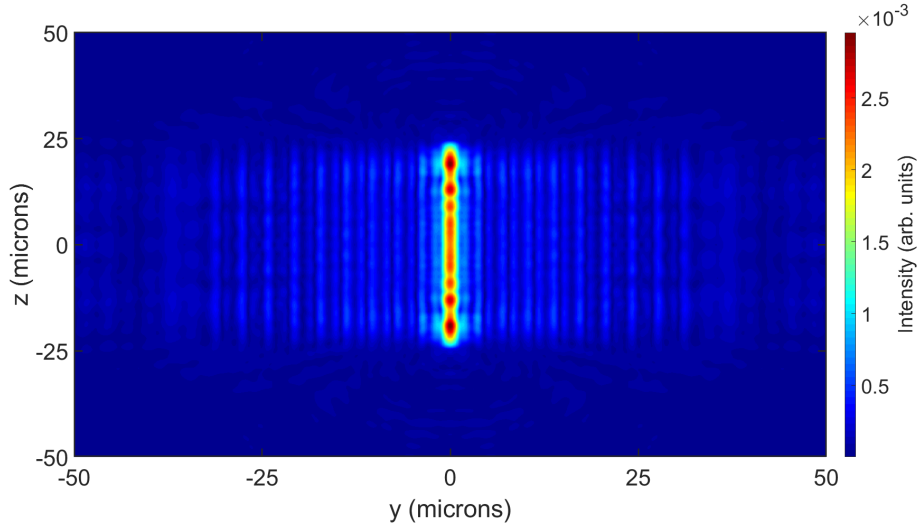

Figure 4.18: Magnetic field on the exit surface of the filter. Incident light wavelength 3.4μm.

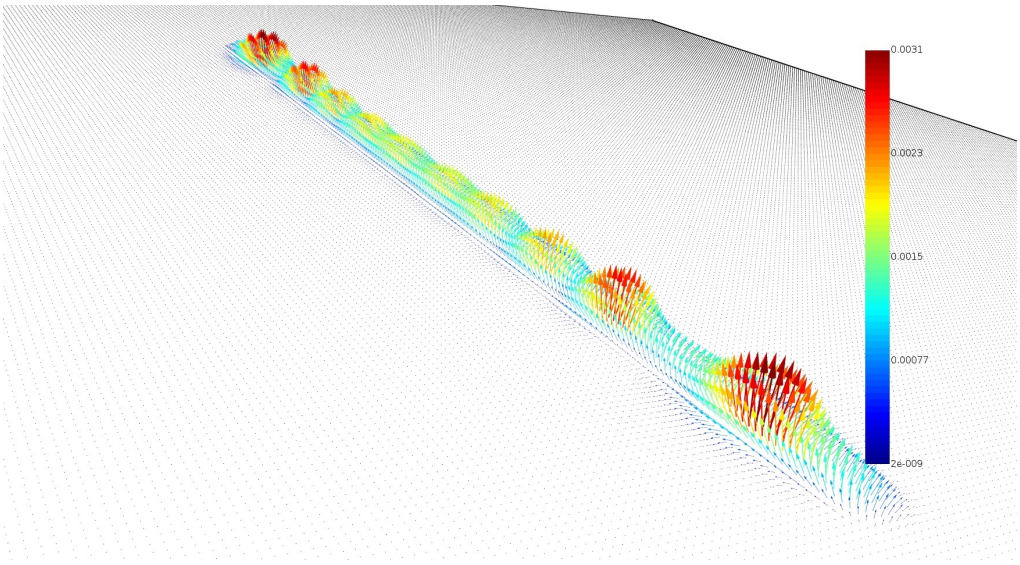

Figure 4.19: Poynting vectors for the aperture exit. Incident light wavelength 3.4μm.

far field radiation pattern, the resulting electric field intensity is shown in Figure 4.20.

To gain insight to observations made in the measurement system, a focused Gaussian source was used to mimic the OPO laser being focused by a reflecting objective lens (as used in experiments) onto the filter, the near and far fields were obtained. Comparing this with the near and far field from the plane wave source simulation there was no difference, it was concluded the plane wave approximation can be made. Far field projections serve as a prediction for what will be seen in experiment as well as allowing for far field data taken by experiment to be backwards engineered to estimate what the near field could look like.

4.4 Summary

In this chapter the design of a mid-infrared dielectric narrow band pass filter, that closely matches the off-the-shelf filter sourced for this project, has been achieved by using the transfer matrix method (TMM). This design was then verified using Lumerical FDTD in two and three dimensions. 2D numerical results of applying a subwavelength aperture to the filter have been presented and the effect of patterning the exit side of filter with a nanograting has been shown. The full width half maximum (FWHM) of the electric field intensity at a distance of one meter from the filter has been reduced from 129.8° for the isolated subwavelength aperture with no nanogrooves to 4.1° for the subwavelength aperture surrounded by nanogrooves, illustrating that QCWs can be successfully used as the sole mechanic for focusing the highly divergent light radiated from a subwavelength aperture. The nanograting geometry was then

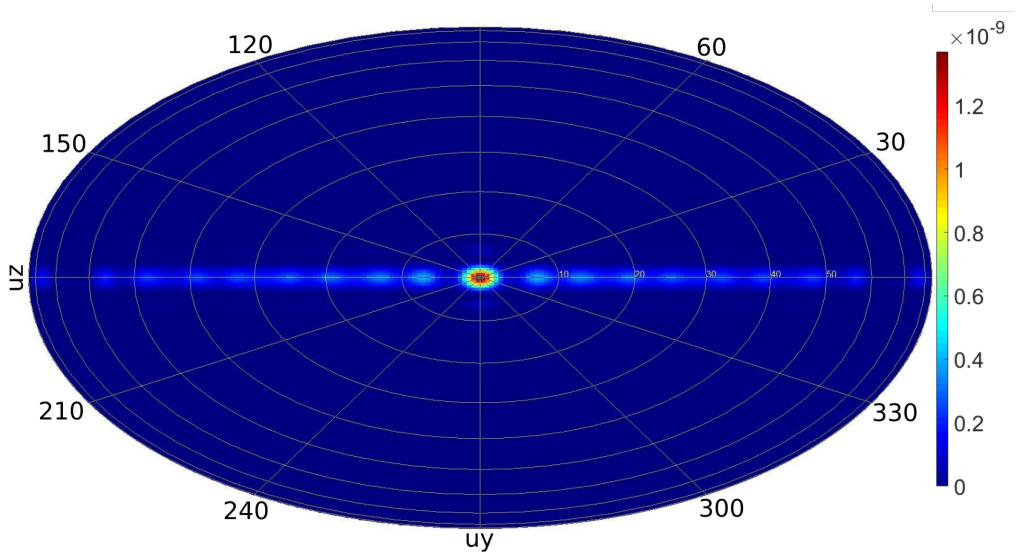

Figure 4.20: Far field intensity one metre from the exit of the aperture. Incident light wavelength 3.4μm.

successfully optimized and the FWHM further reduced from 4.1° to 3.4° with peak electric field intensity greatly increased. The investigation was then expanded to 3D and the 2D results were verified along with investigations into the plane wave source approximation.

Chapter 5

Fabrication and Measurements

5.1 Introduction

This chapter describes the fabrication steps, including using the focused ion beam, to pattern the 1D Quasicylindrical (QCW) grating onto a dielectric filter. Optical measurements were performed on a series of samples, this chapter describes the experiment instrumentation employed for measurements. Initial measurements to validate the optical system are also shown.

5.2 Fabrication overview

5.2.1 Fabrication Process

Mid IR dielectric band pass filters were sourced from Northumbria Optical Coatings limited. The filters are to be patterned using a focused ion beam and to protect the filters from damage a film of photo-resist is added to the dielectric surface. To prevent charge build up and so the sample can be viewed by an scanning electron microscope (SEM) a conducting layer is added onto of the photo-resist layer. Once the FIB patterning is completed acetone can then be introduced to the photo-resist layer, which will dissolve it so that the conducting layer can be lifted off, leaving a fully dielectric patterned filter.

5.2.2 Sample Characteristics

The band pass filter used has a 1mm thick fused quartz substrate with single side dielectric coatings. Light is blocked out from 2.2μm up to 4.3μm, with a narrow band pass at 2.914μm, the optical response of the filter is shown in figure 5.1.

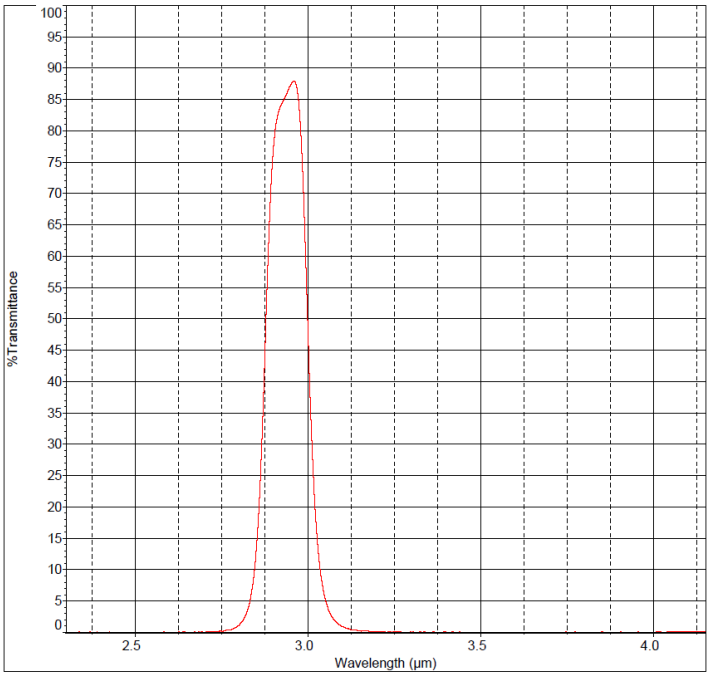

Figure 5.1: Optical response of dielectric band pass filter source from Northumbria Optical Coatings limited.

Photo-resist layer

To protect the filters from damage in the focused ion beam, a layer of ~150nm of polymethyl methacrylate (PMMA) is transferred directly onto the top surface of the band pass filter. The PMMA solution used for this is a 950K A4 solution, where 950K is the molecular weight and A4 is the ratio, 2:1, of PMMA to the solvent, anisole. A spinner was used to deposit the PMMA solution onto the dielectric filter surface. The thickness of the PMMA is determined by the RPM of the spinner, molecular weight of the PMMA and the total spin time. The required parameters to get a 150nm layer of PMMA was 3250 RPM for 55seconds. Once the spinning process is completed the solvent is removed by placing the filter on a hot plate and baked for 10 minutes at a temperature of 150ºC.

Conducting layer

A conducting layer was deposited onto the PMMA to prevent charge build up during the patterning process. A thermal evaporator was used to deposit 80nm of gold on top of the PMMA layer. The filter along with the gold is placed into the thermal evaporator's vacuum chamber, which is pumped down to a pressure of ~2x10^{-6}mbar. The gold is placed into a crucible, which is resistively heated, causing the gold to evaporate. The gold then condenses

Figure 5.2: FEI Nova 600 system located in the Nanofabrication laboratory at the University of Exeter.

on the much cooler filter, forming a thin metallic film. The rate of evaporation is controlled by the magnitude of the current applied to the crucible.

5.2.3 Focused Ion Beam

The focused ion beam (FIB) technique was developed during the late 1970s, with the first commercially available systems appearing in the mid 1990s [49]. These systems were primarily produced and developed for large semiconductor manufacturers [60]. A FIB system operates in a similar way to a scanning electron microscope (SEM) except instead of a beam of electrons, a FIB system uses a highly focused beam of ions. The FIB system can be used at high beam currents for localized sputtering or at low beam currents for imaging although many modern systems incooperate a separate SEM beam to be used for imaging. The 3 largest manufacturers of these FIB/SEM dual-beam systems are FEI, Toshiba and Zeiss [2]. The system used in this work is the Nova 600 from FEI, located in the Nanofabrication laboratory at the University as shown in Figure 5.2.

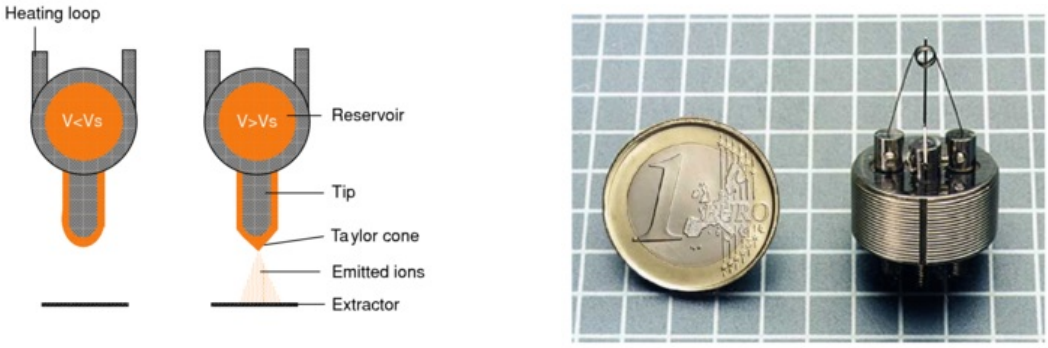

Figure 5.3: Schematic of needle type liquid metal ion source (left), image of assembled source, mesh scale is 5mm (right) [45].

Overview

This section is designed to give an overview of the basic operation of the FIB system used in this work, the FEI Nova 600. Starting with how the ions are produced right through to how they interact with the sample.

Liquid Metal Ion Source

FIB systems use liquid metal ion sources (LMIS), there are several different designs of LMIS such as capillary-type and impregnated-type with the most widespread design being the needle ionizer, as shown in Figure 5.3 [57]. The needle type LMIS consists of reservoir of liquid metal that feeds a blunt tungsten tip with radius of a few microns and a extractor aperture situated at the tip. The reservoir is heated and the liquid metal wets the tungsten tip, when an electric field ($> 10^{10} Vm^{-1}$) is applied at the tip it opposes the force of the surface tension forming the liquid metal into a cusp shaped tip, called a Taylor-Gilbert cone [57, 69]. The tip radius of this cone is typically a couple of nanometers and the large electric field causes ionization and field emission of the liquid metal atoms. The ions generated at the apex of the cone go towards the extractor aperture forming an ion beam.

The metal used as the LMIS needs to have a high surface tension, low vapor pressure in its liquid state and not be corroding to the tip itself. Several different metals and alloys are used for different applications such as Ir, Au and Cu [57]. Most FIB systems are used for micro-machining applications and only use a single source. The most widely used source is gallium (Ga), it has a low melting point of approximately 300K meaning a Ga LMIS can operate at room temperatures. Ga LMIS's are easy to fabricate and with a tungsten (W) substrate they are reliable, stable and have long lifetimes.

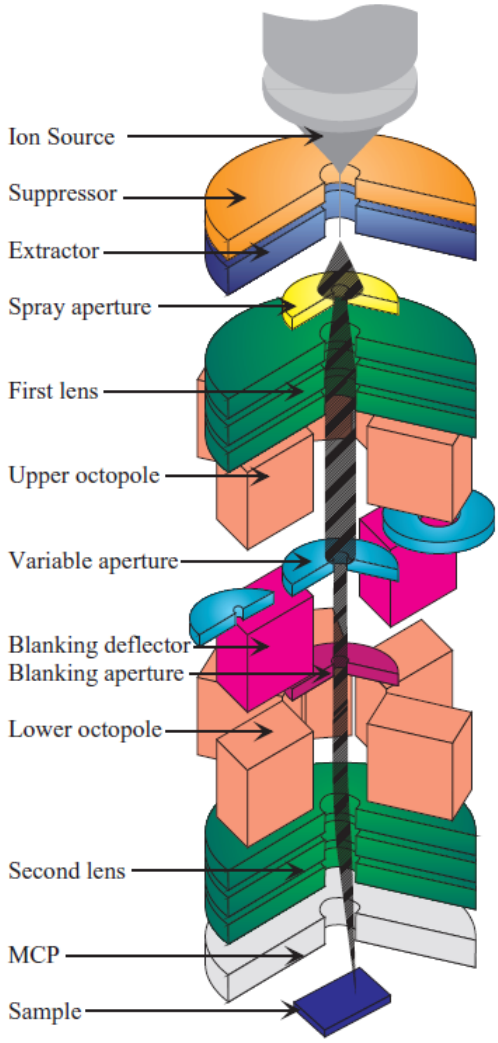

Figure 5.4: Schematic of an ion column [63].

Source to Sample

A schematic of a typical FIB column is shown in Figure 5.4. Upon exiting the extractor aperture the ion beam is condensed in the first electrostatic lens, passing through the upper octopole which adjusts the beam stigmatism. Using a series of variable apertures the beam current can be varied from 1pA to 10nA, allowing for a fine beam for high-resolution imaging through to a coarse beam for fast and rough large area milling. The lower octopole is used for raster scanning of the beam over the sample, which is mounted in a vacuum chamber. The second electrostatic lens focuses the beam to a point on the sample, for a 1pA, 30keV ion beam, the focal point is ~8nm. Larger beam currents result in larger focal points.

Sample interaction with Ions

Etching is achieved by bombarding precisely defined areas with Ga ions. The result of interactions between the ion beam and a solid surface are caused by a small number of physical processes. The results of these processes are very different to similar interactions seen in a scanning electron microscope. Due to the much larger mass of the Ga ions, incident ions can cause displacement of atoms in the target surface, this is a very useful phenomena and is employed to make, break and alter structures on small scales.

Interactions between incident ions and target atoms can be broken down into two categories; elastic and inelastic. The inelastic process which results in the formation of secondary electrons is useful for imaging. However since the SEM was used to image in this work, the elastic interactions will be the focus here. Sputtering occurs at the surface when the incident ions transfer enough momentum to the surface atoms to free one or more target atoms, this interaction is used to alter the structural shape of the target.

A small number of these target atoms are ionized and together with their corresponding electrons contain information about the sample and they form simultaneous images. The Ga ions will either undergo Auger neutralization and be reflected, escaping the sample or they will lose all their energy, implanting themselves on the target material. The distance into the sample at which the ion becomes trapped at is known as the projected range, R_p [28]. An overview of these processes is described in Figure 5.5.

The implanted Gallium can be expelled from the target material by annealing the sample for one hour at a temperature of approximately 700ºC in air [65]. It has been demonstrated that the formation of gallium-oxide platelets on the surface can be reduced by first annealing the sample in a vacuum, then performing the same procedure again in oxygen followed by plasma cleaning [67].

Material Deposition

The FEI Nova 600 has a gas injection system (GIS) that allows for preferential milling or material deposition depending on which precursor material is chosen. The GIS consists of a heated crucible, where the precursor is stored, screwed into a needle, each precursor has its own individual crucible and needle allowing for rapid switching between precursors. During operation the precursor is delivered to the sample by moving the needle tip 100µm above the sample's surface, this small distance means the gas pressure doesn't have to be high and can be localized to a targeted area of the sample [21]. One of the most common uses of the GIS is to deposit a conductive material, such as platinum, onto a sample's surface [64]. The precursor for platinum is trimethyl platinum ($C_6H_{16}Pt$), which is heated to its working temperature of

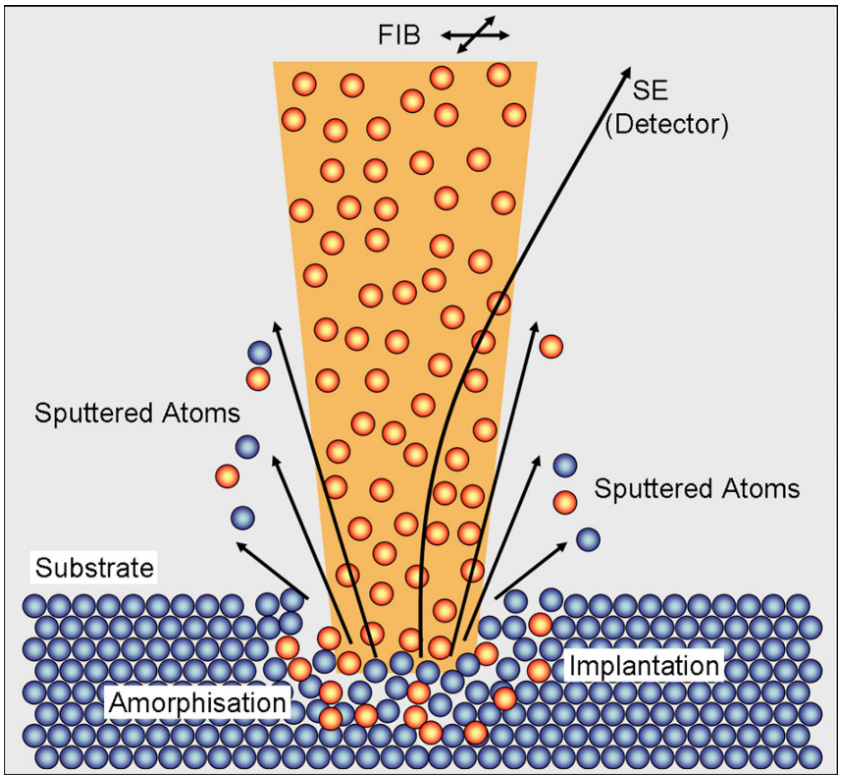

Figure 5.5: Ga ion-sample interaction [74].

40ºC and delivered to the sample's surface as shown in Figure 5.6. The ion beam activates the gas to leave a protective platinum layer. Deposition is a delicate balance between decomposing the adsorbed gas and sputtering the deposited material. This balance depends on parameters such as Needle position, crucible temperature, beam current and the scan area and speed, an example of this balance can be seen in figure 5.7. Due to the nature of the samples that were patterned in the FIB preferential milling was not used and will not be discussed here.

Patterning Method

During patterning the beam unblanks automatically and uses digital beam placement to vector scan over a pattern. Using the xT Nova NanoLab software there are 3 different options for patterning; predefined patterning tools, importing a bitmap file and importing a stream file. The predefined patterning tool options are typically used to pattern more basic shapes and cross sections and important properties such as dwell time, beam overlap and pitch can be customized here.

In a bitmap file each pixel consists of a red, green and blue component (RGB). The red component is ignored by the software, the green determines if the beam is blanked, with a

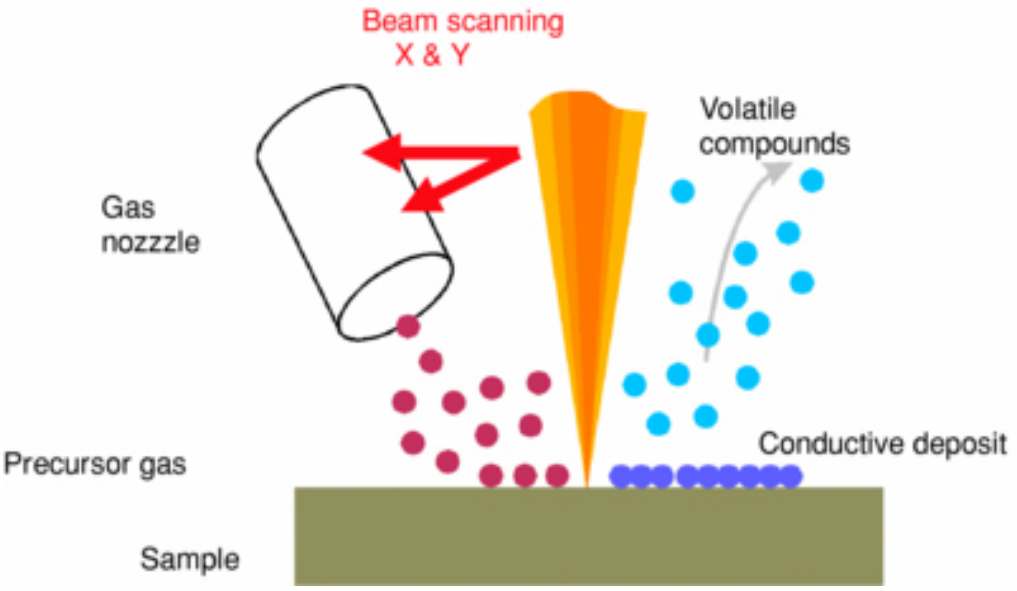

Figure 5.6: Schematic representation of GIS deposition of a conductive material [45].

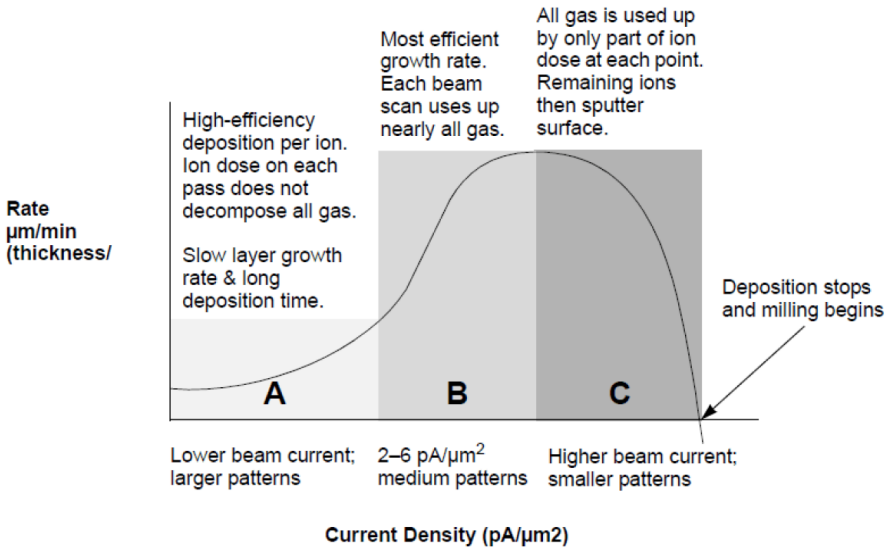

Figure 5.7: Deposition growth rate dependence on beam current [20].

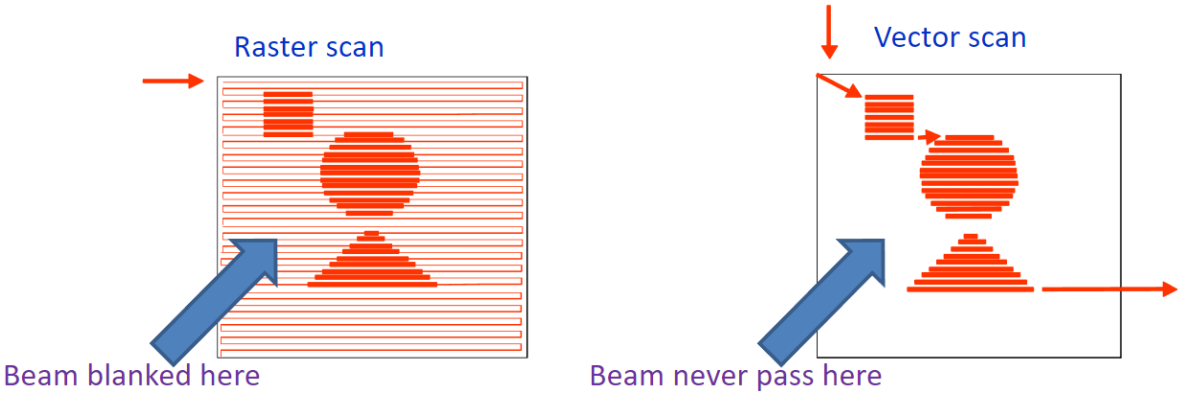

(a) Schematic representation of raster scanning patterning.

(b) Schematic representation of vector scanning patterning.

Figure 5.8

value of zero blanking the beam and any non-zero value unblanking the beam. The blue component determines the dwell time, with a zero value corresponding to a 100ns dwell time and 255 setting the dwell time to the maximum allowed by the software. Other parameters such as depth can be set in the user interface, bitmaps are typically used for patterning complex shapes or quickly patterning orientation and alignment markers.

The final option is to use a stream file, a stream file is a custom pattern file created in ASCII. The software's patterning field of view is divided into 4096 steps, 0-4095 in X and 280-3816 in Y. The advantage of using a stream file is the control of the sequence each pixel is milled in. The patterning tools and bitmap options are scanned in a raster method, where the beam scans the defined patterning area line by line, as seen in figure 5.8a [11]. However due to imperfect blanking of the beam between these defined areas, inter-hole milling can result from raster scanning [34]. To reduce this undesired result the sequence the beam scans over the sample can be changed, by using a stream file. For example if the geometry contains a circular cross section, sequencing the beam to scan in a spiral fashion can avoid inter-hole milling by passing only once between each milled circle. Similarly stream files can be used to minimize the time spent between structures to reduce unwanted milling as shown in figure 5.8b [39].

In this project all three options for patterning were utilised. The predefined patterning tools were used to take cross sections of the filter for the characterisation work described in Chapter 4. Bitmap files were used to pattern the larger structures produced in this project such as alignment markers and classical diffraction gratings. Finally stream files were chosen for patterning the quasicylindrical wave (QCW) gratings.

5.3 Sample characterisation and fabrication

Before the geometry was patterned onto the filter, more information about the sample was needed. The number of layers, the depth of each layer and the sputtering rates for the different materials can be found by performing a cross section procedure on an unused part of the filter. This consists of milling to several different depths in the filter, depositing a layer of protective material and sputtering away a cross section. A typical cross section consists of a box with 3 traditional sides with the fourth side milled away in a step like fashion, this allows the exposed layers of the filter to be seen when the stage is titled to 52º, a schematic of a typical cross section is shown in figure 5.9. Platinum was deposited using the gas injection system (GIS), as the protective material, it also provides the contrast to be able to observe the depth milled. Figure 5.10 shows a cross section through the dielectric layers and into the quartz substrate, using a trigonometric component of the observed length to account for the 52º tilt, the filter was determined to have an average thickness of 5.8μm and an average spluttering rate was obtained. The measurements of the thickness of each layer and the total number of layers was then used to improve the FDTD model of the filter.

5.3.1 Alignment Markers

Using the sputtering rates from characterizing the filter, circular apertures were milled through the dielectric layers at various points on the sample. The primary purpose of this was to make it possible to navigate around the filter to find the QCW gratings once it was in the measurement system, the apertures were also used to help with focusing onto the sample and to obtain the size of the beam incident on the sample. Circular apertures of radius 100μm, 30μm, 10μm and 3μm were patterned around each QCW grating, forming the vertices of a diamond of height and width 2mm, with the QCW grating at the centre, as shown in figure 5.11. Keeping the order of 100μm north, 30μm west, 10μm south and 3μm east for each grating allows these markers to be used to obtain the orientation of the sample, which is important when looking at polarization.

5.3.2 Classical Gratings

Classical diffraction gratings with periods of 12μm, 6μm and 3μm were patterned onto the filter, as shown in figure 5.12. Each grating has 10 periods and each period has a height of 50μm The classical diffraction gratings were used to verify that the far field image detected by the measurement system is correct by observing the classical diffraction orders.

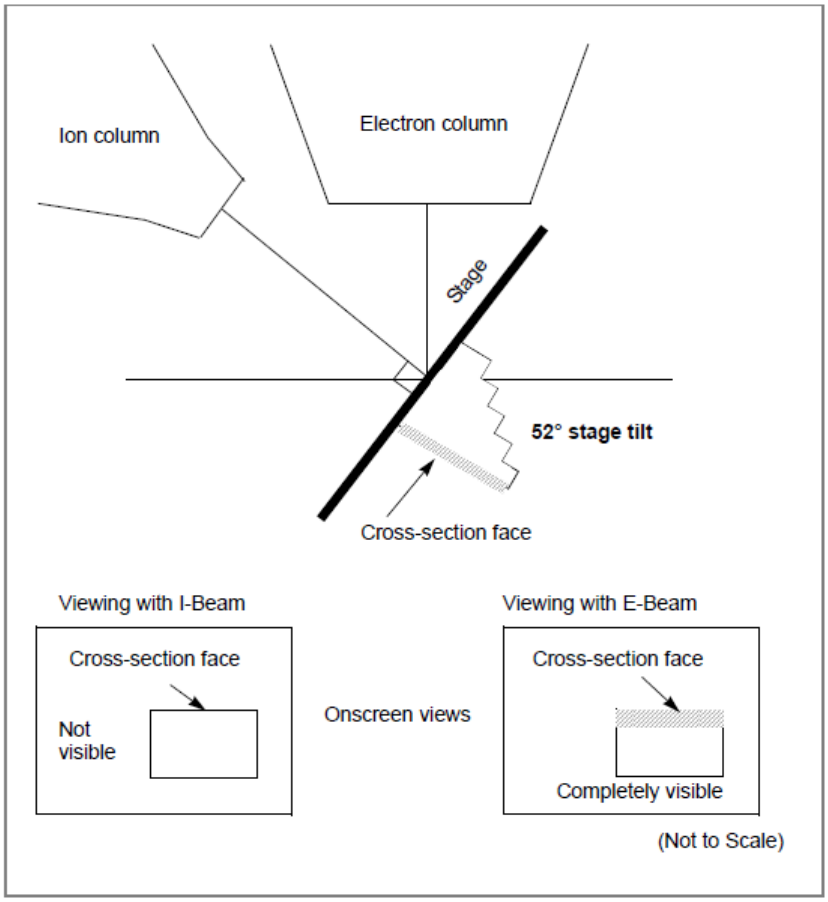

Figure 5.9: Cross section viewing during milling [20].

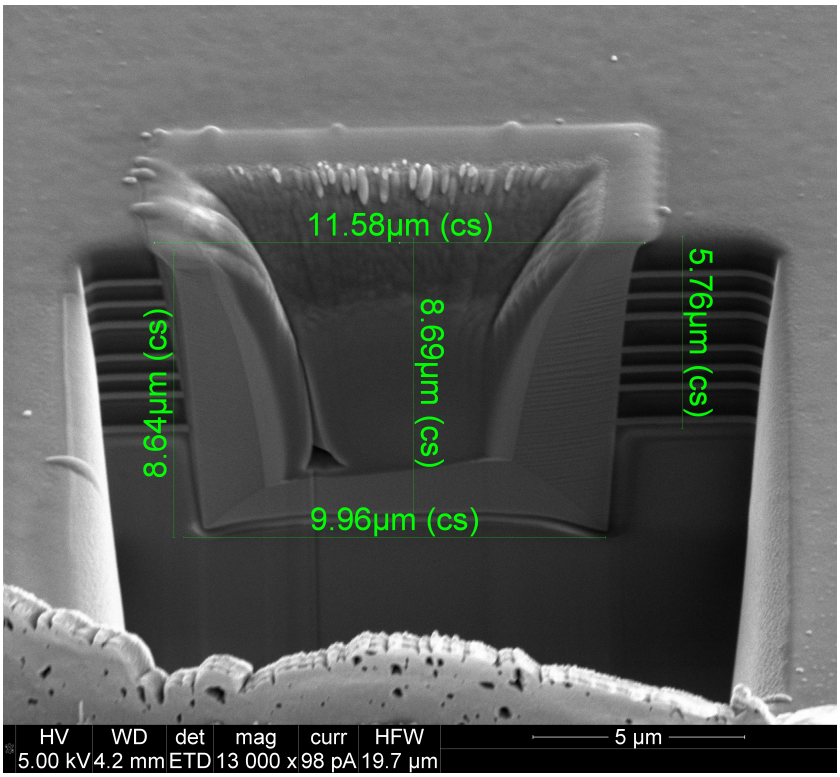

Figure 5.10: A cross section through the band pass filter's dielectric layers.

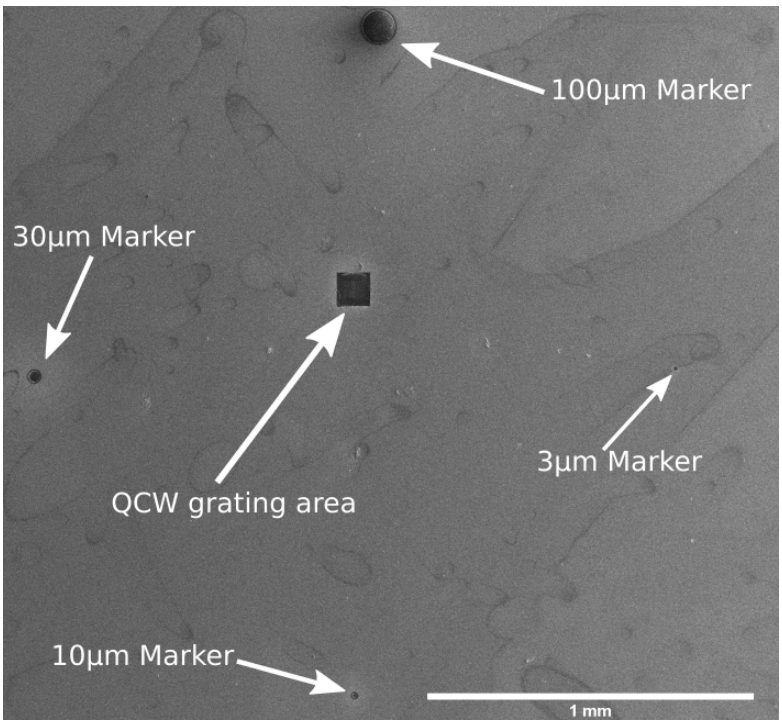

Figure 5.11: SEM image of alignment markers with QCW grating in the centre.

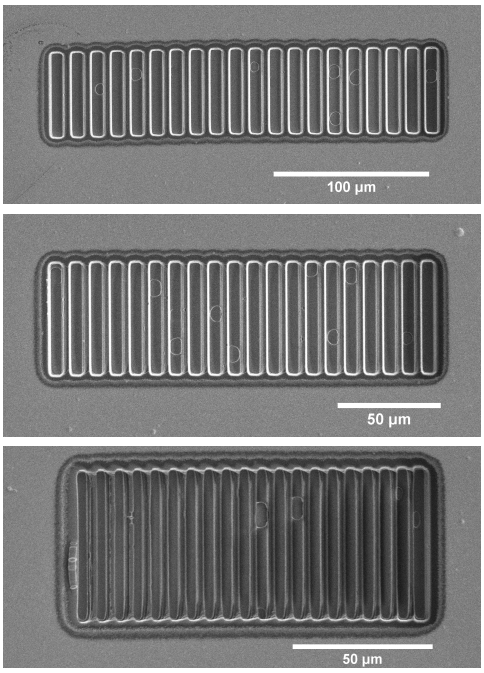

Figure 5.12: SEM image of completed classical gratings, 12µm (top), 9µm (middle), 6µm (bottom).

5.3.3 QCW gratings

An initial coarse etch was performed at a beam current of 7nA, to sputter away an 100µm^2 area of Au and PMMA to create a site free from conducting material to pattern a QCW grating. All etches were performed at a constant accelerating voltage of 30keV. The 1D QCW grating geometry modeled in Chapter 4 was etched using a beam current of 1nA to keep the etching time down in order to minimize beam drift. A large dwell time (~1ms) was used to reduce the angle of the sidewalls of the slots and aperture as shown by Hopman et al [35]. Figure 5.13 shows a SEM image of a 3.2µm QCW grating. In total three optimized geometries for resonances centered around 3.2µm , 3.4µm and 3.6µm were patterned onto the filter, with repeats of each grating etched in case of laser induced filter damage.

5.3.4 Sample Map

The patterning of alignment markers, classical and QCW gratings were completed and a map of where each feature was positioned on the sample was created to help with navigation and identifying the features once the sample was placed in the measurement system. A sample map is shown in Figure 5.14, note the sample will be placed in the measurement system so that the light will be incident onto the substrate, this means that a mirror of the sample map

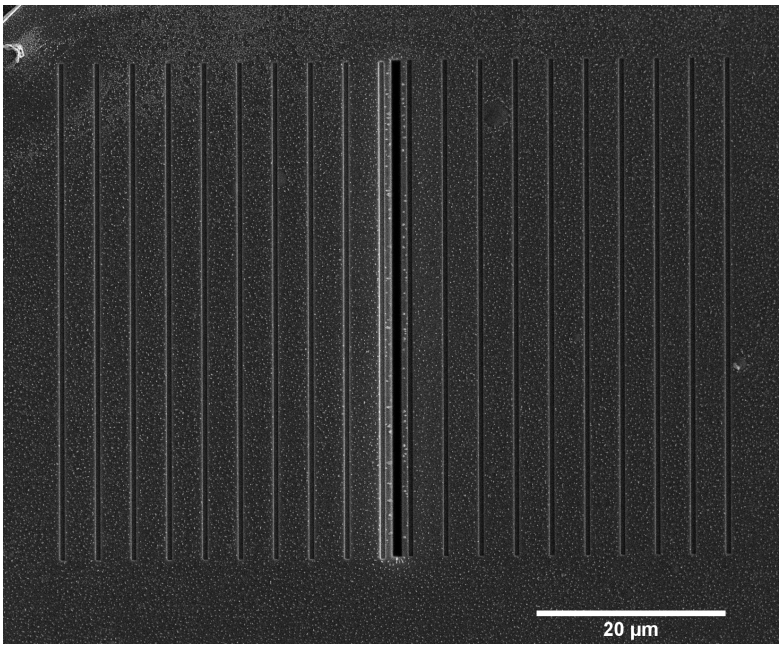

Figure 5.13: SEM image of a completed QCW grating.

will be seen by the system.

5.3.5 Lift off process

With the patterning stage completed the conducting layer needed to be removed to leave a fully dielectric sample. A lift-off process was performed to remove the unwanted gold layer, by using a solvent to dissolve the photo-resist. The PMMA layer was dissolved in acetone, warmed to 50ºC and an ultrasonicator was used to aid the process. The filter after fabrication was completed, under a light microscope is shown in figure 5.15.

5.4 Optical Measurement

5.4.1 Setup Overview

Optical measurements presented in this work were performed using an IR laser set up. Light emitted from a tuneable nanoLavente OPO in the wavelength range 1.4-4.2µm is focused to a spot size of ~2λ on the sample by a x36 reflecting objective (numerical aperture (NA) 0.5). The light transmitted by the sample, which is mounted on a motorized xyz stage, is collected by a x15 reflecting objective (NA 0.3) that directs collimated light onto a focusing parabolic mirror which in-turn focuses the light into a single element detector. As the light is scattered

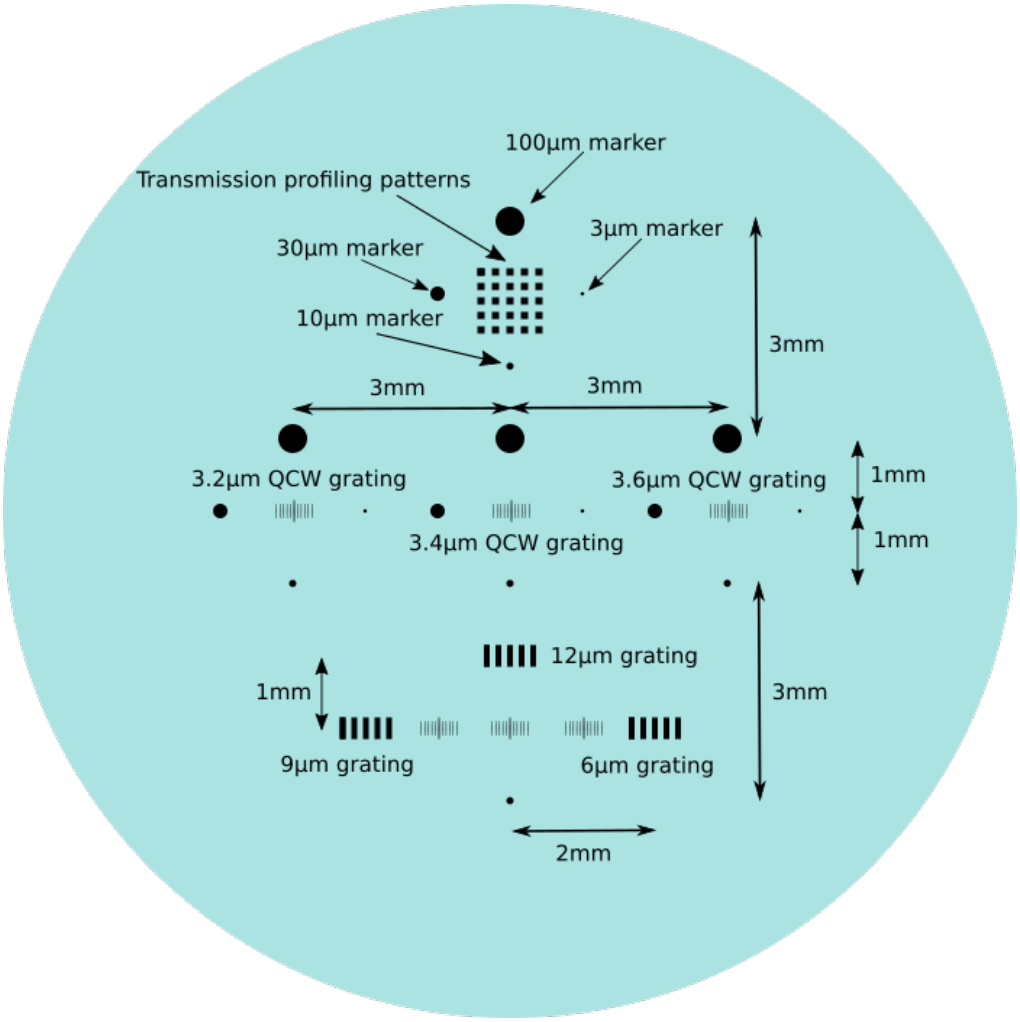

Figure 5.14: Sample map, showing the layout of key gratings and alignment makers.

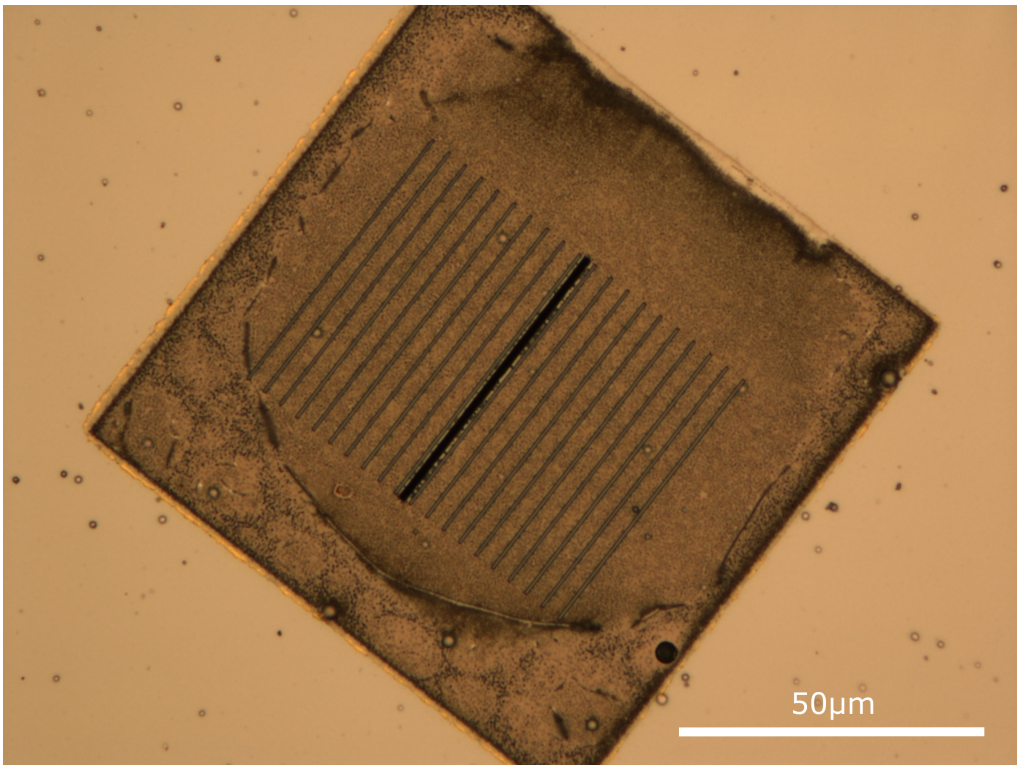

Figure 5.15: Light microscope of filter post lift-off.

by the sample at different angles, the collection optics and detector are also mounted on a motorized xyz stage to collect the full far-field radiation pattern. Reflective objectives were chosen over refractive ones to minimize chromatic aberrations that result from the changes in wavelength. The motorized xyz stages are driven by DC Servo Motor Actuators which allow precise repeatable positioning down to 800nm. A schematic of this set up is shown in figure 5.16.

5.4.2 NanoLevante OPO

The light source used was a A.P.E nanoLevante which is an optical parametric oscillator(OPO). The nanoLevante is pumped at a variable repetition rate at 1064nm wavelength by a diode-pumped, passively Q-switched solid state laser. This input laser provides two horizontally polarized output waves, Signal and Idler, out of two separate ports. The Signal output has a tuning range from 1470nm to 1950nm and the Idler has a tuning range from 2300nm to 4200nm, the output power over these ranges can be seen in Figure 5.17. The wavelength tuning is achieved by moving an optical element with a factory calibrated stepper motor, with a minimum step size corresponding to 1nm wavelength resolution. The repetition rate can be changed from single shot up to 20kHz by using internal and external triggers with pulse dura-

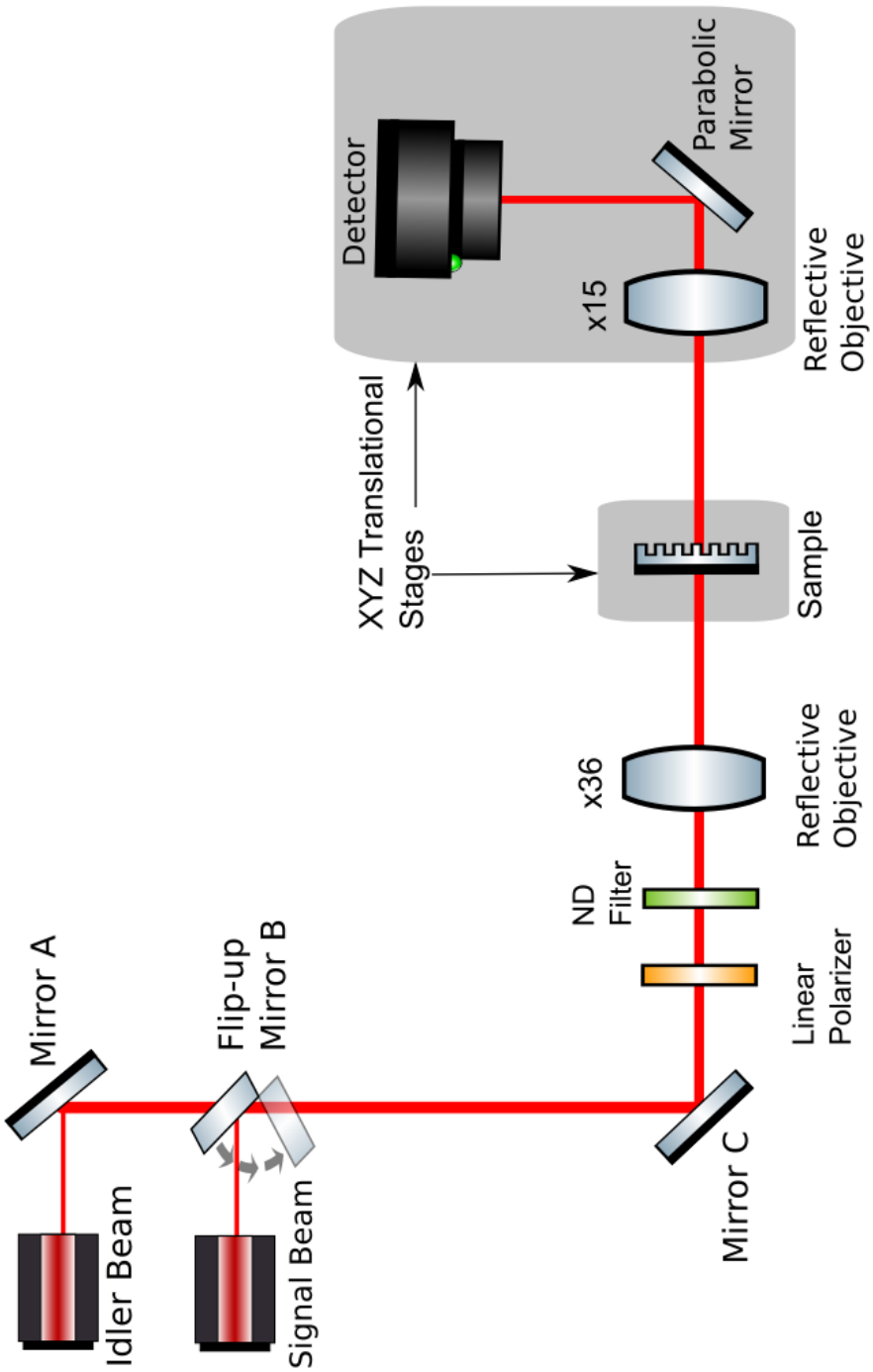

Figure 5.16: Schematic representation of optical measurement system.

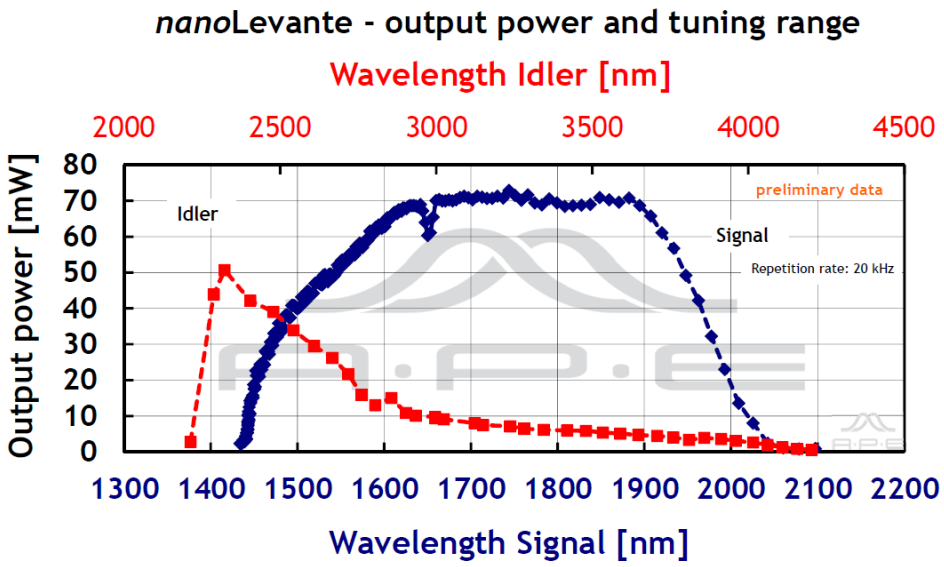

Figure 5.17: Optical response of nanoLevante's Idler (red) and signal (blue) beams.

tion of under two nanoseconds. The nanoLevante is fully automated and the OPO operation is controlled via USB by the lab computer. By removing the optical filters (servo controlled) the 1064nm pump laser and its green second harmonic light at 532nm can be used as a pilot beam for optical alignment. An overview of OPO systems is given in section 2.

5.4.3 Far-field Detection

The IR detector was a VIGO System PVI-3TE, which was thermo-electrically cooled to 203K. The detector was an optically immersed photovoltaic with a barium fluoride (BaF_2) window, connected to a DC coupled transimpedance preamplifier with a gain of $2.1e^4$ and a cut of frequency of 10MHz. The detector had an active area of $1x1mm^2$ and was responsive over a wavelength range of 2.1-4.2μm, optimized at 4μm with a response of 2.0A/W as shown in Figure 5.18.

5.5 Measurements

Initial characterization measurements were performed on the sample to validate the measurement system and ensure the filter was not damaged during the fabrication process.

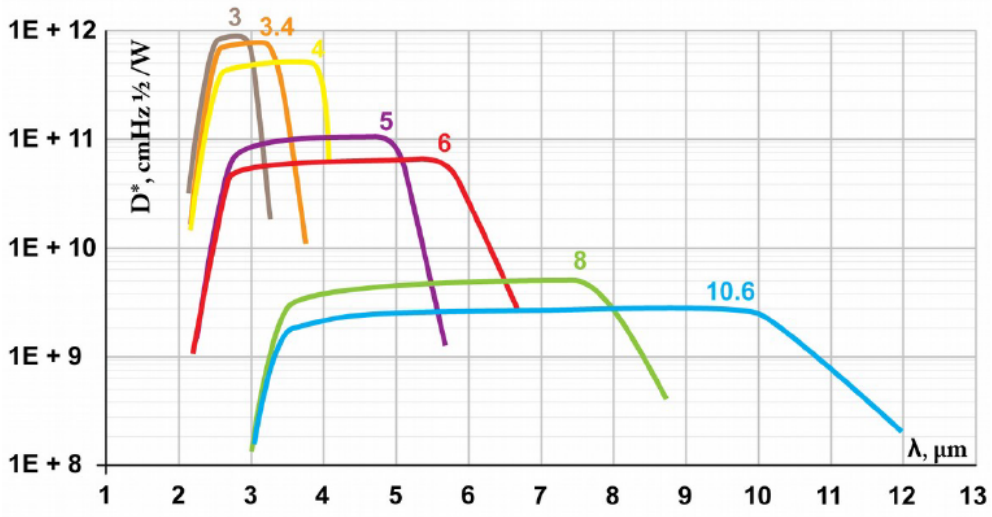

Figure 5.18: Wavelength response of VIGO IR detectors, the yellow line is the PVI-3TE used on the measurement system.

5.5.1 Imaging Sample

Optical Alignment

Two visible green pilot beams, with a wavelength of 532nm, exiting from the separate Signal and Idler ports and a series of pinholes were used to align the optical system. Firstly the two pilot beams were directed onto the same area of mirror C by adjusting mirror A and flip up mirror B. Next the pilot beams were directed through the centre of the x36 reflecting objective, pinholes were placed at the entrance to the optical cage and on the reflecting objective to ensure both ports had the same beam path. The collection optics motorized stage was moved to centre the beam onto the x15 reflecting objective. Pinholes were placed on the x15 reflecting objective and in front of the parabolic mirror and adjustments made to the stage such that the beam passed through both pinholes, this ensured the stage is horizontally level. Finally a pinhole was placed in front of the detector and the parabolic mirror was adjusted to centre the beam to maximize the throughput to the detector. The pilot beam was switched off and the Signal and Idler beams turned on, with 0.01% transmission ND filters, the response of the detector was tested. It was found the pilot beams had a slightly different path to the Signal and Idler beams, to view the position of the beams an IR detector card was used to make additional adjustments to the system. The IR detector card reacts to wavelengths from 1.5µm to 13.2µm, a layer of thermochromic liquid crystals change colour when IR light changes the temperature of the card as seen in Figure 5.19a. The IR targets, shown in Figure 5.19b, replaced the pinholes and the same methodology as with the pilot beams was followed. With the optical system aligned the sample was placed on an xyz motorized stage, with the substrate closest to

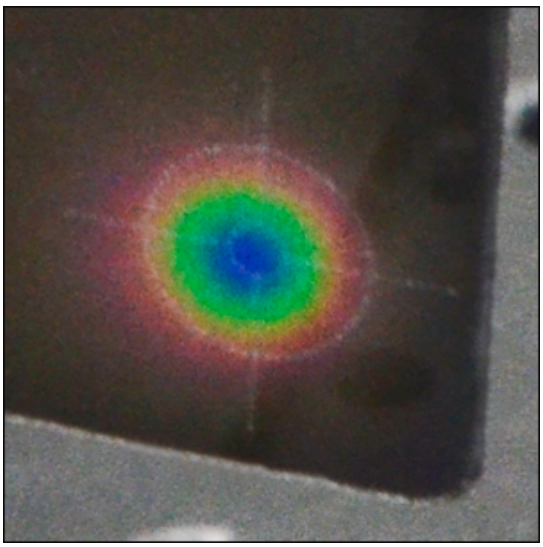

(a) Detector card changing colour when exposed to IR light.

(b) Cage system Alignment plate with Mid-IR Disk.

Figure 5.19

the OPO.

Alignment Markers

For all of the following measurements Mirror B was lowered and the nanoLevante's Idler beam was used, with a repetition rate of 15kHz and a pulse duration of ~2ns. The Idler beam was adjusted to a wavelength of 2910nm, corresponding to the bandpass of the sample. With high transmission of the beam through the sample, ND filters were placed in the beam path, reducing the beam to 0.01% of its source power to prevent the detector from saturating. The detector was moved in the x,y and z directions to find the position at which the beam intensity was at maximum. The wavelength was then adjusted to 2600nm and the sample was moved in the x and y directions to create an initial sample map, as shown in Figure 5.20. Here, high signal is obtained when the beam is incident upon an alignment marker or diffraction grating. The sample was then moved along the z direction to bring the features into focus, with the 100μm, 30μm and classical diffraction gratings visible the sample was rotated to optimize the gratings for horizontally polarized light.

Beam size

The sample was then moved to a set of 100μm, 30μm and 10μm alignment markers, the z position of the sample was adjusted while keeping the sample to detector distance constant

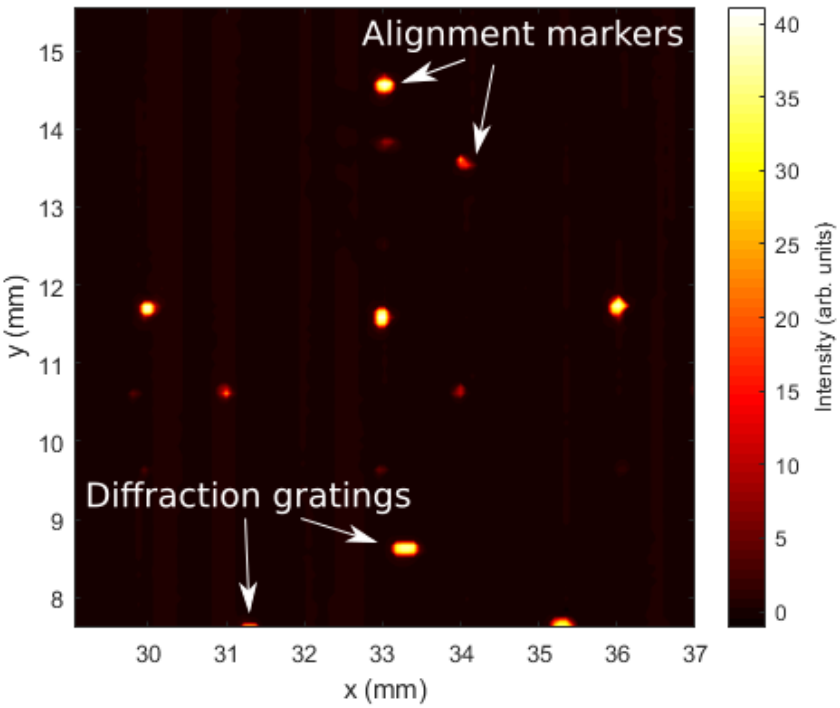

Figure 5.20: Initial map of sample when scanned by incident beam. Source wavelength 2.6μm.

until the markers were brought into focus. With the beam incident on the 10μm marker, the detector position was fixed and the sample was moved in the x and y direction to create an image of the 10μm marker. Doing so effectively images the beam, using 10μm stencils, allowing for the size of the beam to be measured. The scan of the 10μm marker was repeated for multiple wavelengths and the beam size was measured to be ~2λ.

5.6 Conclusion

In summary, a mid IR dielectric band pass filter was patterned using a focus ion beam. The fabrication method for creation of a fully dielectric 1D QCW grating was outlined and fabrication results were presented. The measurement system was introduced and validated ready for characterization of far field radiation resulting from QCW coupling.

Chapter 6

Optical Measurements

6.1 Introduction

This chapter presents optical measurements performed on the patterned fully dielectric mid infrared band pass filter which was designed and modelled in Chapter 4 and fabricated as described in Chapter 5. Analysis is performed on the far field radiation pattern produced by the geometries designed in this thesis and flaws in the filter are highlighted. Solutions to these problems are then presented and implemented on a second mid infrared band pass filter described at the end of this chapter.

6.2 System Validation

6.2.1 Filter transmission

Upon receiving the dielectric band pass filter from Northumbria Optical Coatings Limited (NOC), the filter was placed in the infrared optical measurement system described in Chapter 5, a schematical representation is shown in Figure 6.1.

Both reflective objectives were removed and ND filters of strength 1.0 and 2.0 were placed in series between the output of the OPO laser and the sample in order to avoid saturating the detector, this reduced light incident upon the detector to 0.1% of maximum power. The resulting larger spot size upon the filter also allowed for faster characterization of the entire sample's surface. The OPO laser's wavelength was matched to the midpoint of the filter's band pass, allowing for maximum transmission through. The detector was then centered onto the radiation exiting the filter, note that due to the low divergence of the incoming radiation, the detector's distance from the sample (z direction) was not changed. The transmission between

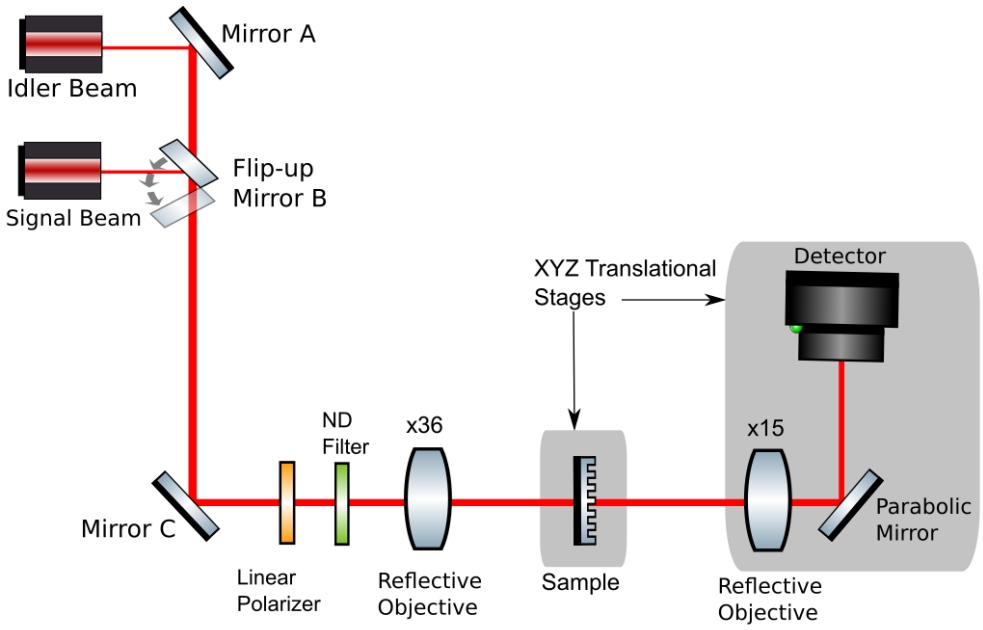

Figure 6.1: A schematic representation of optical measurement system

1.5-1.95μm (signal beam) and 2.3-4.2μm (idler beam) was measured, in 200nm steps. For each step the sample was translated in the x and y directions to allow the laser to scan the entire surface and an average transmission value was recorded. The geometry described in Chapter 4 was then applied to the filter, using the method outlined in Chapter 5. Once the fabrication steps were complete the filter was returned to the optical measurement system for characterization. Prior to confirming that the optical system was collecting the far field radiation patterns as expected, another set of transmission measurements were performed on the filter to ensure that the fabrication process had not damaged it. The pre and post fabrication transmissions measurements are shown in Figure 6.2, no significant difference between the transmission scans could be seen and it was concluded no damage had been caused to the filter by the fabrication method.

6.2.2 Sample Scans

With the filter's transmission characterized pre and post fabrication, the next step was to identify the sample's orientation. First the reflecting objectives were placed back into the optical system and the detector realigned by translating it in the x-y planes until maximum signal was found. The laser's wavelength was moved away from the filter's bandpass, to 2.6μm. This ensures the filter blocks incoming radiation from the laser and any signal measured by

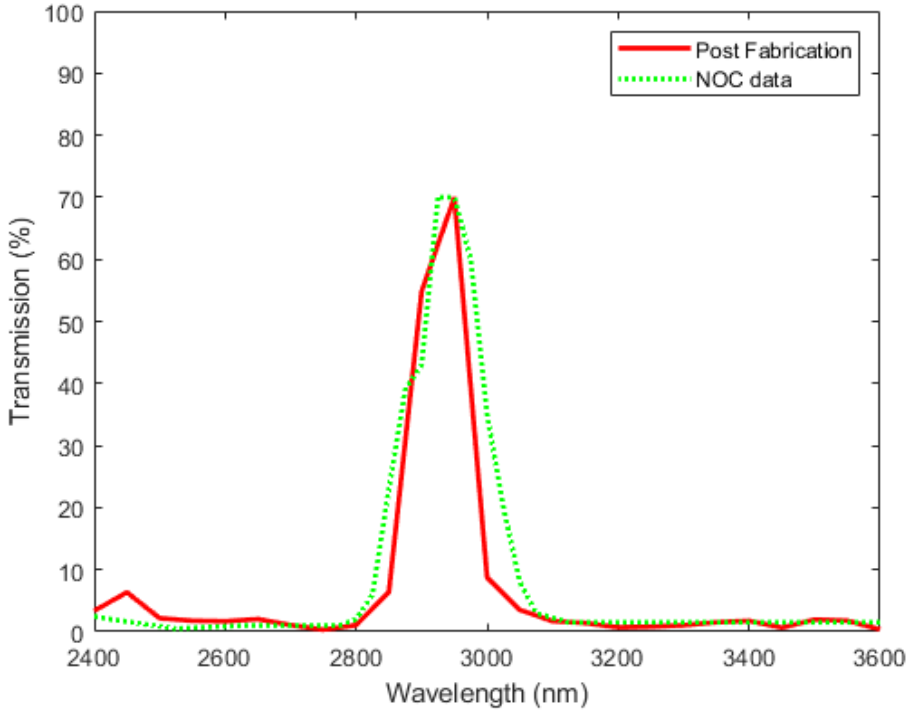

Figure 6.2: Transmission profile post fabrication (red) compared against manufacturer supplied spectra (green)

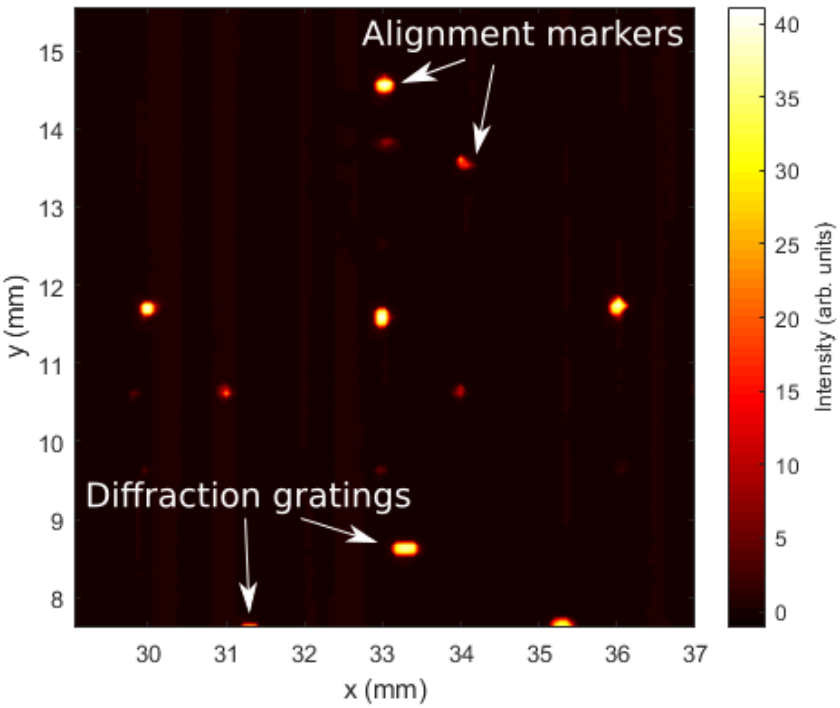

Figure 6.3: Sample map post rotation. Source wavelength 2.6μm.

the detector would be from radiation passing through the patterned areas of the filter. Coarse sample scans were carried out to locate the largest artifacts such as the 100μm optical markers and diffraction gratings created in the fabrication process. An initial coarse scan of the whole sample was carried out, here the detector's position was fixed and the sample was moved in the x-y plane in a raster pattern until the entire sample had been imaged. The step size was 100μm, which is small to ensure at least 1 point of signal at each of the large artifacts. The positions of the 100μm markers and diffraction gratings were compared with the FIB images to identify the sample's orientation. The sample was found to be rotated by 37º. The sample's mount was then rotated to correct the orientation difference, this is important as the incident radiation should be TM polarised with respect to the 1D nanogratings to achieve the described beam shaping. With the orientation corrected, the coarse scan of the sample was repeated to confirm the desired rotation has been reached and obtain an initial sample map which is shown in Figure 6.3.

The next step was to move the sample onto the focal point of the first reflective objective, to minimize the spot size incident upon it. The sample was moved in the x and y planes until the laser was incident upon an 100μm marker. Coarse x-y sample scans were carried out, with a total area of 200μm² and a step size of 20μm, these scans were repeated at various positions

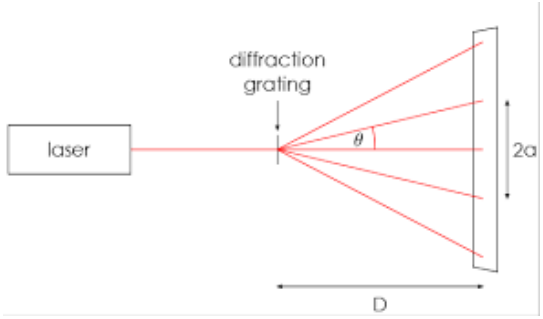

(a) Diffraction orders produced by monochromatic light incident upon a grating

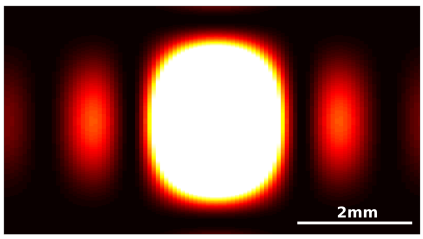

(b) Simulated far field pattern of of 2.6μm light incident upon a 12μm grating

Figure 6.4

of the sample along the z axis, to find a coarse focal point. With a smaller and more energetic spot size, the incident radiation was moved onto the 30μm marker. The focusing process was repeated for the 30 and 10μm markers to minimize the spot size, using the 10μm marker as a stencil, the spot size was estimated to be ~2λ.

6.2.3 Far-field measurements

With the filter occupying the focal point from the first reflecting objective, the correct distance between the exit surface of the filter and the second reflecting objective was investigated. The aim here was to collect and collimate light scattered by the filter onto the detector and thus characterize the far field. Classical diffraction gratings provide a known far field on which to have a baseline to start from. Monochromatic light incident upon a grating will constructively and destructively interfere with itself, producing an interference pattern of well defined maxima (bright spots) called grating orders, shown in Figure 6.4a. The classical interference pattern is well understood; intensity, form and distances can be compared directly with theory to ensure a true far field is collected by the detector. Figure 6.4b shows the far field pattern of 2.6μm light incident upon a 12μm grating, simulated in MATLAB, here you can see the bright zeroth order (m=0) in the centre, with less intense first order (m=1) fringes either side.

The laser was focused onto the large diffraction gratings. Starting with the 12μm classical grating, the sample scan is shown in Figure 6.5 and the corresponding far fields are shown in Figure 6.6. In the sample scan, maxima in intensity corresponds to the slots in the filter machined by the FIB. The far field diffraction pattern consists of three fringes, at an incident wavelength of 2.6μm,the spacing between the zeroth and first order was measured to be 2.1mm, compared to a calculated value of 2.3mm. The calculated value was obtained using the equation $d \sin \theta_m = m\lambda$, where d is the slit separation distance, θ_m is the angle between

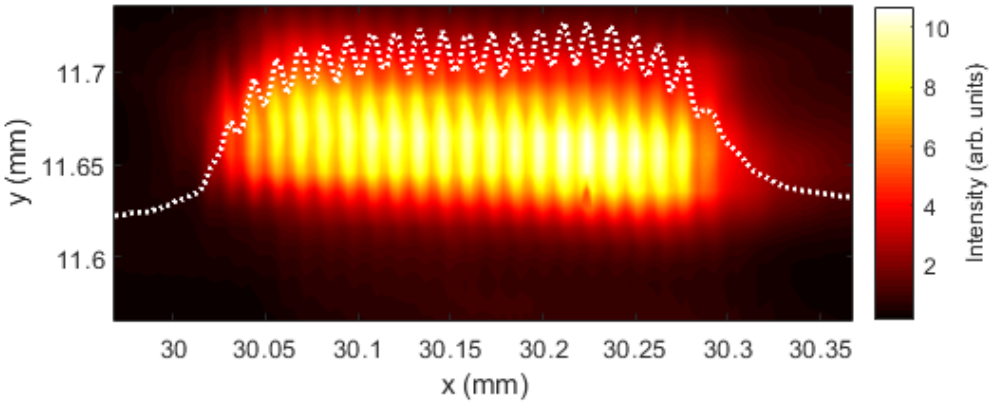

Figure 6.5: Classical grating sample xy scan. Source wavelength 2.6μm.

the diffracted ray and the grating's normal vector and λ is the wavelength of the incident light. These measurements show both that the laser can be focused to a spot size on the order of the slot width (800nm), and that the measurement system gives a valid far field pattern.

6.3 QCW resonant nanograting

6.3.1 Far field measurements

Once a correct distance between the exit surface of the filter and second reflecting objective had been found the search for the QCW nanogratings could begin. This was done by first finding the 100, 30 and 10μm alignment markers for each of the nanogratings and using them to triangulate it's position. An area of 100μm by 100μm square was then scanned by moving the sample in the x,y plane and keeping the detector's position fixed. A step size of 800nm in the y direction and 5μm in the x direction was used to ensure multiple points of the incident beam upon the subwavelength aperture, note the smallest repeatable step size for the DC Servo Motor Actuators that drive the motorized xyz stages is 800nm. The incident light's wavelength was set to 2600nm, this is the smallest wavelength for which the transmission through the sample will be negligible. Figure 6.7 shows the raster sample scan for the 3.2μm resonant nanograting. This demonstrates that light is only transmitted through the sample where the nanogratings had been patterned.

With the light incident on the subwavelength aperture of the 3.2μm resonant nanograting, the sample's position was fixed and the detector was moved in the xy plane to collect the far field radiation pattern created by the nanograting. Figure 6.8 shows the far field radiation pattern at wavelengths from 3200nm to 3350nm, the far field pattern appears to be a uniform

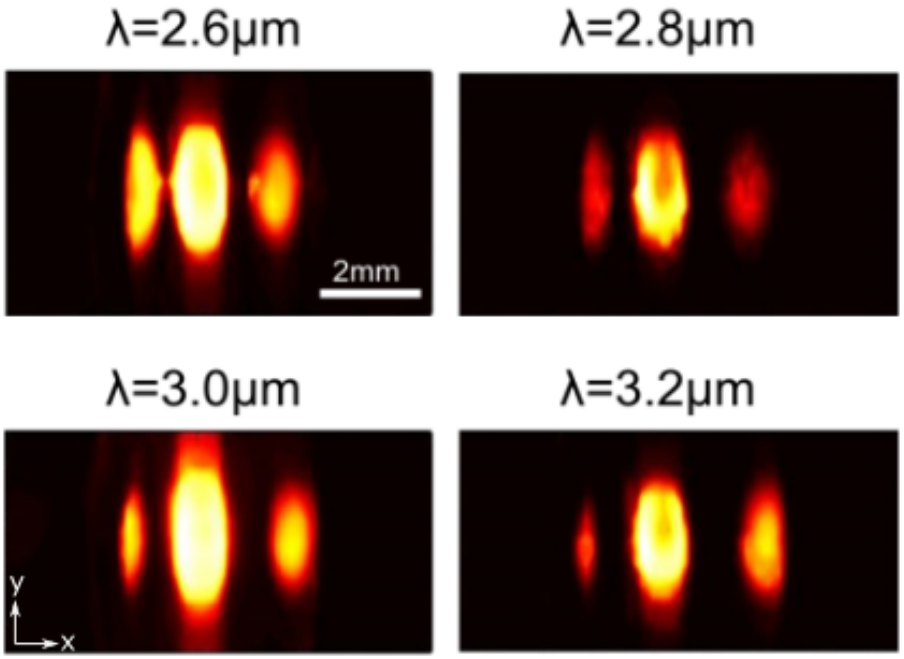

Figure 6.6: Classical grating detector xy scans at various wavelengths

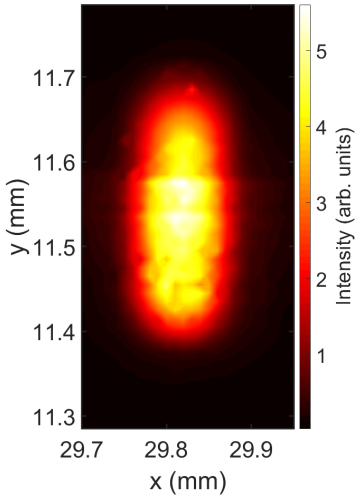

Figure 6.7: 3.2μm QCW grating sample xy scan. Source wavelength 3.2μm.

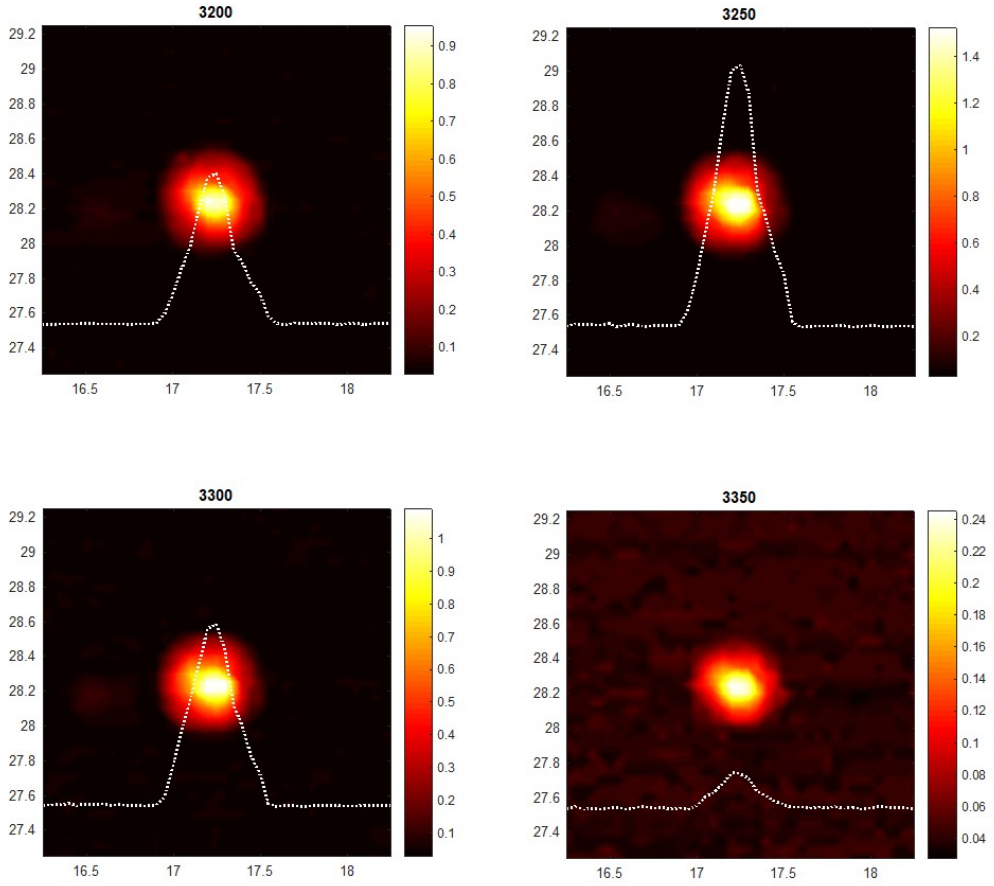

Figure 6.8: 3.2μm QCW grating detector xy scans at various wavelengths

and focused beam, across all wavelengths. Given that the light should have passed through a subwavelength aperture and the sensitivity of QCWs gratings outlined in earlier Chapters, a radiation pattern with divergence in the x-direction was expected, with a greatly reduced divergence occurring at resonance (3.2μm).

The wavelength range was increased to investigate far field patterns further away from resonance, a wavelength sweep from 2400nm to 3600nm was performed and analysis on the far field measurements was carried out, this will be presented in more detail below. The laser was moved onto the 3.4μm grating following the same method of using the alignment markers to triangulate its position as done for the 3.2μm resonant nanograting, again the sample was moved to ensure the laser was incident upon the subwavelength aperture and the far field radiation pattern was collected for a range of wavelengths. The resulting far field patterns can be seen in Figure 6.9. The far field is the beam at resonance, it can be seen that the beam is marginally larger in the x direction than the y direction hinting that the beam may be the result of a highly divergent beam that has been focused by resonant nanogratings however off

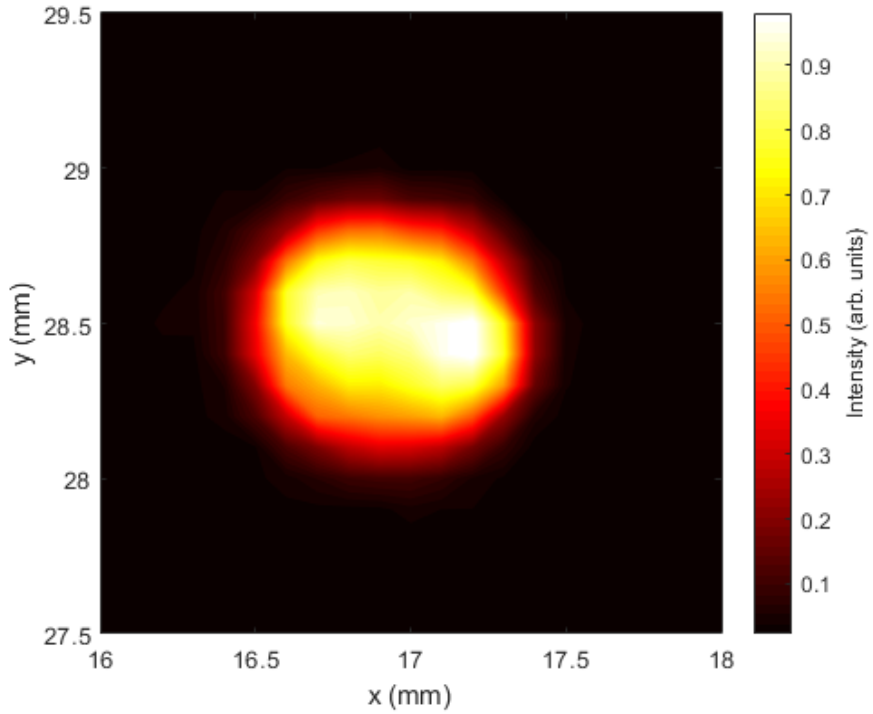

Figure 6.9: 3.4μm QCW grating detector xy scan. Source wavelength 3.4μm.

resonance the beam was no more divergent and the trend was similar to the 3.2μm resonant nanograting.

6.3.2 FWHM analysis

The far field measurements were more closely analysed to determine if there was any wavelength dependence, Figure 6.10 shows a comparison of the full-width half maximum of the far field radiation pattern for the 3.2μm and 3.4μm resonant nanogratings, here the FWHM should be lowest at the resonance wavelengths for each grating however it is clear from the data that is this not the case. The smallest FWHM is seen at a wavelength of 2600nm for the 3.4μm resonant nanograting and 3400 for the 3.2μm grating. The FWHM peaks for both gratings at 3000nm. The variance in the FWHM is small across the whole range and away from the bandpass is largely invariant with wavelength. The increase in FWHM around 3000nm is likely due to the bandpass of the filter allowing a large portion of incident light to pass directly through the filter and could illustrate the incident beam size as seen by the detector. Figure 6.10 suggests that light passing through the grating is less divergent than light that passes through at bandpass. However this is difficult to explain simply with surface waves as there would be a strong correlation between wavelength and FWHM, as presented in Chapter 4. One possible

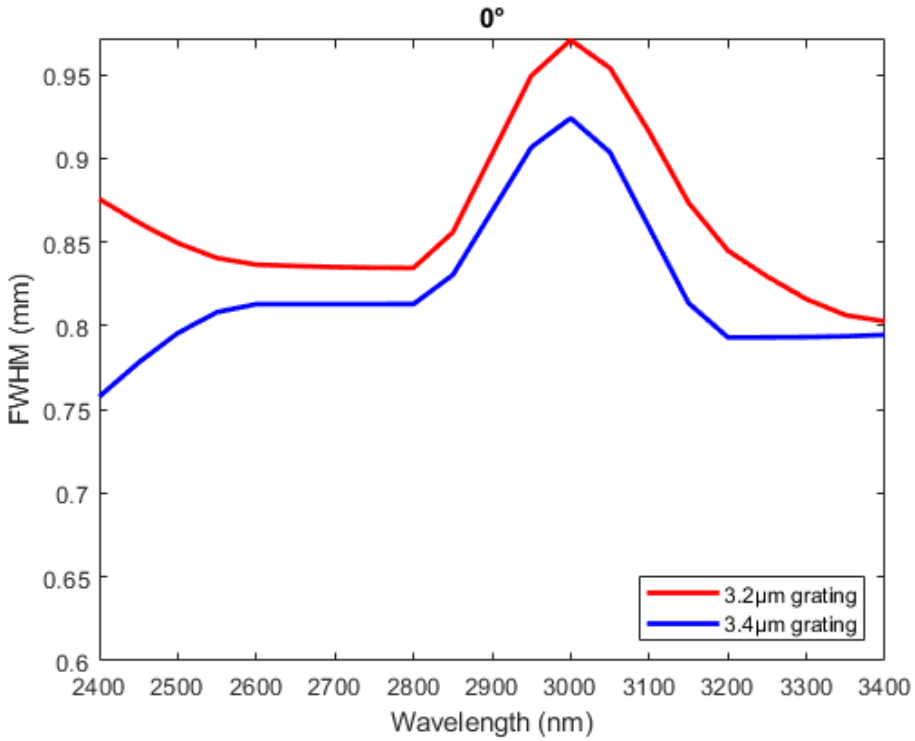

Figure 6.10: FWHM of measured far field intensity comparing the 3.2µm and 3.4µm gratings at a sample rotation angle of 0º

explanation could be that the beam is partially blocked by the filter away from the bandpass, This does not support the simulation results and appears to show no beam shaping behavior.

In the simulations (Chapter 4), the incident light was transverse magnetically (TM) polarised to achieve the reduction in divergence of the far field radiation at resonance. Although the OPO laser's manual stated the light emitted was TM polarised, this was checked to rule out the polarization being the cause of the lack of wavelength dependence in the far field. The sample was rotated to 90º and the methodology of obtaining a sample map and using the alignment markers to find the resonant nanogratings was repeated. A series of far field measurements on the 3.2 and 3.4µm resonant nanogratings were carried out at wavelengths from 2400 to 3400nm in 100nm intervals. This was repeated for a sample angle of 45º for a better representation of the effect of incident light polarization angle on the far field radiation pattern. Figure 6.11 shows the full width half maximum of the far field for the 3.2µm resonant 1D QCW nanograting for sample angles of 0º, 45º and 90º. The FWHM is more variable with wavelength at polarization angles of 45º and 90º, as with the 0º data, there is an increase in FWHM at the band pass of the filter. At 90º the FWHM decreases significantly as wavelength increases beyond the band pass however this doesn't support a 3.2µm resonance as expected

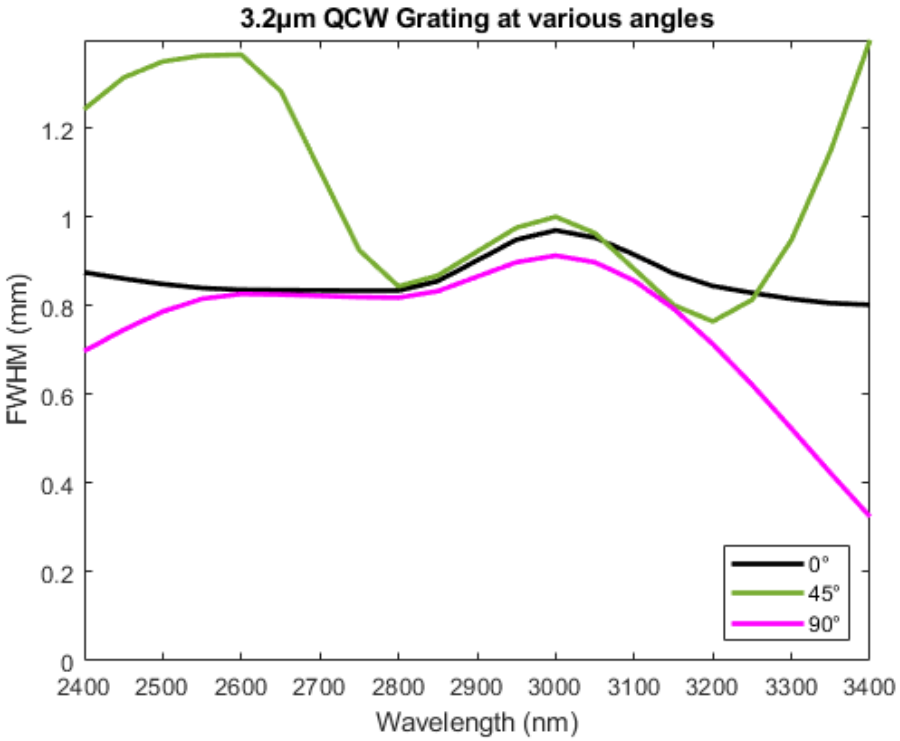

Figure 6.11: FWHM of measured far field intensity as a function of sample angle for the 3.2µm grating at various sample orientations

and may be the results of a less intensity incident beam as shown in Figure 5.17. 45° is more difficult to explain, sharp increases in FWHM are seen below 2800nm and above 3200nm.

Figure 6.12 shows the full width half maximum of the 3.4µm resonant 1D QCW nanograting, 45° compares well with 0°, the largest FWHM seen at the band pass. The 90° shows a peak FWHM at 3200nm followed by a sharp decline in beam width fund at 3400nm, unfortunately additional measures beyond 2400nm could not be obtained due to a large drop off in intensity of the OPO laser creating a far field with no measurable beam to calculate the FWHM for.

A further breakdown of FWHM data is shown in Figure 6.13. The trends for 0° have previously been discussed, 90° shows similar trends for both nanogratings with the smallest FWHM found at 3400nm, this would be expected for the 3.4µm resonant nanograting to support what is shown for in the theory. However, the peak at 3200nm is not reflected in the modelling and a supported argument for its existence cannot be made.

With no wavelength dependence found in the FWHM data, further analysis was carried out on the far field results for both nanogratings to try and gain insight into what is occurring at the

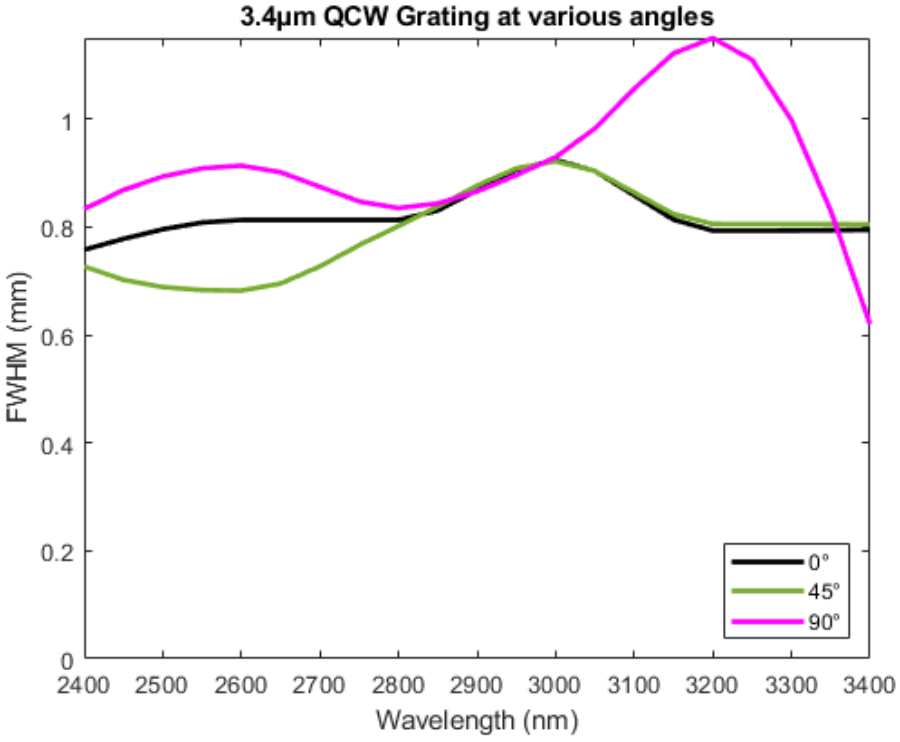

Figure 6.12: FWHM of measured far field intensity as a function of sample angle for the 3.4µm grating at various sample orientations

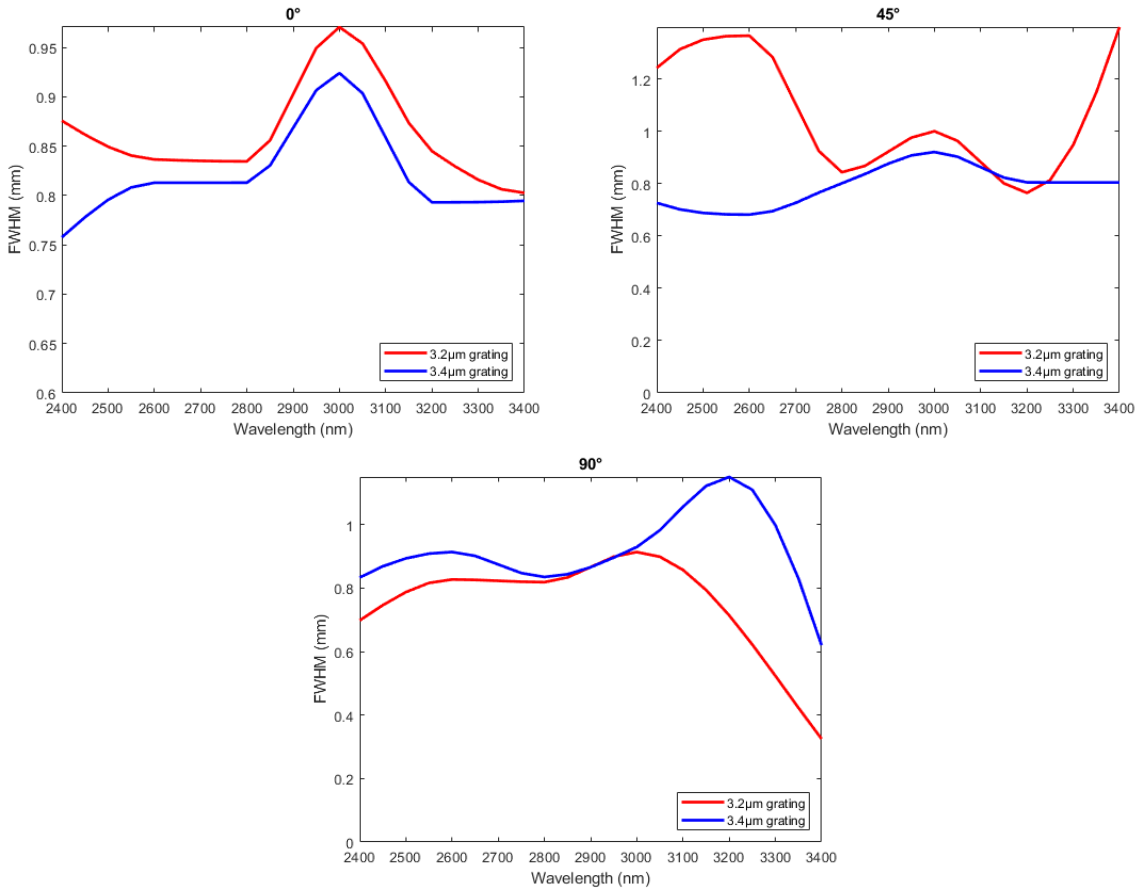

Figure 6.13: FWHM of measured far field intensity comparing the 3.2μm and 3.4μm gratings at various sample orientations

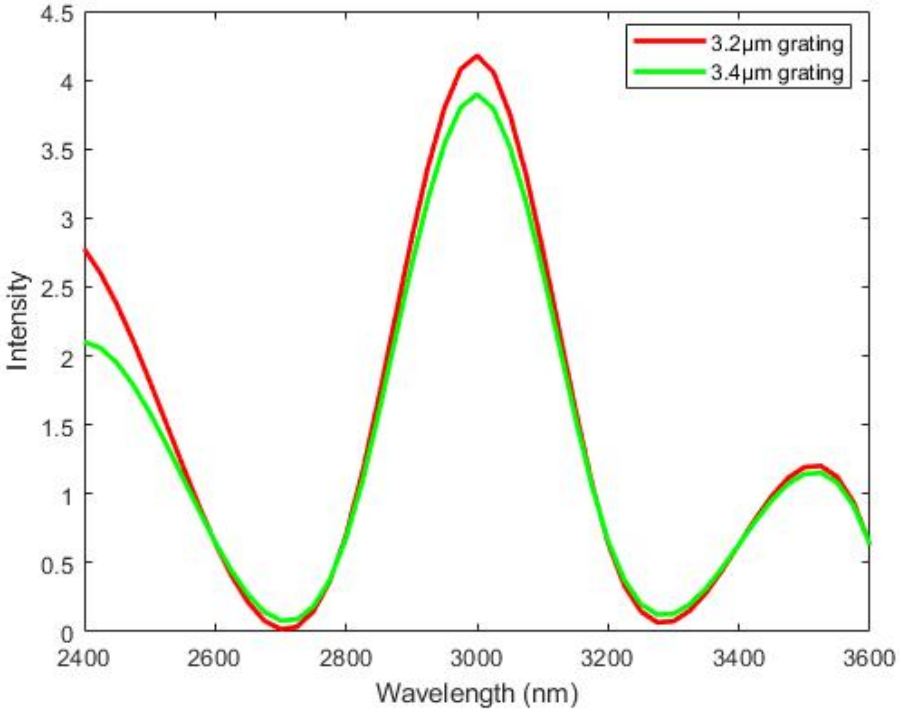

Figure 6.14: 3.2μm vs 3.4μm QCW grating beam intensity for a range of wavelengths

sample that results in no beam shaping occurring. Far field intensity data at 0º rotation for the 3.2 and 3.4μm gratings is presented in Figure 6.14 at a wavelength range of 2400 to 3600nm with a 100nm step size. The intensity shown is the average intensity inside the FWHM region of each far field pattern and is normalized for difference in the idler beam power shown in Chapter 5, Figure 5.17 and detector sensitivity displayed in Figure 5.18. The highest average intensity occurs at the band pass where the transmission through the filter peaks at 85%, the result is a relatively unchanged focused incident beam, the second highest peak occurs are 2400nm, this could suggest a non-negligible level of transmission through the filter occurring however is not a worry for investigating the role of QCWs in beam shaping as this is far from the resonant region for the nanogratings. The most significant peak is at 3500nm, this again could be transmission through the filter which if this is the case then would prevent the detection of beam shaping by QCWs, this is discussed in more detail later on in this chapter. The peak does not correlate to any changes in FWHM described above and occurs at the same wavelength for both the 3.2 and 3.4μm resonant nanogratings, which suggests it is not a result of interaction with the nanogratings.

The contribution of the subwavelength aperture to the far field radiation pattern can be investigated by rotating the sample at various angles and analyzing the intensity. The average

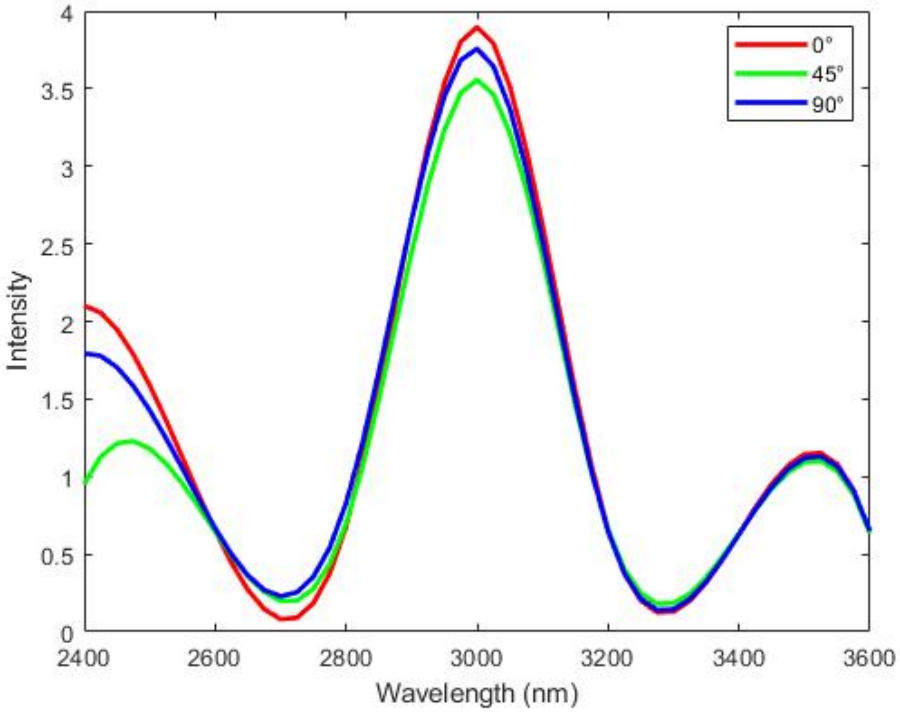

Figure 6.15: 3.4μm QCW grating beam intensity for a range of wavelengths at various angles

normalized far field intensity for the 3.4μm resonant grating at sample rotations of 0º, 45º and 90º is compared in Figure 6.15. It can be seen that the rotation has little effect on the average intensity which would suggest the subwavelength aperture is not the source of the far field radiation pattern and, given that the nanograting seems not to be contributing either, it is most likely the transmission wavelength response of the filter itself is largely responsible for the far field results seen.

For completeness, the average normalized far field intensity for the 3.2μm resonant grating at the 3 sample rotations is compared in Figure 6.16. Interestingly there is a more pronounced difference between the rotations than seen in the 3.4μm far field results, with the largest differences occurring at wavelengths shorter than the band pass. The 90º intensity being lowest is encouraging and would suggest the subwavelength aperture has a small contribution to the far field. However, no argument can be made for the 45º rotation having the highest intensity here and this is all occurring at a wavelengths far from the resonance wavelengths of the nanogratings.

With no clear change to the FWHM of the far field at resonance, the geometry was not performing as expected. The geometry simulated in Chapter 4 was successfully patterned on the filter within acceptable tolerances and additional optical microscope images were taken

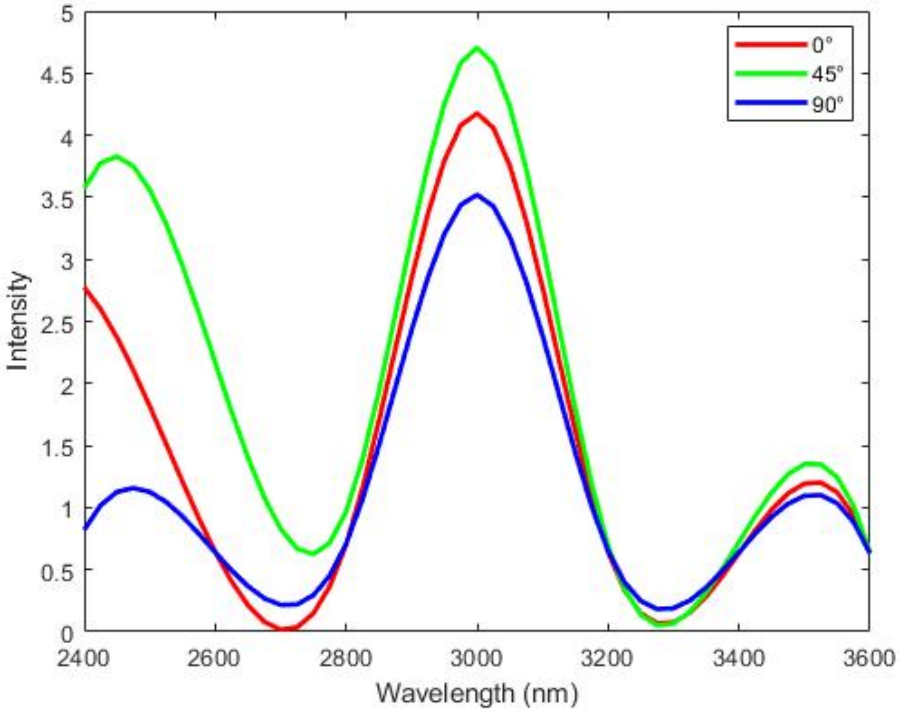

Figure 6.16: 3.2μm QCW grating beam intensity for a range of wavelengths at various angles

to verify that the geometry had not been damaged by the laser. The measurement system itself was verified to be working as expected by recreating classical diffraction patterns with the 12μm grating. Analyzing the mechanics of the nanograting, the non resonant nature of the results show that the grooves are not responsible for the far field pattern. The problem cannot be that the grooves are not re-radiating the surface waves created by the subwavelength aperture, as this would simply result in a highly divergent beam, which is not seen. This leaves the subwavelength aperture's role; off resonance the subwavelength aperture is the dominant contributor to the far field, it creates a highly divergent beam due to the scattering of the radiation escaping the aperture, as shown in Chapter 4, Figure 4.9. However this is not seen in the optical measurements, meaning radiation was not scattered at the exit of the subwavelength aperture. The null result was recreated in Lumerical FDTD by allowing radiation to leak through the sidewalls of the subwavelength aperture, this result can be seen in Chapter 4, Figure 4.7. This results in a less divergent beam, as the field is not scattered by the exit of the subwavelength aperture, the field simply radiates through the area around the subwavelength aperture corresponding to ~3 times the thickness of the filter, this not only prevents the aperture from channeling the fields but generates negligible surface waves for the grooves to scatter and re radiate. It was concluded this was the most likely cause of the optical results for 3.2 and

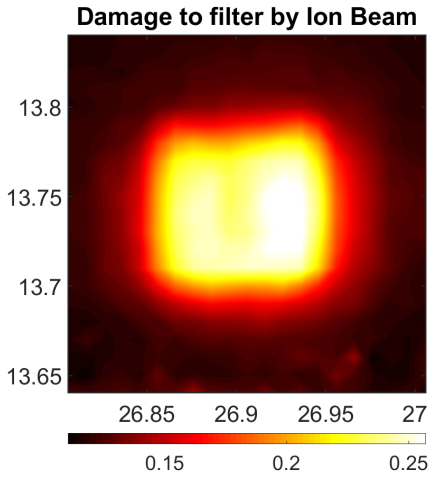

Figure 6.17: Damage to filter xy sample scan. Source wavelength 2.6μm.

3.4μm nanogratings.

6.3.3 Filter damage

In addition to radiation escaping through the sidewalls of the sub-wavelength aperture it was clear there was damage to the filter in areas surrounding the 1D QCW gratings. This damage was highest in the area of the 3.6μm resonant QCW grating and can be seen in Figure 6.17 by the transmission of light through the filter. Figure 6.17 was obtained by removing ND filters and replacing the reflecting objectives with classical CaF_2 convex lenses, this increased the beam size incident on the sample. The damage was not picked up by the transmission scans of the entire filter, this was because the areas in question are small (50x50μm) with respect to the total surface area of the filter and the magnitude of the transmission through the filter is negligible with respect to the transmission in the band pass region of the filter. An ND 0.3 (50% transmission) was used in Figure 6.17 whereas during the whole sample transmission scans ND 1.0 and 2.0 were used in series to reduce the magnitude of light incident on the filter to 0.1% of maximum power. This was to avoid saturating the detector at the band pass. At 0.1% of laser power 0.12mW of transmission was detected through the sample, this is less than 1% transmission when compared with the transmission at the bandpass which is negligible, however this amount of transmission is significant when attempting to measure the light exiting a subwavelength aperture.

On the macro-scale such as the far field distribution, the radiation passing directly through the filter effectively masks the radiation that exits the subwavelength aperture and is re-radiated by the grooves. Analyzing the near field and events taking place on the filter itself, the field

re-radiated by the grooves is smaller than the field passing directly through the filter. The field passing through the filter will interact with the QCW field, which itself is a superposition of evanescent and radiative components, if the two fields were equivalent in size it would result in a more complex superposition of components. However, the field passing through the filter is several times larger and dwarfs the QCWs meaning no detectable contribution from QCWs can be measured.

6.4 QCW nanograting sample two

6.4.1 Overview of geometries and fabrication

As the problems arising from the first filter may be solvable with changes to the fabrication method, a second dielectric bandpass filter was sourced from Northumbria optical coatings. Alongside changing the original fabrication method to decrease the damage to the filter done by the FIB, additional geometries were patterned on the filter to gain a better understanding of aspects of the QCW role in beam shaping. The a schematic of the second sample is shown in Figure 6.18.

First an identical 1D 3.4μm resonant QCW geometry was patterned, with improvements in the patterning method to better protect the filter and prevent the damage as seen in Figure 6.17. This was achieved by under-milling the photo-resist layer as to not directly bombard the filter surface within the field of view (FOV) of the ion beam, patterning accuracy was decreased due to the filter being below the focal plane of the beam however this was an acceptable compromise to better protect the filter from damage. This method was employed for every geometry patterned on the filter.

The second problem to address was the leaking of radiation at the sidewalls of the filter. The filter is a 1D photonic crystal and is optimized to reflect light in a single plane, as such scattered light incident upon the filter at various angles will not be adequately reflected. One of the only ways to decrease the transmission through the sidewalls of the aperture, is to deposit a thin wall of metal. This was a difficult compromise to make as a non metallic infrared beam steering geometry that could be patterned on the facet of a laser was a big motivation for this work, however no other viable options could be found. To prevent SPPs from propagating the metallic sidewalls would have to be extremely thin, for gold, ~50nm.

A 1D 3.4μm resonant QCW geometry with metallic sidewalls was attempted. This was a challenging process, the milling rate of gold was different to that of the filter and the beam waist of the ion beam increased with depth in the filter, this coupled with sample drift made

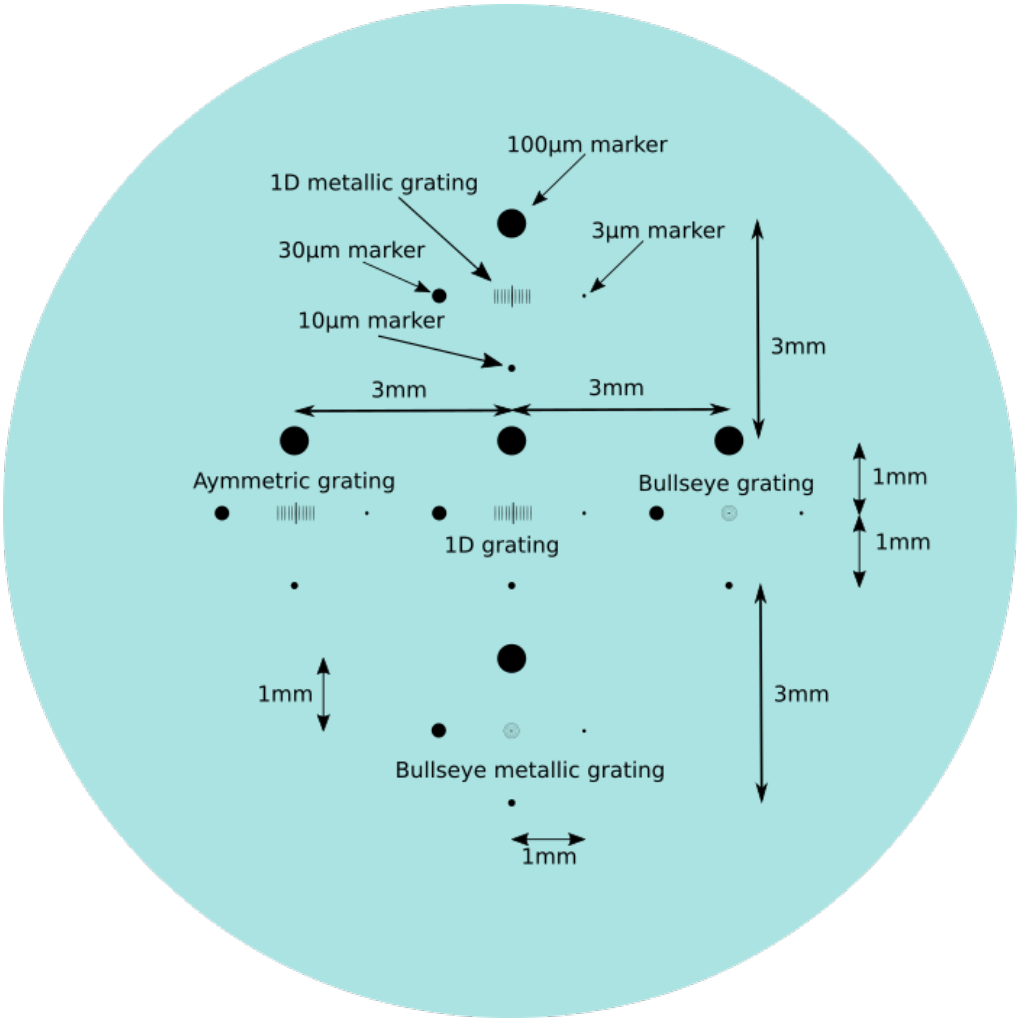

Figure 6.18: Sample map of second NOC bandpass filter

obtaining an acceptable geometry challenging. The top layer of gold was first milled and the photo-resist layer was partially milled to protect the filter in the ion beam's FOV from damage. The 1D 3.4μm resonant QCW geometry was milled following the method outlined in Chapter 5, the subwavelength aperture size was increased from 850nm to 950nm to allow for the 50nm gold sidewalls. Then the FOV was focused on the subwavelength aperture and a 10μm layer of gold was deposition inside the subwavelength aperture via the FEI Nova 600's gas injection system (GIS). A 850nm subwavelength aperture was milled in the newly deposited gold to leave a 50nm gold sidewall. Using the deposited material's sputtering rate, a depth of 200nm further than the original aperture's depth was milled to ensure no gold was present at the bottom of the aperture to prevent incident light from entering the subwavelength aperture, this meant a slight over-mill in the CaF_2 layer below, which was deemed to be acceptable. Several attempts at the 1D 3.4μm resonant QCW geometry with metallic sidewalls were first carried out near the outer edge of the filter and cross sections were taken to determine if the method worked. A varying thickness of sidewall with depth was found, this is likely due to sputtering rate differences between the filter and gold resulting in a steeper sidewall angle in the gold meaning the sidewall decreased in thickness with depth, this was mitigated as much as possible by using a smaller beam current when milling into the gold. This had a compromise as increased pattern times increased sample drift and resulted in asymmetric sidewall thickness. Final cross sections showed an average sidewall thickness of 43nm and 52nm respectively and an average variation in thickness with depth of 27%. A cross section is shown in Figure 6.19, platinum was deposited onto the gold to protect from the sputtering process described in Chapter 5, the gold is the slightly brighter layer between the platinum and the filter. The 1D 3.4μm resonant QCW geometry with metallic sidewalls was then attempted at the location shown in Figure 6.18.

In addition to the two 1D 3.4μm resonant QCW geometries, a 2D grating design was etched into the filter, called a bulls-eye grating, this will be introduced and explained in Chapter 7 alongside the theoretical modelling for it. Finally an asymmetrical 1D 3.4μm resonant QCW geometry was patterned into the filter, with the aim to better understand the role of QCWs in beam shaping, which will also be presented in Chapter 7.

6.4.2 Linear QCW nanograting

The filter was placed in the measurement system and the steps outlined earlier in the Chapter for the first filter, were again followed to ensure a focused beam incident upon the filter and the detector was in an optimised position to map the far field radiation pattern. The filter was then mapped out using the alignment markers to use as a reference tool for navigating the filter.

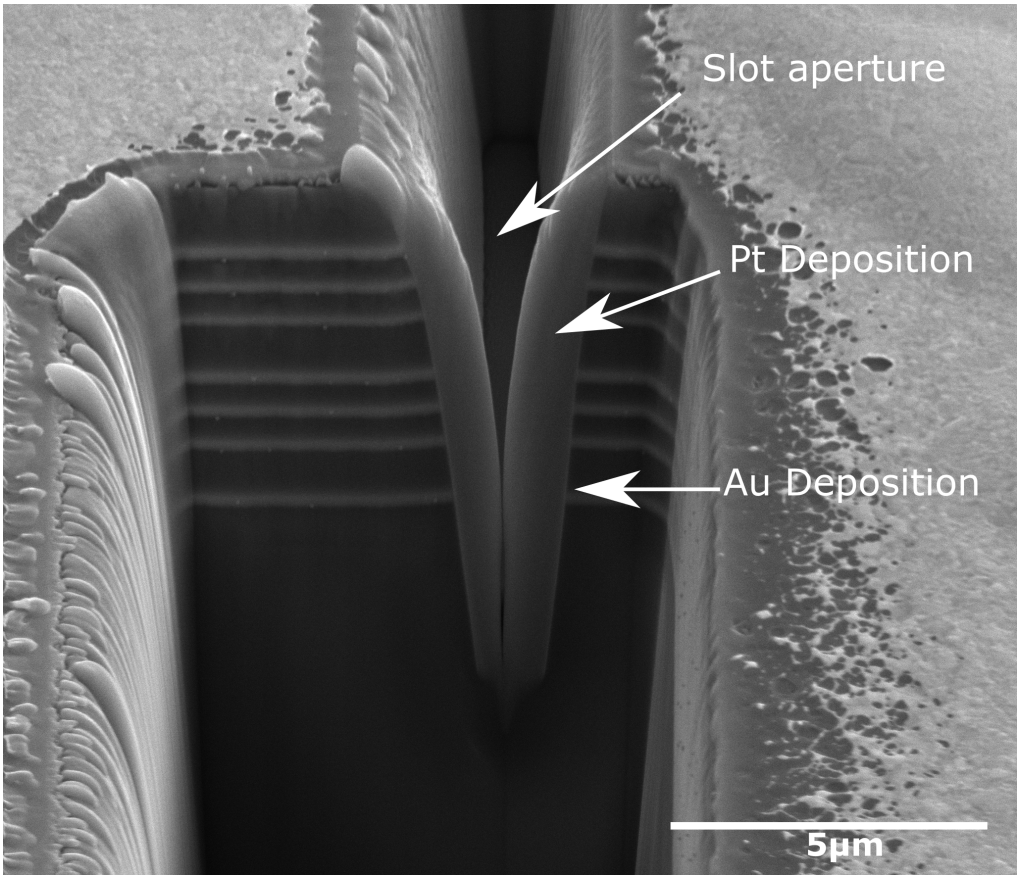

Figure 6.19: SEM cross section of the metallic subwavelength aperture

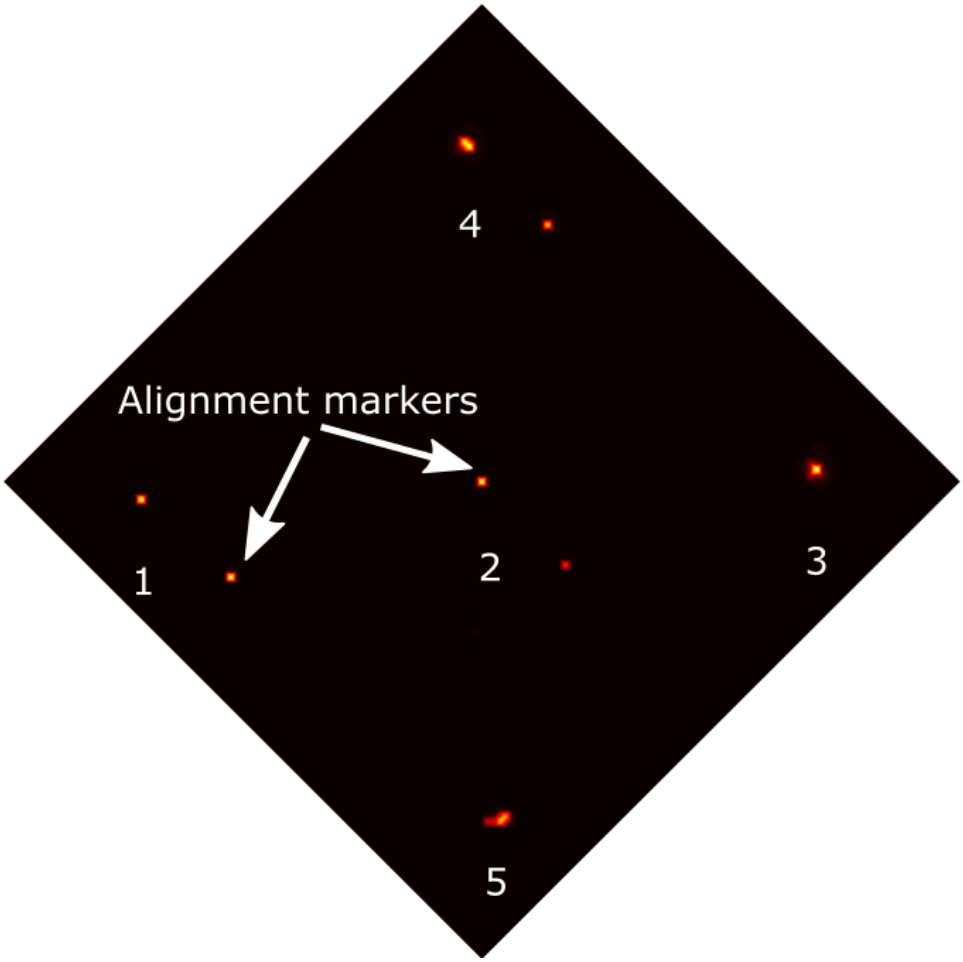

Figure 6.20: Optical sample map of second NOC bandpass filter. Source wavelength 2.6μm.

The resulting sample map is shown in Figure 6.20, cross referencing this with the schematic shown in Figure 6.18, the areas containing each geometry was identified.

The sample was moved to the area containing the linear QCW nanograting. The 30μm and 10μm alignment markers were again used to minimise the beam size and the area containing the linear nanograting was scanned. The nanograting was successfully found and is shown in Figure 6.21. A clear slot like structure is seen but with a lower intensity when compared with the corresponding feature on the first sample, this likely due to a slightly larger spot size but with a clear structure observed, the sample was moved such that the laser was incident on the centre of the aperture.

With the sample position fixed, the detector was moved to collect the resulting far field pattern, this was carried out for wavelengths; 3200nm, 3400nm and 3600nm, to obtain a resonant and two off resonance results. Figure 6.22 shows the far field pattern at resonance

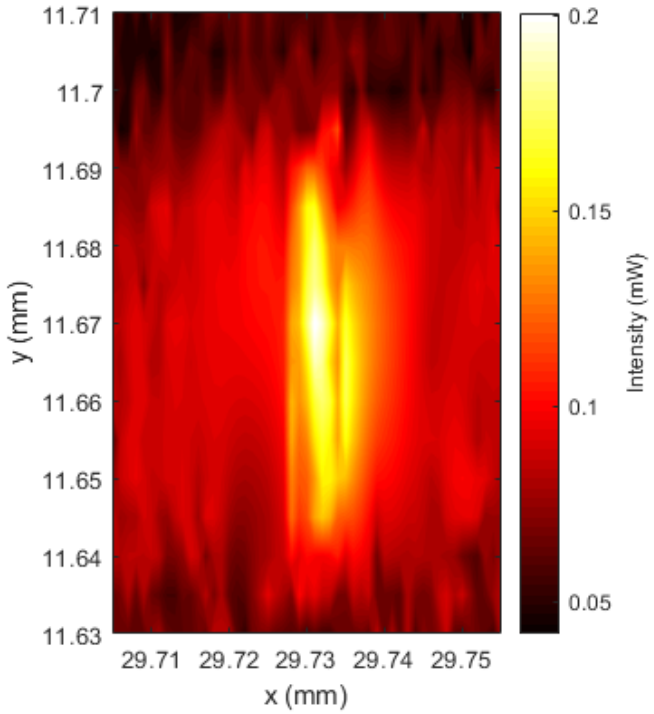

Figure 6.21: 1D grating sample xy scan. Source wavelength 3.4μm.

(3400nm), the beam has a FWHM of 0.41mm in the x direction and 0.37mm in the y direction.

6.4.3 Linear QCW nanograting with metallic sidewall

The sample was moved and refocused onto the 1D geometry containing a subwavelength aperture with a thin gold coating. Figure 6.23 shows the sample scan, the slot structure can be observed but less clearly when compared with the fully dielectric variant. A noticeable decrease in transmission is also seen here. The alignment makers were used to refocus and minimise the spot size of the incident beam, this did not affect the signal profile from the sample scan. It is likely this change in appearance is caused by the metallic deposition during fabrication.

Again the sample position was fixed and the detector was moved to collect the resulting far field pattern for wavelengths; 3200nm, 3400nm and 3600nm to obtain a resonant and two off resonance results. The far field at resonance, shown in Figure 6.24, shows more a more pronounced divergence along the x direction when compared with the fully dielectric geometry's far field. The FWHM is 0.415mm, this compares with an off-resonance FWHM of 0.420mm found at a wavelength of 3200nm. A 5μm decrease in FWHM of the far field

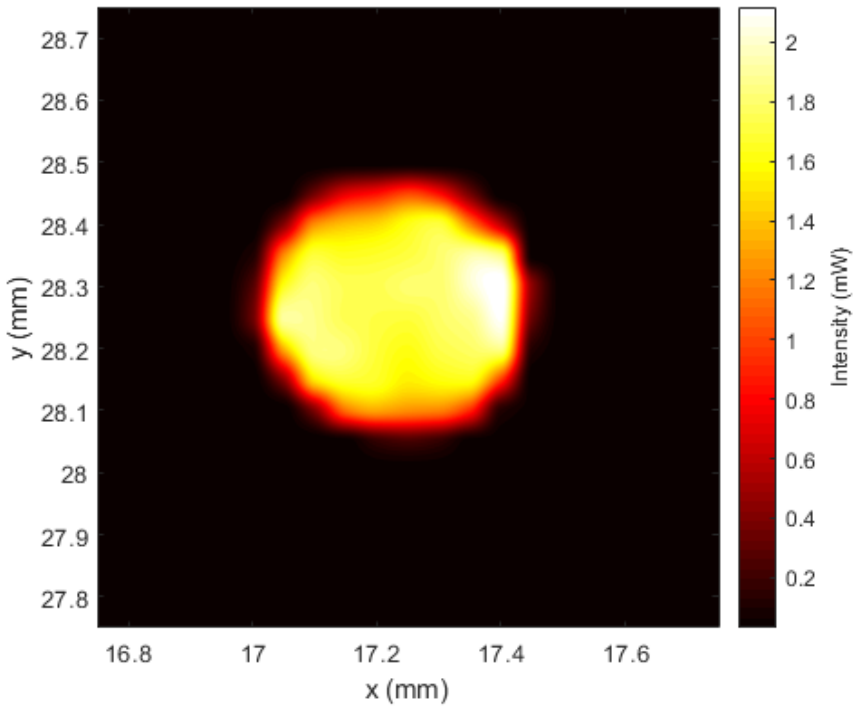

Figure 6.22: 1D grating detector xy scan. Source wavelength 3.4μm.

at resonance falls within the resolution of the measurement, so while this could be a positive result, more investigation is needed.

6.5 Conclusion

In this chapter the optical measurements of resonant nanogratings patterned onto a fully dielectric mid infrared band pass filter have been presented. The optical measurement system was validated by measuring the far field radiation patterns of classical diffraction gratings, which compared well to the calculated pattern. The far field radiation patterns produced by the 3.2μm and 3.4μm resonant nanogratings in the wavelength range of 2400 to 3400nm have been analysed and no beam shaping was found. Upon further investigation at different sample rotations no wavelength or polarization dependence could be seen and it was concluded neither the subwavelength aperture or nanogratings were functioning as expected. Changes to the fabrication method were carried out to overcome problems found with the filter and a second patterned mid infrared band pass filter was presented.

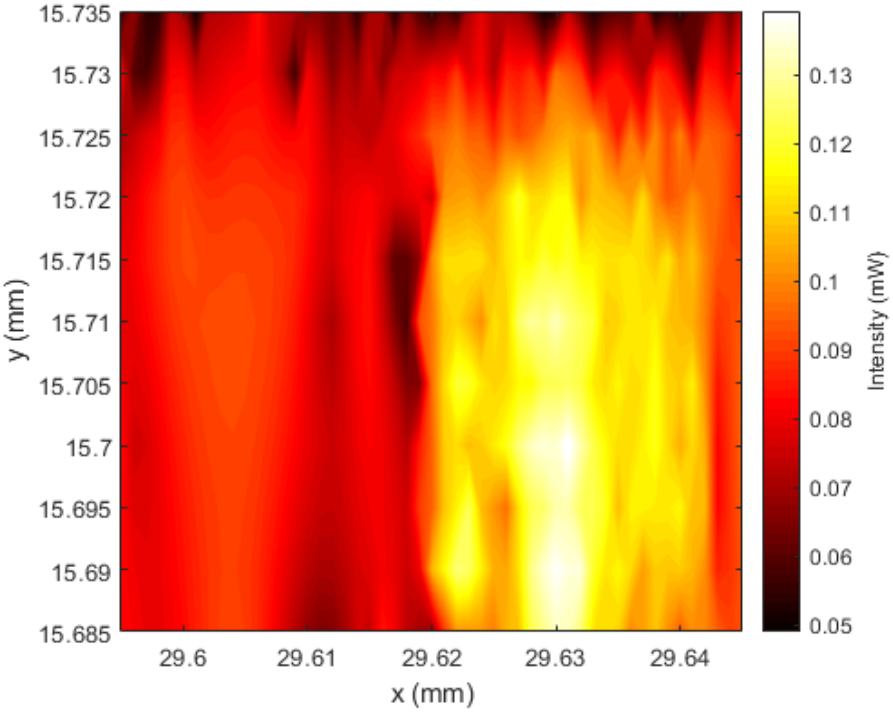

Figure 6.23: 1D grating with metallic aperture sidewalls sample xy scan. Source wavelength 3.4μm.

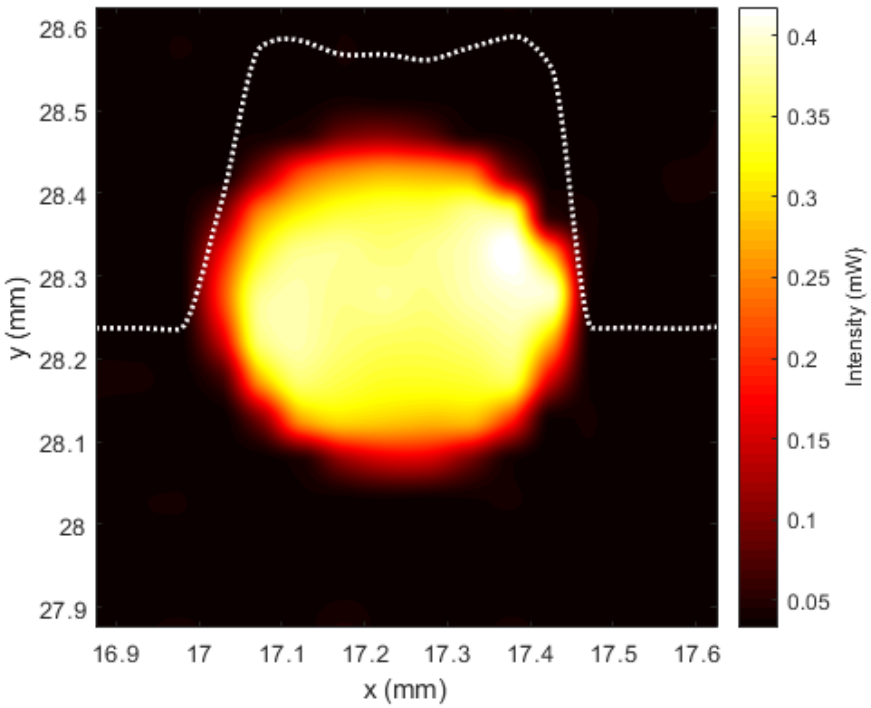

Figure 6.24: 1D grating with metallic aperture sidewalls detector xy scan. Source wavelength 3.4μm.

Chapter 7

Iterative design and QCW characteristics

7.1 Overview

This Chapter presents modelling results and optical measurements on the second dielectric filter outlined in Chapter 6. Modelling results of a bullseye geometry design is presented and analysis of the near and far fields generated by the geometry is given. Fabrication of the geometry is described and SEM and optical microscopy images are presented along with optical measurements of the design. Analysis of the wavelength sensitivity of quasicylindrical waves (QCWs) is carried out. Finally an asymmetrical grating is analysed, with modelling results and optical measurements presented.

7.2 Improved design

7.2.1 Bullseye design

The design discussed in Chapter 4 consisting of an aperture that is subwavelength (850nm) along the x direction and 50μm in the y direction, created a highly divergent beam in the x direction. The divergence was found to be greatly reduced by patterning a series of grooves on the exit side of the device along the x axis. This was adequate as a proof of principle example to show isolated QCWs can be employed to reduce the divergence from a subwavelength aperture. The natural progression once proof of principle has been demonstrated is to move to a geometry that could be used in potential practical applications. Here it would be desirable to reduce the divergence of a beam passing through an aperture that is completely subwavelength in the x-y plane. A fully divergent beam, which is diffracted in all directions by passing through a subwavelength cylindrical aperture will be analysed.

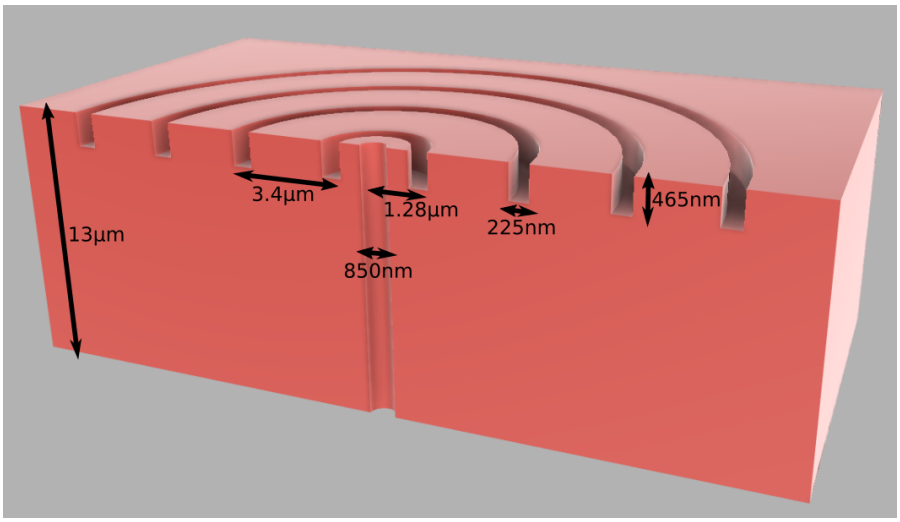

Figure 7.1: 2D slice through the bullseye grating structure used in FDTD simulations.

An FDTD model of a single cylindrical subwavelength aperture, with a diameter of 850nm, through the fully dielectric bandpass filter described in Chapter 4 was created using Lumerical FDTD. A plane wave propagates 1.5µm in free space before reaching the incident side of the subwavelength cylindrical aperture. The incident radiation is scattered at the aperture's entrance, where standing waves are formed within the aperture before exiting at the far side, where the resulting radiation is measured along the xy plane. The electric field intensity of the far field, one metre from the exit side of the aperture is shown in Figure 7.2. The beam is highly divergent is all directions on the xy plane due to the subwavelength diameter of the cylindrical aperture, resulting in a classical 'half-sphere' diffraction pattern. By patterning the exit side with a concentric periodic grating the divergence in all directions can be reduced. The resulting geometry resembles that of a dart board and for that reason will be referred to as the bullseye grating from this point onward. A slice through the bullseye grating structure is shown in Figure 7.1. The starting dimensions for; the first groove to aperture distance, groove depth, groove width and number of grooves are taken from the optimized resonant nanogrooves calculated in the 2D FDTD model in Chapter 4. This should be a good starting approximation because the 3D FDTD bullseye grating model can be created by rotating the 2D FDTD resonant nanogrooves model about z axis by 180º.

Figure 7.3 shows the total magnetic field intensity along the surface on the exit side of the aperture. By taking a snapshot of how the field looks on this plane, we can begin to understand how the magnetic field associated with the QCW evolves as radiation propagates out of the subwavelength aperture. We can see the effect of the source's polarisation, with the magnetic field amplitude much higher along the x direction, at y=0 than along the y-axis at x=0. The

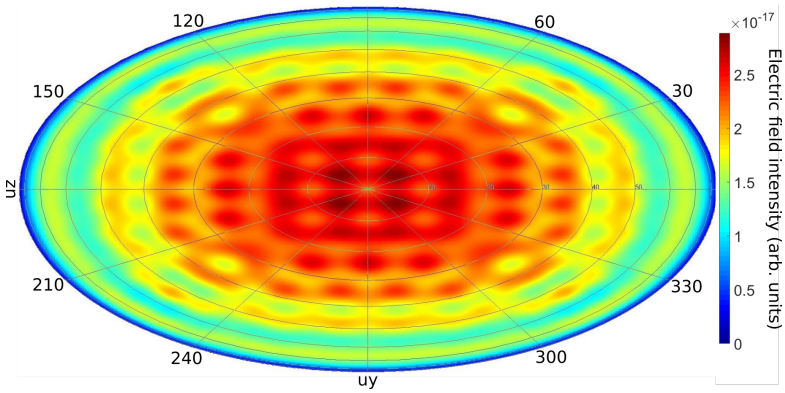

Figure 7.2: Electric field far field intensity of the cylindrical aperture. Plane wave source wavelength 3.4μm.

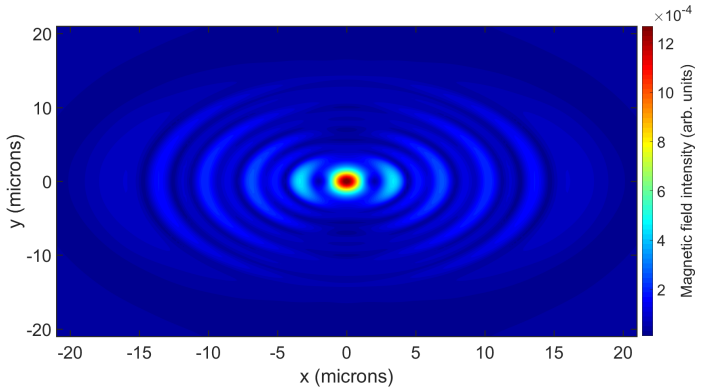

Figure 7.3: Magnetic field along the filter surface for the bullseye grating simulation. Plane wave source wavelength 3.4μm.

total magnetic field amplitude rapidly decays to 50% of the initial value as it exits the aperture and travels along the x-y plane to the first groove, this is indicative of the strong influence of QCWs at short distances. The magnetic field decay lessens as the wave travels from the first groove, outwards all the way to the 10th groove, where the field is negligible.

The field radiated at the exit of the subwavelength aperture and by the grooves is shown in Figure 7.4. This is known as the far field and represents the electric field intensity one metre from the exit side of the aperture. Rather than the flat x,y plane used for representing the near field, a hemispherical surface is used to represent the far field, this ensures a one metre distance from the centre of the subwavelength aperture's exit in all positive directions which allows for direct comparison with how the electric field propagates at different angles. Figure 7.4 shows up to 50º from the zeroth direction and illustrates that the exit beam is highly directional, with the high intensity electric fields contained within 5º either side of the zeroth direction, rapidly decays in amplitude to almost zero outside of 10º. In contrast to the highly divergent beam

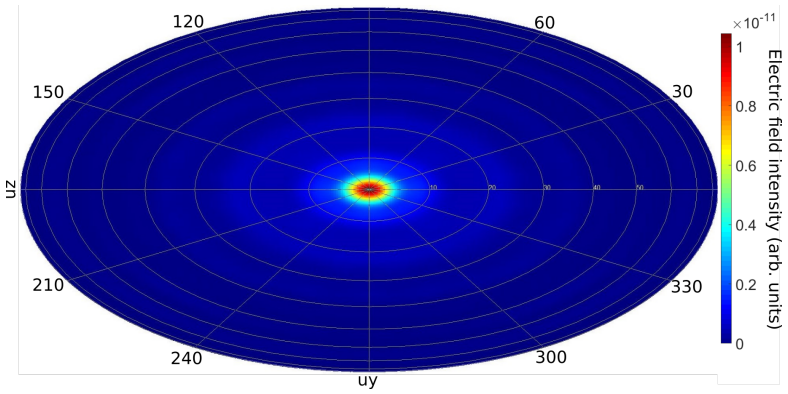

Figure 7.4: Electric field intensity of the far field for the bullseye grating simulation. Plane wave source wavelength 3.4μm.

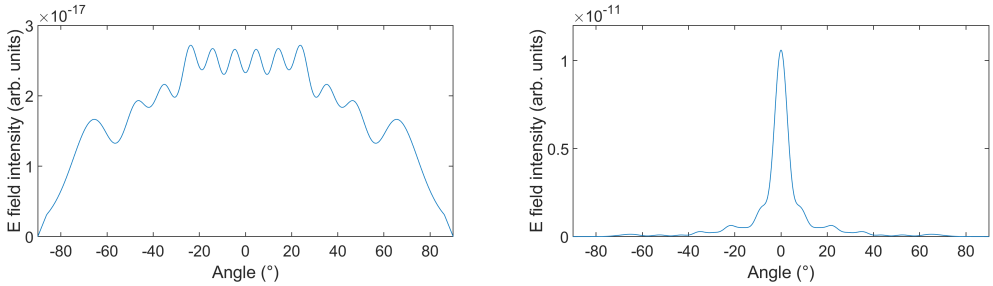

Figure 7.5: FWHM of the bullseye output beam for grooves (right) and aperture only (left). Plane wave source wavelength 3.4μm.

shown in Figure 7.2.

The effect of the grooves on the far field can be seen in Figure 7.5. The FWHM is reduced from 144.8º to 4.1º and the peak intensity of the beam increases dramatically.

7.2.2 Bull's-eye fabrication

The optimized geometry was then patterned onto the second off-the-shelf mid-infrared dielectric band pass filter sourced from Northumbria Optical Coatings limited, using a focused ion beam (FIB). Two versions of the bullseye geometry were patterned on the filter; a fully dielectric geometry and a variant with 50nm of gold coating the subwavelength aperture sidewalls. For the fully dielectric variant the fabrication process was identical to that of the first filter which was described in Chapter 5, an SEM image of this geometry is shown in Figure 7.6. The geometry with metallised sidewalls used an updated fabrication method outlined in Chapter 6.

Figure 7.7 shows optical microscope images of the filter after the PMMA photo-resist layer

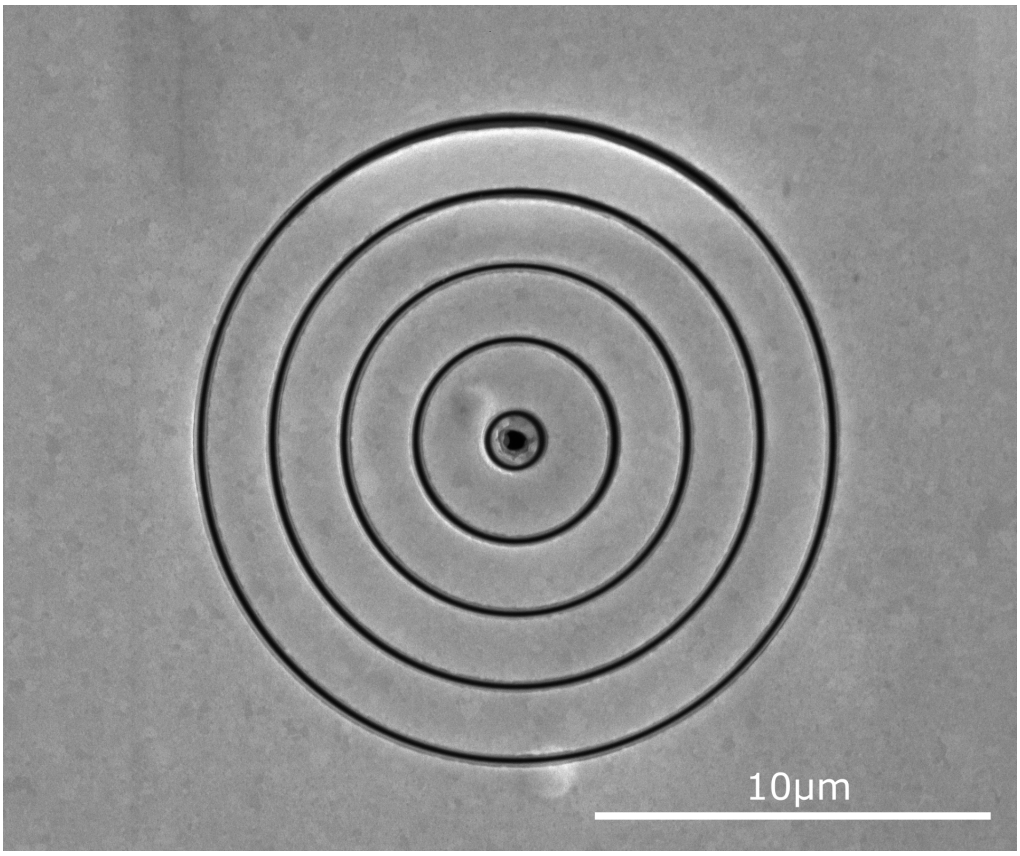

Figure 7.6: SEM image of the patterned bullseye grating

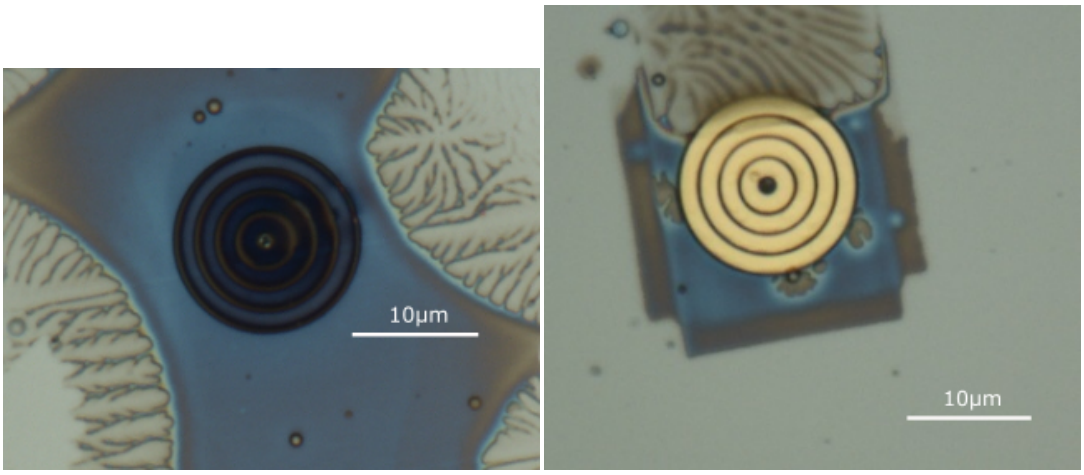

Figure 7.7: Optical microscope images of the patterned bullseye grating

had been dissolved in acetone, lifting off the top layer of gold needed for imaging in the FIB. The left image is the fully dielectric filter and shows a successful lift off. The right image is the metallised sidewall variant, unfortunately the lift off process was unsuccessful and metal remained on the filter surface. A full schematic of the filter can be found in Chapter 6, Figure 17.

After the lift off process was completed, the filter was placed in the measurement system. 100μm, 30μm, 10μm and 3μm alignment markers were used to minimise the laser's spot size incident onto the filter and identify the area in which the fully dielectric bullseye geometry was located. A 100μm square area was raster scanned but no increase in transmission associated with being incident upon the sub-wavelength aperture was found. The minimum repeatable step size of the sample's motorized stage was used (800nm) and the reflecting objective with the highest numerical aperture (0.5) available was focusing light onto the sample. Without knowing the intensity of light scattered by the exit side of the subwavelength aperture, upgrades to the measurement system were not guaranteed to pick up a signal. Concluding that no addition steps could be made in the time remaining, data acquisition of the one-dimensional geometries was prioritised. Figure 7.8 shows the area of the filter occupied by the bullseye grating, as shown, no increase in transmission was detected and the aperture of the bullseye grating could not be located. This is likely due to imperfect fabrication, with either gold blocking the entrance of the aperture or light not being confined by the aperture sidewalls.

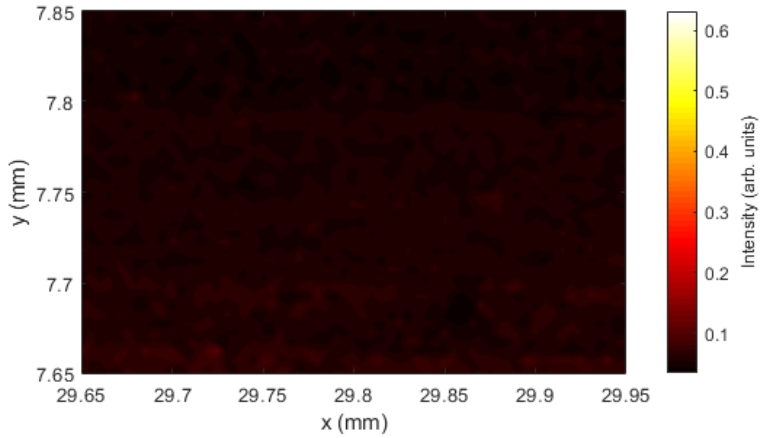

Figure 7.8: Sample xy scan in the area containing the bullseye grating. Source wavelength 3.4μm

7.3 Sensitivity

7.3.1 Wavelength sensitivity

The effect of the adding resonant nanogrooves around a subwavelength aperture has been analysed for both the bullseye grating and the linear grating (Chapter 4). The sensitivity of the design to wavelength change will be analysed here by observing changes to both the near and far field at different frequency points. Unlike surface plasmon polaritons (SPPs), QCWs have not been extensively studied and due to being a superposition of evanescent and propagating waves it is not obvious how sensitive they may be to wavelength change. This analysis will help gain insight to QCW wavelength sensitivity which will help with potential applications to this design and any device that employs isolated QCWs as well as elucidate the physics of the beam formation on the exit side of the filter.

The FDTD method is capable of sweeping over a large wavelength range in a single simulation making it a suitable method to carry out such analysis. The initial simulation started with a broadband plane wave source with a wavelength span of 2.9μm to 3.9μm and the electromagnetic field on the exit side of the filter was recorded at 100nm wavelength intervals. The magnetic field along the exit side surface is shown in Figure 7.9, the sensitivity to wavelength change appears to decrease at longer wavelengths, shown with the longer wavelength having a higher peak (ie. a smaller drop from the resonant peak) than the shorter wavelength. At 3.3μm the magnetic field drops off over a shorter distance, this drastic decrease in magnetic field intensity occurs at 500nm from the aperture and the scattering from the grooves is greatly diminished.

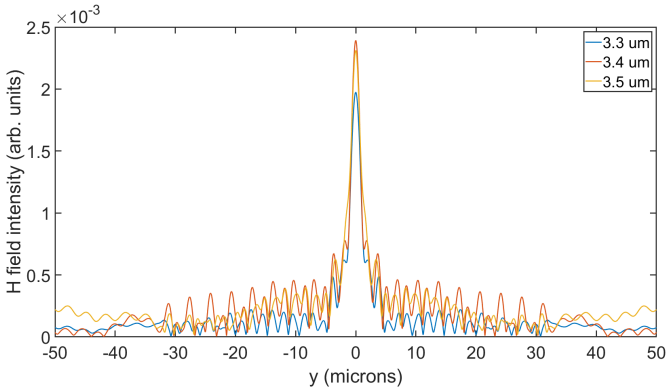

Figure 7.9: Near field wavelength sweep.

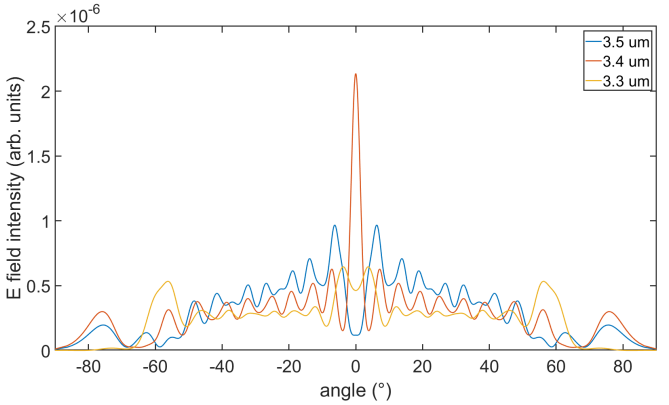

Figure 7.10: Far field wavelength sweep.

The electric field intensity one metre away from the exit surface of the filter is shown in Figure 7.10, the result of the fast drop off in magnetic field and low interaction with the grooves seen in the near field is illustrated here. There is no meaningful collimation on the exit side, hinting that the field along the exit side surface is not efficiently reradiated by the grooves. The impact of these large differences to the near and far fields caused by changes in the wavelength in 100nm steps show the device to be sensitive to wavelength changes. The next step was to investigate the effects of smaller frequency changes. A smaller wavelength range of 3.35μm to 3.45μm was studied with wavelengths steps reduced to 10nm.

Figure 7.11 shows the magnetic field along the exit surface, the smaller step size in wavelength has resulted in good interaction with the grooves in the near field. As with the larger step size, a larger shift away from the resonance magnetic field profile is seen at the smaller wavelength, the field strength decreases faster before reaching the first groove.

Figure 7.12 shows the electric field intensity at a distance of 1m from the exit surface of the filter. A smaller wavelength change of 10nm results is shift in maximal electric field

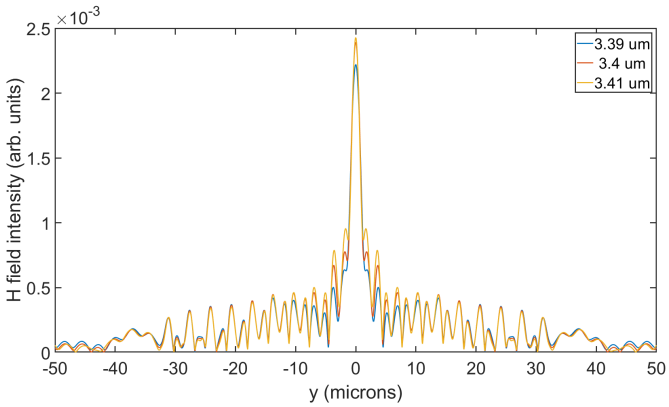

Figure 7.11: Near field wavelength sweep.

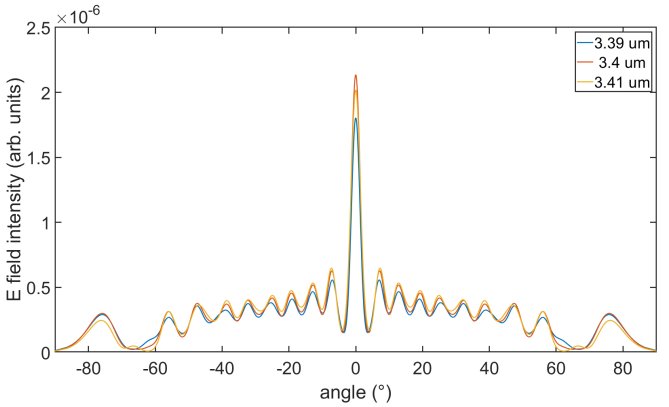

Figure 7.12: Far field wavelength sweep.

intensity of 30% and 10% respectively, however the collimation effect is still present. It was found at a shift of 25nm from the resonance wavelength the collimation effect was negligible. This highlights that the light source needs to be carefully chosen, a source with a central wavelength that is more than 25nm either side of its stated wavelength could result in no collimation from the grating. This result also shows that QCW resonant structures require high precision fabrication in order to interact with the field efficiently and collimate the beam.

7.4 Asymmetry

Following the large decrease seen in the magnetic field along the surface of the filter between the aperture and the first groove, when small changes to incident wavelength were made, changes in the aperture to first groove distance were investigated. Figure 7.13 shows the geometry being investigated. The aperture width, grating constant, groove width and groove height were all kept constant and the optimised values found in Chapter 4 were used. The

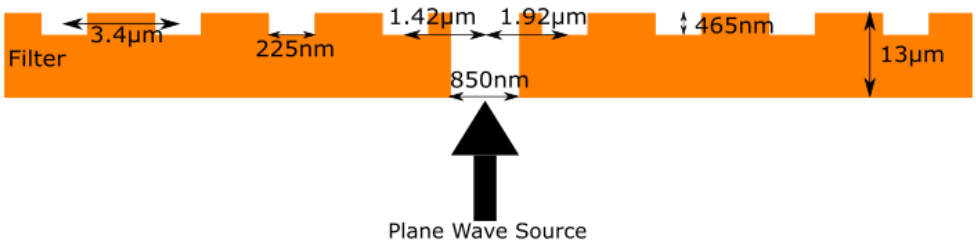

Figure 7.13: Asymmetric grating geometry

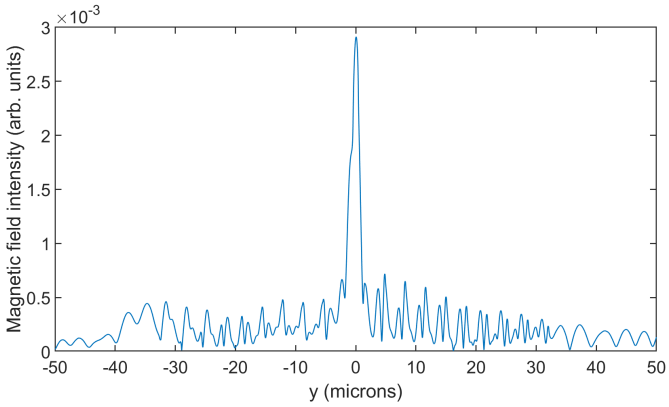

Figure 7.14: Asymmetric grating near field. Plane wave source wavelength 3.4μm.

aperture to first groove distance was investigated in a series of simulations using Lumerical FDTD and it was concluded that having an offset of 1.92μm and 1.42μm respectively provided the changes to the near and far field needed to illustrate how vital this distance was to collimation and to hopefully be able to measure the asymmetry with the optical measurement system.

Figure 7.14 shows the magnetic field along the exit surface of the filter. The right side of the figure has an aperture to first groove distance of 1.42μm and the left 1.92μm. The two sides have very different magnetic field profiles, the field decreases much faster with the larger aperture groove distance and interacts far less with the second groove onward. This is contrasted with the smaller first groove distance side, where the field interacts with the grooves more consistently, given that the grating constant is the same, this could be due to the magnitude of the field after it passes the first groove.

Figure 7.15 shows how the electromagnetic field propagates in the first 200μm upon being radiated from the exit side of the filter. The radiated field is stronger on the shorter first groove distance side and the radiation patterns shows a clear asymmetry.

Figure 7.16 shows a 1D slice of the far field at the focal point of the output beam. The

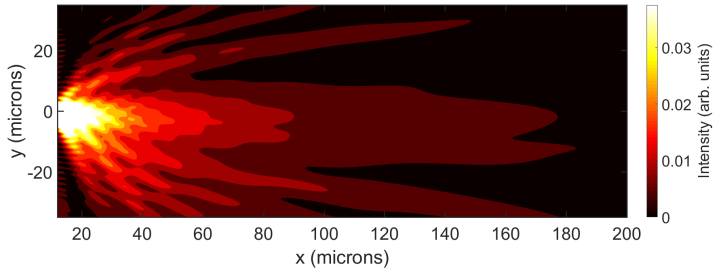

Figure 7.15: Asymmetric grating far field intensity. Plane wave source wavelength 3.4μm.

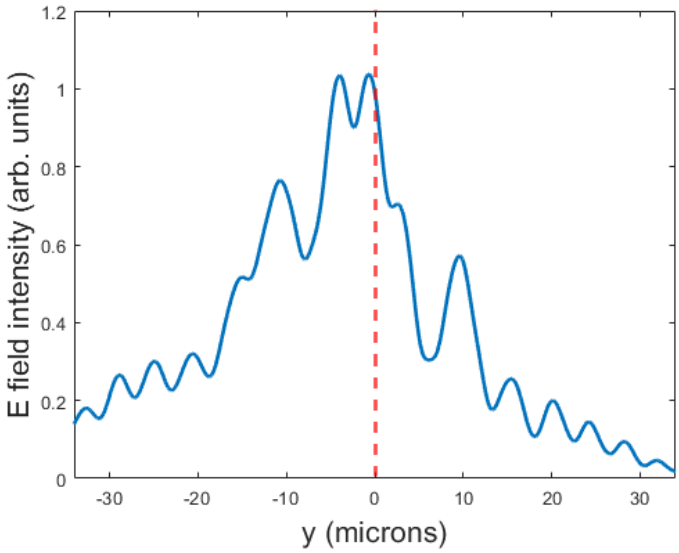

Figure 7.16: Asymmetric grating beam profile at focal point. Plane wave source wavelength 3.4μm.

FWHM is calculated to be 19.9μm and there is clear evidence of asymmetry. The red dotted line in the figure denotes the central line (centre of the aperture), this shows that the beam has been steered off centre, highlighting potential for beam steering. Expanding the calculation to one metre away from the aperture, the centre of the beam is located at an angle of 0.5º left of centre.

7.4.1 Asymmetry optical measurements

The asymmetry design was fabricated onto the second band pass filter sample, the modified fabrication steps are given in Chapter 6. An SEM image of the geometry is shown in Figure 7.17.

The sample was then placed in the measurement system and laser's spot size minimised

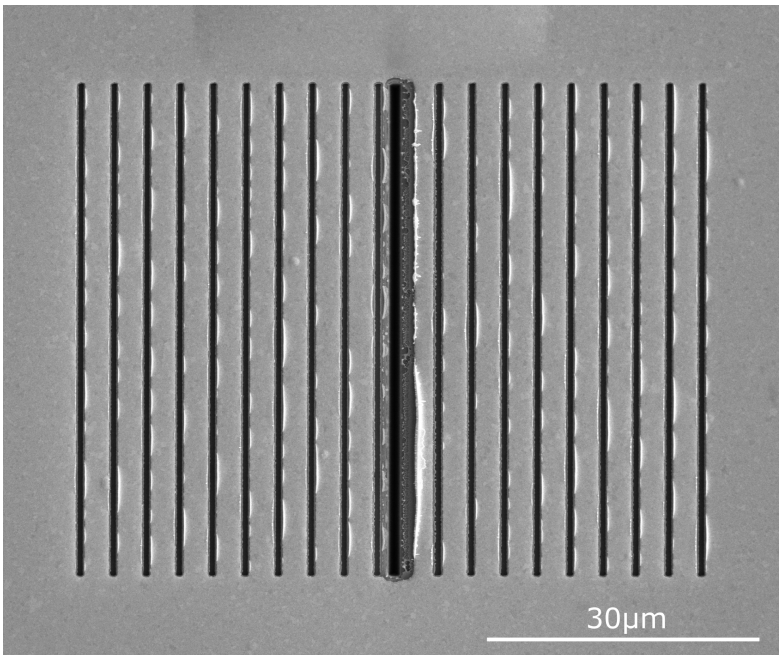

Figure 7.17: Asymmetric grating SEM image, pre lift-off.

with the alignment markers adjacent to the asymmetry grating. The filter was then translated in the xy plane until the grating aperture was found. The raster scan is shown in Figure 7.18.

The sample was then moved until the laser was incident upon the aperture entrance. The sample was then fixed in position and the detector translated in the xy plane to collect the far field radiation pattern, this was done for a wavelength range of 3.2µm to 3.6µm, in 50nm steps. The resonant wavelength far field scan is shown in Figure 7.19. There is a noticeable area of higher intensity to the right of the beam, which is supported the simulations discussed above. The FWHM is measured to be 0.42mm at resonance, the FWHM does not vary significantly over the wavelength range measured with the lowest values coming at either side of resonance, 3350nm and 3450nm measured two microns less than resonance. No conclusive evidence of beam collimation was found but the high area of intensity over the the right side of the measured far field beam is evidence that the grating was beaming asymmetrically.

7.5 Summary

In this chapter the modelling results of a bullseye grating were presented showing collimation in the xy plane and fabrication results were shown. Unfortunately the bullseye grating was unable to be found by the optical measurement system. Analysis of the wavelength sensitivity of the linear quasicylindrical wave geometry carried out and concluded that collimation can only

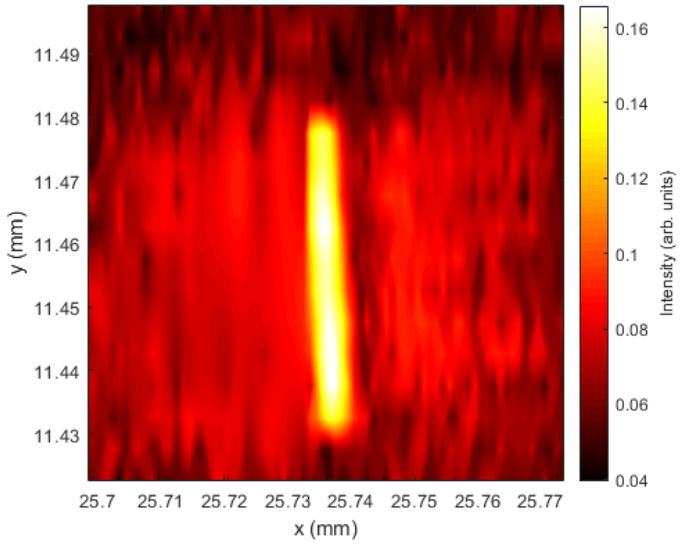

Figure 7.18: Asymmetric grating sample xy scan. Source wavelength 3.4μm.

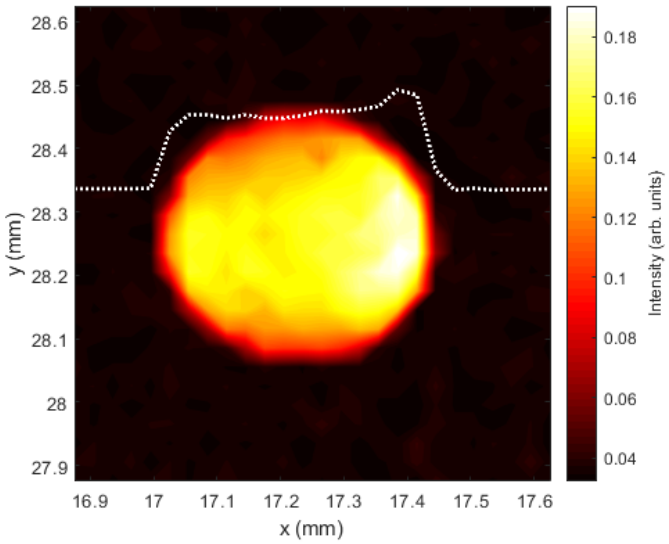

Figure 7.19: Asymmetric grating detector xy scan. Source wavelength 3.4μm.

been observed for incident beams that are within 25nm of the resonance wavelength, limiting potential applications for light sources with larger bandwidths. Modelling and optical results for an asymmetric 1D slit grating were presented, highlighting the large effect the aperture to first groove distance has on the output beam characteristics. The simulations showed potential for beam steering and although no collimation could be detected by the optical system, evidence of an asymmetrical output beam was found.

Chapter 8

Conclusion and Future Work

8.1 Overview

The work presented in this thesis focuses on the development of a fully dielectric subwavelength aperture groove structure optimised to collimate light in the mid-infrared by supporting quasicylindrical wave (QCW) propagation. The motivation behind implementing such a structure is to provide an alternative to metallic aperture-groove structures that support surface plasmon (SP) propagation to collimate light and change other beam characteristics such as polarisation. When integrating such a structure onto an active device, depositing metal is not desirable. An extra layer of insulation needs to be deposited to avoid a short circuit and in some cases an additional insulation channel is needed to prevent the device from a high malfunctioning rate [30]. These added fabrication steps increase costs and complexity of manufacture. SPs also perform less optimally at longer wavelengths where losses are high. Increasing the power density output of light sources at these infrared wavelengths has numerous applications including gas-sensing, free space communications and remote sensing [80].

8.2 Conclusions

Structures designed, modelled and fabricated in this project were integrated onto a commercially available, fully dielectric mid-infrared band pass filter. To accurately model and optimise these structures, properties of the dielectric band pass filter had to be known. Cross sections of the filter were etched using a focused ion beam (FIB) system to characterise the filter. The filter was confirmed to be a 1D photonic crystal, consisting of alternating layers of dielectric with high and low refractive indices and a cavity. The number of layers, thickness of each layer and position of the cavity were identified and modelled using the transfer matrix

method (TMM). These were fitted to known dielectric materials to develop a good approximation to the commercial available filter. The approximation consisted two dielectric stacks separated by a cavity, using alternating layers of stibnite and chiolite. The modelled filter had a total thickness of 13.1μm with a narrow band pass at 2.91μm. This design was recreated in two dimensions and verified with the finite difference time domain (FDTD) method.

The remainder of the simulations were carried out in Lumerical FDTD. A aperture-grating structure was designed for a 3.4μm light source, made up of a 850nm slit aperture, surrounded by a linear grating consisting of 10 slit grooves each side, of height 350nm and width 300nm. The grating period was 3.4μm and aperture to first groove distance was 1.35μm. This structure was contrasted against an isolated 850nm aperture and the grooves were found to decrease the full-width half-maximum (FWHM) of the output beam from 129.8º (without grooves) to 4.1º when the incident light had a wavelength of 3.4μm. This structure was further optimised using a population based stochastic optimisation technique. The grating period and aperture width were kept constant. The grooves width and aperture to first groove distance was reduced to 225nm and 1.28μm respectively and the groove height increased to 465nm. This resulted in a further reduction of the output beam's FWHM from 4.1º to 3.4º. Finally the model was expanded to three dimensions and the reductions in FWHM confirmed. The simulations show the potential for using QCWs to collimate mid-infrared light exiting a subwavelength aperture

The optimised geometry was then patterned onto the commercial fully dielectric mid-infrared band pass filter using a focused ion beam (FIB). First the top surface of the filter coated with a photo resist. The filter was spin coated with a 150nm layer of 950K A4 solution of polymethyl methacrylate (PMMA). Then a 80nm layer of gold was thermally evaporated on-top of the PMMA, this conducting layer was needed only during fabrication, to stop charge build up during the patterning process. The optimised geometry was successfully patterned onto the filter using the FIB alongside alignment markers, classical diffraction gratings and two variants of the optimised geometry, for 3.2μm and 3.6μm incident light. The conducting layer was then lifted off by dissolving the PMMA layer in acetone. These fabrication steps successfully produced a fully dielectric and patterned filter within acceptable tolerances of the designed and modelled geometry.

Optical measurements were performed on the patterned filter. Pre- and post-fabrication transmission measurements were taken and showed no significant damage had been done to the light blocking ability of the filter. Far field measurements of the classical diffraction gratings were performed, and the resulting diffraction pattern compared to calculated values. Good agreement was found between the calculated and measured far field, thus validating the optical measurement system. Far field measurements were taken with the laser spot focused upon the 3.2μm, 3.4μm and 3.6μm QCW gratings. Analysis was performed, concluding that no mea-

surable beam collimation had occurred and that light may be escaping through the sidewalls. Simulations in Chapter 4 support this hypothesis, requiring a 50nm layer of perfect electrical conductor (PEC) on the aperture sidewalls to confine the radiation within the aperture.

A second dielectric bandpass filter was patterned with changes to the fabrication method, including 50nm of gold being deposited on the sidewalls of the subwavelength aperture. Optical measurements were again performed and showed a 5μm decrease in the FWHM at resonance, this result fell within the resolution of the optical system and thus was not conclusive evidence of collimation.

Additional geometries were also patterned on the second filter, including a 2D 'bullseye' structure. Simulations showed a reduction in FWHM of 144.8º to 4.1º throughout the xy plane however the structure could not be found by the optical system and no far field measurements could be performed. An asymmetrical 1D slit geometry was designed and modelled and analysis on the far field produced valuable insight to the coupling mechanics of the QCW on a dielectric surface. Optical measurements were taken on the asymmetrical grating however no collimation or asymmetry could be detected in the far field pattern. Lastly the sensitivity to incident wavelength of the coupling geometry was investigated. Changes in wavelength of 100nm resulted in no collimation effects, wavelength changes needed to be within 25nm of the resonant wavelength to have a reduction of the output beam's FWHM. This suggests fabrication tolerances need to be within 25nm and the light source carefully chosen, with a small bandwidth in order to interact with the geometry sufficiently to produce collimation.

In summary the FDTD models described in this thesis showed potential for fully dielectric mid-infrared beam collimation, using QCWs, provided light could be confined within the aperture. However experimental results were less conclusive with no collimation measured in the fully dielectric filter and collimation within experimental error found in a second filter (with 50nm of gold deposited on the aperture sidewalls).

8.3 Future Work

8.3.1 Confining light within the aperture

The potential for fully dielectric mid-infrared beam collimation has been demonstrated by the modelling work presented in this thesis. To realise this potential, collimation needs to be demonstrated in experiment. The key point to address is confining the light within the aperture. In this work 1D photonic crystals were used in experiment, in the form of a dielectric band pass filter. Light is only efficiently blocked in one plane and because light is scattered in all

directions when incident upon the subwavelength aperture, the 1D photonic crystal fails to confine light within the aperture. Dielectric waveguides would be an alternative approach to confine the light in the subwavelength aperture. Although the challenges of integrating them with the aperture made such an approach beyond the scope of this project, it could be addressed in a future project. Perhaps a more commercial step would be to integrate structures designed in this thesis on actives devices, such as those described in Chapter 1. Many of these devices already contain dielectric waveguides and would only require the dielectric facet's surface directly patterned, assuming a fabrication method can be found which does not damage the facet. Provided it works, this would also move the concept on in terms of technology readiness level (TRL).

8.3.2 Commercial viability

For optical components not integrated into an active device, a dielectric waveguide could be an expensive solution. A more cost effective alternative could be to incorporate a 3D photonic crystal. Recent advances in the field of metamaterials has demonstrated this can be done in a cost effective and scaleable way, which would be ideal from a industrial standpoint for stand alone optical components. Zhai et al embedded resonant polar dielectric micro-spheres randomly in a polymeric matrix, demonstrating a 0.93 emissivity from the layer across the 8-13μm atmospheric window [84]. They demonstrated a high-throughput, economical roll-to-roll manufacturing of the randomized glass polymer hybrid metamaterial, showing the commercial viability of such a design. By carefully selecting the size and concentration of the micro-spheres along with the materials for the both the micro-spheres and polymer, a highly reflective, dielectric mid-infrared layer could be designed. This would have the ability to reflect light in all directions, confining the light to the aperture. An additional step needed here for commercial viability would be a scaleable patterning method to fabricate the nanostructures needed for beam collimation. A variety of techniques for large-scale patterning of planar structures are available ranging from deep UV lithography, to nanoimprint lithography and soft lithography [50].

8.3.3 Beam characteristics

Finally further work into other desirable beam characteristics could be undertaken. Beam steering, polarisation, Bessel beams and other special beams could be possible. Yu et al reported multi beam emission and spatial wavelength demultiplexing of a semiconductor laser by metallising and patterning the facet of a mid-infrared quantum cascade laser (QCL) [81]. This was achieved by exciting SPs on two gratings, with two different periods, on the same

facet and resulted in the emission of two collimated beams in different directions. Such a design could be used in interferometry and holography. Dolev et al experimentally demonstrated holographic beam shaping by forming free-space beams of arbitrary shapes from SP coupling [12]. An accelerating Airy beam, a focused beam and a vortex beam were all demonstrated. All these experiments could be attempted with QCW coupling on fully dielectric devices. Given the superposition of evanescent and radiative components that make up a QCW, this approach could deliver beam characteristics that SPs cannot.

References

[1] A. E. Siegman. *Lasers*. University Science Books, 1986. URL https://books.google.ch/books?id=1BZVwUZLTkAC.

[2] M Y Ali, W Hung, and Y Q Fu. A Review of Focused Ion Beam Sputtering. *International Journal of Precision Engineering and Manufacturing*, 11(1):157–170, 2010. ISSN 1229-8557. doi: 10.1007/s12541-010-0019-y.

[3] Angela S. Camacho. Focusing Nanoplasmonics. *Nano Science and Technology*, 3(10-17), 2015.

[4] J. N. Baillargeon, P. K. York, C. A. Zmudzinski, G. E. Fernández, K. J. Beernink, and J. J. Coleman. High-power phase-locked InGaAs strained-layer quantum well heterostructure periodic laser array. *Applied Physics Letters*, 53(6):457–459, 1988. ISSN 00036951. doi: 10.1063/1.99883.

[5] William L Barnes. Surface plasmon-polariton length scales: A route to sub-wavelength optics, apr 2006. ISSN 14644258. URL http://stacks.iop.org/1464-4258/8/i=4/a=S06?key=crossref.ee31646dd6259a2f38bfc889072c44fe.

[6] William L. Barnes, Alain Dereux, and Thomas W. Ebbesen. Surface plasmon subwavelength optics, aug 2003. ISSN 00280836. URL http://www.nature.com/doifinder/10.1038/nature01937.

[7] Jean-Pierre Berenger. A perfectly matched layer for the absorption of electromagnetic waves. *Journal of Computational Physics*, 114(2):185–200, oct 1994. ISSN 00219991. doi: 10.1006/jcph.1994.1159. URL http://linkinghub.elsevier.com/retrieve/pii/S0021999184711594.

[8] H. A. Bethe. Theory of diffraction by small holes. *Physical Review*, 66(7-8):163–182, 1944. ISSN 0031899X. doi: 10.1103/PhysRev.66.163.

[9] V. Betz and R. Mittra. Comparison and evaluation of boundary conditions for the absorption of guided waves in an FDTD simulation. *IEEE Microwave and Guided Wave Letters*, 2(12):499–501, dec 1992. ISSN 1051-8207. doi: 10.1109/75.173408. URL http://ieeexplore.ieee.org/document/173408/.

[10] Robert E. Collin. Hertzian dipole radiating over a lossy earth or sea: Some early and late 20th-century controversies. *IEEE Antennas and Propagation Magazine*, 46(2):64–79, 2004. ISSN 10459243. doi: 10.1109/MAP.2004.1305535.

[11] Zheng Cui. *Nanofabrication : principles, capabilities and limits*. Springer, 2008. ISBN 9780387755779.

[12] Ido Dolev, Itai Epstein, and Ady Arie. Surface-plasmon holographic beam shaping. *Physical Review Letters*, 109(20):1–5, 2012. ISSN 00319007. doi: 10.1103/PhysRevLett.109.203903.

[13] T. W. Ebbesen, H. J. Lezec, H. F. Ghaemi, T. Thio, and P. A. Wolff. Extraordinary optical transmission through sub-wavelenght hole arrays. *Nature*, 391(6668):667–669, feb 1998. ISSN 00280836. doi: 10.1038/35570. URL http://www.nature.com/doifinder/10.1038/35570.

[14] Andrei M. Efimov. *Optical constants of inorganic glasses*. CRC Press, 1995. ISBN 0849337836. URL https://books.google.co.uk/books/about/Optical{_}Constants{_}of{_}Inorganic{_}Glasses.html?id=A0qMBgqQstwC{&}redir{_}esc=y.

[15] Andrew Estroff and Bruce W. Smith. Tuning metamaterials for applications at DUV wavelengths. *International Journal of Optics*, 2012:1–7, 2012. ISSN 16879384. doi: 10.1155/2012/603083. URL http://www.hindawi.com/journals/ijo/2012/603083/.

[16] Jonathan A. Fan, Mikhail A. Belkin, Federico Capasso, Suraj Khanna, Mohamed Lachab, A. Giles Davies, and Edmund H. Linfield. Surface emitting terahertz quantum cascade laser with a double-metal waveguide. *Optics Express*, 14(24):11672, 2006. doi: 10.1364/oe.14.011672.

[17] U. Fano. The Theory of Anomalous Diffraction Gratings and of Quasi-Stationary Waves on Metallic Surfaces (Sommerfeld's Waves). *Journal of the Optical Society of America*, 31(3):213, 1941. ISSN 0030-3941. doi: 10.1364/JOSA.31.000213. URL https://www.osapublishing.org/abstract.cfm?URI=josa-31-3-213.

[18] Ugo Fano. Some theoretical considerations on anomalous diffraction gratings [5], sep 1936. ISSN 0031899X. URL https://link.aps.org/doi/10.1103/PhysRev.50.573.

[19] Ugo Fano. On the anomalous diffraction gratings. II [1], feb 1937. ISSN 0031899X. URL https://link.aps.org/doi/10.1103/PhysRev.51.288.

[20] FEI Company. xT Nova NanoLab User's Manual. 2006.

[21] V Friedli and I Utke. Optimized molecule supply from nozzle-based gas injection systems for focused electron- and ion-beam induced deposition and etching: simulation and experiment. *Journal of Physics D: Applied Physics*, 42(12):125305, jun 2009. ISSN 0022-3727. doi: 10.1088/0022-3727/42/12/125305. URL http://stacks.iop.org/0022-3727/42/i=12/a=125305?key=crossref.b59d38355f1e7aba588333ecab4065c9.

[22] C H Gan, J R Pugh, M J Cryan, J G Rarity, and G R Nash. Role of quasicylindrical waves and surface plasmon polaritons on beam shaping with resonant nanogratings in the infrared. *Physical Review B - Condensed Matter and Materials Physics*, 89(20):2–5, 2014. ISSN 1550235X. doi: 10.1103/PhysRevB.89.201415.

[23] Choon How Gan, Loïc Lalouat, Philippe Lalanne, and Lionel Aigouy. Optical quasicylindrical waves at dielectric interfaces. *Physical Review B - Condensed Matter and Materials Physics*, 83(8):085422, feb 2011. ISSN 10980121. doi: 10.1103/PhysRevB.83.085422. URL https://link.aps.org/doi/10.1103/PhysRevB.83.085422.

[24] J Gao, G Song, Q Gan, B Guo, and L Chen. Surface plasmon modulated nano-aperture vertical-cavity surface-emitting laser. *Laser Physics Letters*, 4(3):234–237, mar 2007. ISSN 1612-2011. doi: 10.1002/lapl.200610082. URL http://stacks.iop.org/1612-202X/4/i=3/a=011?key=crossref.ef1b69acc26918bac560cd453c7a5c56.

[25] F. J. García-Vidal, H. J. Lezec, T. W. Ebbesen, and L. Martín-Moreno. Multiple Paths to Enhance Optical Transmission through a Single Subwavelength Slit. *Physical Review Letters*, 90(21):4, 2003. ISSN 10797114. doi: 10.1103/PhysRevLett.90.213901.

[26] F. J. Garcia-Vidal, L. Martin-Moreno, T. W. Ebbesen, and L. Kuipers. Light passing through subwavelength apertures. *Reviews of Modern Physics*, 82(1):729–787, 2010. ISSN 00346861. doi: 10.1103/RevModPhys.82.729.

[27] G. Gay, O. Alloschery, B. Viaris De Lesegno, C. O'Dwyer, J. Weiner, and H. J. Lezec. The optical response of nanostructured surfaces and the composite diffracted evanescent wave model. *Nature Physics*, 2(4):262–267, apr 2006. ISSN 17452481. doi: 10.1038/nphys264. URL http://www.nature.com/doifinder/10.1038/nphys264.

[28] Lucille A Giannuzzi and Fred A. Stevie. *Introduction to focused ion beams: Instrumentation, theory, techniques and practice*. Springer US, Boston, MA, 2005. ISBN 0387231161. doi: 10.1007/b101190. URL http://link.springer.com/10.1007/b101190.

[29] Baoshan Guo, Guofeng Song, and Lianghui Chen. Plasmonic very-small-aperture lasers. *Applied Physics Letters*, 91(2):021103, jul 2007. ISSN 0003-6951. doi: 10.1063/1.2755784. URL http://aip.scitation.org/doi/10.1063/1.2755784.

[30] Baoshan Guo, Guofeng Song, and Lianghui Chen. Plasmonic very-small-aperture lasers. *Applied Physics Letters*, 91(2):021103, jul 2007. ISSN 0003-6951. doi: 10.1063/1.2755784. URL https://aip.scitation.org/doi/10.1063/1.2755784http://aip.scitation.org/doi/10.1063/1.2755784.

[31] O. E. Higbee, C. H. Gan, and G. R. Nash. Quasicylindrical waves at dielectric interfaces. *Frontiers in Optics*, 2016. doi: 10.1364/FIO.2016.JTh2A.75. URL https://doi.org/10.1364/FIO.2016.JTh2A.75.

[32] Daniel Hofstetter, Jérôme Faist, Mattias Beck, and Ursula Oesterle. Surface-emitting 10.1 μm quantum-cascade distributed feedback lasers. *Applied Physics Letters*, 75 (24):3769–3771, dec 1999. ISSN 0003-6951. doi: 10.1063/1.125450. URL http://aip.scitation.org/doi/10.1063/1.125450.

[33] Ji Homola, Sinclair S. Yee, and Günter Gauglitz. Surface plasmon resonance sensors: review. *Sensors and Actuators B: Chemical*, 54(1):3–15, 1999. ISSN 09254005. doi: 10.1016/S0925-4005(98)00321-9. URL http://www.sciencedirect.com/science/article/pii/S0925400598003219.

[34] Wico C L Hopman, Feridun Ay, Wenbin Hu, and Vishwas J Gadgil. Focused Ion Beam Milling Strategies of Photonic Crystal Structures in Silicon. In *European Conference on Integrated Optics, ECIO 2007*, volume 1, pages FA1—-FA1/1, Copenhagen, 2007. Technical University Denmark. URL http://doc.utwente.nl/64359/.

[35] Wico C L Hopman, Feridun Ay, Wenbin Hu, Vishwas J Gadgil, Laurens Kuipers, Markus Pollnau, and René M de Ridder. Focused ion beam scan routine, dwell time and dose optimizations for submicrometre period planar photonic crystal components and stamps in silicon. *Nanotechnology*, 18(19):195305, 2007. ISSN 0957-4484. doi: 10.1088/0957-4484/18/19/195305. URL http://stacks.iop.org/0957-4484/18/i=19/a=195305?key=crossref.d5ea32faae1796a60f5c0df4e93ea035.

[36] P. B. Johnson and R. W. Christy. Optical Constants of the Noble Metals. *Physical Review B*, 6(12):4370–4379, dec 1972. ISSN 0556-2805. doi: 10.1103/PhysRevB.6.4370. URL https://link.aps.org/doi/10.1103/PhysRevB.6.4370.

[37] Kane Yee. Numerical solution of initial boundary value problems involving maxwell's equations in isotropic media. *IEEE Transactions on Antennas and Propagation*, 14(3): 302–307, may 1966. ISSN 0018-926X. doi: 10.1109/TAP.1966.1138693. URL http://ieeexplore.ieee.org/document/1138693/.

[38] Masoud Kasraian and Dan Botez. Metal-grating-outcoupled, surface-emitting distributed-feedback diode lasers. *Applied Physics Letters*, 69(19):2795–2797, 1996. ISSN 00036951. doi: 10.1063/1.116846.

[39] Heung-Bae Kim, Gerhard Hobler, Andreas Steiger, Alois Lugstein, and Emmerich Bertagnolli. Full three-dimensional simulation of focused ion beam micro/nanofabrication. *Nanotechnology*, 18(24):245303, 2007. ISSN 0957-4484. doi: 10.1088/0957-4484/18/24/245303. URL http://stacks.iop.org/0957-4484/18/i=24/a=245303?key=crossref.db538ce41c3e6c6fe2629548d62c1021.

[40] E. Kretschmann. Decay of non radiative surface plasmons into light on rough silver films. Comparison of experimental and theoretical results. *Optics Communications*, 6 (2):185–187, oct 1972. ISSN 00304018. doi: 10.1016/0030-4018(72)90224-6. URL http://linkinghub.elsevier.com/retrieve/pii/0030401872902246.

[41] E. Kretschmann and H. Raether. Radiative Decay of Non Radiative Surface Plasmons Excited by Light, jan 1968. ISSN 18657109. URL https://www.degruyter.com/view/j/zna.1968.23.issue-12/zna-1968-1247/zna-1968-1247.xml.

[42] P. Lalanne and J. P. Hugonin. Interaction between optical nano-objects at metallo-dielectric interfaces. *Nature Physics*, 2(8):551–556, aug 2006. ISSN 1745-2473. doi: 10.1038/nphys364. URL http://www.nature.com/doifinder/10.1038/nphys364.

[43] P. Lalanne, J. P. Hugonin, H. T. Liu, and B. Wang. A microscopic view of the electromagnetic properties of sub-λ metallic surfaces. *Surface Science Reports*, 64(10):453–469, 2009. ISSN 01675729. doi: 10.1016/j.surfrep.2009.07.003.

[44] H. J. Lezec, A. Degiron, E. Devaux, R. A. Linke, L. Martin-Moreno, F. J. Garcia-Vidal, and T. W. Ebbesen. Beaming light from a subwavelength aperture. *Science*, 297(5582): 820–822, 2002. ISSN 00368075. doi: 10.1126/science.1071895.

[45] Nathan C Lindquist, Prashant Nagpal, Kevin M Mcpeak, and Jacques Gierak. Focused ion beam technology and ultimate applications. *Semiconductor Science and Technology*, 24(4):3001, 2009. doi: 10.1088/0268-1242/24/4/043001.

[46] Stefan Maier. *Plasmonics : fundamentals and applications*. Springer, 2007. ISBN 0387331506 9780387331508 9780387378251 (e-ISBN) 0387378251 (e-ISBN). URL http://www.loc.gov/catdir/toc/fy0715/2006931007.html.

[47] L. Martín-Moreno, F. J. García-Vidal, H. J. Lezec, A. Degiron, and T. W. Ebbesen. Theory of Highly Directional Emission from a Single Subwavelength Aperture Surrounded by Surface Corrugations. *Physical Review Letters*, 90(16):167401, apr 2003. ISSN 0031-9007. doi: 10.1103/PhysRevLett.90.167401. URL https://link.aps.org/doi/10.1103/PhysRevLett.90.167401.

[48] J. C. Maxwell. A Dynamical Theory of the Electromagnetic Field. *Philosophical Transactions of the Royal Society of London*, 155(0):459–512, jan 1865. ISSN 0261-0523. doi: 10.1098/rstl.1865.0008. URL http://rstl.royalsocietypublishing.org/cgi/doi/10.1098/rstl.1865.0008.

[49] John Melngailis. Critical review: focused ion beam technology and applications. *Journal of Vacuum Science & Technology B: Microelectronics and Nanometer Structures*, 5(469), 1987.

[50] Etienne Menard and John A. Rogers. Stamping Techniques for Micro- and Nanofabrication, 2010.

[51] E. Mujagić, L. K. Hoffmann, S. Schartner, M. Nobile, W. Schrenk, M. P. Semtsiv, M. Wienold, W. T. Masselink, and G. Strasser. Low divergence single-mode surface emitting quantum cascade ring lasers. *Applied Physics Letters*, 93(16):20–23, 2008. ISSN 00036951. doi: 10.1063/1.3000630.

[52] Lars Nähle, Julia Semmel, Wolfgang Kaiser, Sven Höfling, and Alfred Forchel. Tapered quantum cascade lasers. *Applied Physics Letters*, 91(18):181122, oct 2007. ISSN 0003-6951. doi: 10.1063/1.2805628. URL http://aip.scitation.org/doi/10.1063/1.2805628.

[53] Adnan H. Nayfeh. The general problem of elastic wave propagation in multilayered anisotropic media. *The Journal of the Acoustical Society of America*, 89(4):1521–1531, 1991. ISSN 00014966. doi: 10.1121/1.400988.

[54] Adnan H. Nayfeh and D. E. Chimenti. Ultrasonic Wave Reflection From Liquid-Coupled Orthotropic Plates With Application to Fibrous Composites. *Journal of Applied Mechanics*, 55(4):863, dec 1988. ISSN 00218936. doi: 10.1115/1.3173734. URL http://appliedmechanics.asmedigitalcollection.asme.org/article.aspx?articleid=1409435.

[55] Northumbria Optical Coatings Limited. Mid-IR dieletric band pass filter transmission profile. Technical report.

[56] Hajime Okuda, Haruhisa Soda, Tunneling Microscope, Kazuhiro Kurihara, Yasuyuki Miyamoto, Kazuhito Furuya, Surface Emitting Laser, Hideshi Kawasaki, Fumio Koyama, Kenichi Iga, Cun-zheng Ning, Weng W Chow, and Stephan Reitzenstein. Related content GaInAsP / InP Surface Emitting Injection Lasers. 1979.

[57] Jon Orloff, Mark Utlaut, and Lynwood Swanson. *High Resolution Focused Ion Beams: FIB and its Applications*. Springer US, Boston, MA, 2003. ISBN 978-1-4613-5229-7. doi: 10.1007/978-1-4615-0765-9. URL http://link.springer.com/10.1007/978-1-4615-0765-9.

[58] Andreas Otto. Excitation of nonradiative surface plasma waves in silver by the method of frustrated total reflection. *Zeitschrift für Physik*, 216(4):398–410, aug 1968. ISSN 14346001. doi: 10.1007/BF01391532. URL http://link.springer.com/10.1007/BF01391532.

[59] Edward D. Palik. *Handbook of optical constants of solids*. Academic Press, 1998. ISBN 9780125444156. URL http://www.sciencedirect.com/science/book/9780125444156.

[60] M.W Phaneuf. Applications of focused ion beam microscopy to materials science specimens. *Micron*, 30(3):277–288, 1999. ISSN 09684328. doi: 10.1016/S0968-4328(99)00012-8. URL http://www.sciencedirect.com/science/article/pii/S0968432899000128.

[61] Heinz Raether. *Surface Plasmons on Smooth and Rough Surfaces and on Gratings*, volume 111 of *Springer Tracts in Modern Physics*. Springer Berlin Heidelberg, Berlin, Heidelberg, 1988. ISBN 978-3-540-17363-2. doi: 10.1007/BFb0048317. URL http://link.springer.com/10.1007/BFb0048317.

[62] Lord Rayleigh. On the Dynamical Theory of Gratings. *Proceedings of the Royal Society of London A: Mathematical, Physical and Engineering Sciences*, 79(532), 1907. URL http://rspa.royalsocietypublishing.org/content/79/532/399.

[63] Steve Reyntjens and Robert Puers. A review of focused ion beam applications in microsystem technology. *Journal of Micromechanics and Microengineering*, 11(4):287–300, 2001. ISSN 0960-1317. doi: 10.1088/0960-1317/11/4/301.

[64] Alexander Rigort and Jürgen M. Plitzko. Cryo-focused-ion-beam applications in structural biology. *Archives of Biochemistry and Biophysics*, 581:122–130, 2015. ISSN 00039861. doi: 10.1016/j.abb.2015.02.009. URL http://www.sciencedirect.com/science/article/pii/S0003986115000715.

[65] M. M. Saad, R. M. Bowman, and J. M. Gregg. Characteristics of single crystal thin film capacitor structures made using a focused ion beam microscope. *Applied Physics Letters*, 84(7):1159–1161, feb 2004. ISSN 0003-6951. doi: 10.1063/1.1645318. URL http://aip.scitation.org/doi/10.1063/1.1645318.

[66] Matthew N. O. Sadiku. *Numerical techniques in electromagnetics*. CRC Press, 2001. ISBN 9781482225785. URL https://www.crcpress.com/Numerical-Techniques-in-Electromagnetics-Second-Edition/Sadiku/p/book/9781482225785.

[67] a Schilling, T Adams, R M Bowman, and J M Gregg. Strategies for gallium removal after focused ion beam patterning of ferroelectric oxide nanostructures. *Nanotechnology*, 18 (3):035301, 2007. ISSN 0957-4484. doi: 10.1088/0957-4484/18/3/035301.

[68] D. R. Scifres, R. D. Burnham, and W. Streifer. Lateral grating array high power CW visible semiconductor laser. *Electronics Letters*, 18(13):549–550, 1982. ISSN 00135194. doi: 10.1049/el:19820372.

[69] R. L. Seliger, J. W. Ward, V. Wang, and R. L. Kubena. A high-intensity scanning ion probe with submicrometer spot size. *Applied Physics Letters*, 34(5):310–312, 1979. ISSN 00036951. doi: 10.1063/1.90786.

[70] A. Sommerfeld. The broadening of the waves and the wireless telegraph. *Annalen der Physik*, 665(28), 1909.

[71] John C. Strikwerda. *Finite Difference Schemes and Partial Differential Equations, Second Edition*. Society for Industrial and Applied Mathematics, jan 2004. ISBN 978-0-89871-567-5. doi: 10.1137/1.9780898717938. URL http://epubs.siam.org/doi/book/10.1137/1.9780898717938.

[72] A. Taflove and S. C. Hagness. *Computational Electrodynamics: The Finite-Difference Time-Domain Method*. Artech House,

2000. URL https://www.scholars.northwestern.edu/en/publications/computational-electrodynamics-the-finite-difference-time-domain-m-2.

[73] A. Taflove and A. Taflove. Advances in Computational Electrodynamics: The Finite-Difference Time-Domain Method, 1998. URL https://www.scholars.northwestern.edu/en/publications/advances-in-computational-electrodynamics-the-finite-difference-t.

[74] Ivo Utke, Patrik Hoffmann, and John Melngailis. Gas-assisted focused electron beam and ion beam processing and fabrication. *Journal of Vacuum Science & Technology B: Microelectronics and Nanometer Structures*, 26(4):1197, 2008. ISSN 10711023. doi: 10.1116/1.2955728. URL http://scitation.aip.org/content/avs/journal/jvstb/26/4/10.1116/1.2955728.

[75] L. Wang and S.I. Rokhlin. Stable reformulation of transfer matrix method for wave propagation in layered anisotropic media. *Ultrasonics*, 39(6):413–424, oct 2001. ISSN 0041624X. doi: 10.1016/S0041-624X(01)00082-8. URL http://linkinghub.elsevier.com/retrieve/pii/S0041624X01000828.

[76] R W Wood. On a Remarkable Case of Uneven Distribution of Light in a Diffraction Grating Spectrum. *Proceedings of the Physical Society of London*, 18(1):269–275, jun 1902. ISSN 1478-7814. doi: 10.1088/1478-7814/18/1/325. URL http://stacks.iop.org/1478-7814/18/i=1/a=325?key=crossref.7ebbe1383fb00dffe4b52e1569cdd953.

[77] Amnon Yariv and Pochi Yeh. *Photonics: optical electronics in modern communications*. 2007. ISBN 9780195179460. doi: 0195106261.

[78] Liang Bin Yu, Ding Zheng Lin, Yi Chun Chen, You Chia Chang, Kuo Tung Huang, Jiunn Woei Liaw, Jyi Tyan Yeh, Jonq Min Liu, Chau Shioung Yeh, and Chih Kung Lee. Physical origin of directional beaming emitted from a subwavelength slit. *Physical Review B - Condensed Matter and Materials Physics*, 71(4):2–5, 2005. ISSN 10980121. doi: 10.1103/PhysRevB.71.041405.

[79] Nanfang Yu, Romain Blanchard, Jonathan Fan, Federico Capasso, Tadataka Edamura, Masamichi Yamanishi, and Hirofumi Kan. Small divergence edge-emitting semiconductor lasers with two-dimensional plasmonic collimators. *Applied Physics Letters*, 93(18):91–94, 2008. ISSN 00036951. doi: 10.1063/1.3009599.

[80] Nanfang Yu, Jonathan Fan, Qi Jie Wang, Christian Pflügl, Laurent Diehl, Tadataka Edamura, Masamichi Yamanishi, Hirofumi Kan, and Federico Capasso. Small-divergence semiconductor lasers by plasmonic collimation. *Nature Photonics*, 2(9):

564–570, sep 2008. ISSN 1749-4885. doi: 10.1038/nphoton.2008.152. URL http://www.nature.com/articles/nphoton.2008.152.

[81] Nanfang Yu, Mikhail Kats, Christian Pflugl, Markus Geiser, Qi Jie Wang, Mikhail A. Belkin, Federico Capasso, Milan Fischer, Andreas Wittmann, JÌrôme Faist, Tadataka Edamura, Shinichi Furuta, Masamichi Yamanishi, and Hirofumi Kan. Multi-beam multi-wavelength semiconductor lasers. *Applied Physics Letters*, 95(16):2009–2011, 2009. ISSN 00036951. doi: 10.1063/1.3253713.

[82] Nanfang Yu, Qi Jie Wang, Christian Pflugl, Laurent Diehl, Federico Capasso, Tadataka Edamura, Shinichi Furuta, Masamichi Yamanishi, and Hirofumi Kan. Semiconductor lasers with integrated plasmonic polarizers. *Applied Physics Letters*, 94(15):151101, apr 2009. ISSN 0003-6951. doi: 10.1063/1.3093476. URL http://aip.scitation.org/doi/10.1063/1.3093476.

[83] J. Zenneck. Über die Fortpflanzung ebener elektromagnetischer Wellen längs einer ebenen Leiterfläche und ihre Beziehung zur drahtlosen Telegraphie. *Annalen der Physik*, 328(10):846–866, 1907. ISSN 15213889. doi: 10.1002/andp.19073281003. URL http://doi.wiley.com/10.1002/andp.19073281003.

[84] Yao Zhai, Yaoguang Ma, Sabrina N. David, Dongliang Zhao, Runnan Lou, Gang Tan, Ronggui Yang, and Xiaobo Yin. Scalable-manufactured randomized glass-polymer hybrid metamaterial for daytime radiative cooling. *Science*, 355(6329):1062–1066, 2017. ISSN 0036-8075. doi: 10.1126/science.aai7899. URL http://www.sciencemag.org/lookup/doi/10.1126/science.aai7899.